The impact of black holes on the stellar-dynamical properties of early-type galaxies

Matteo Frigo

München 2019

The impact of black holes on the stellar-dynamical properties of early-type galaxies

Matteo Frigo

Dissertation
an der Fakultät der Physik
der Ludwig–Maximilians–Universität
München

vorgelegt von
Matteo Frigo
aus Valdagno (Italien)

München, den 29/01/2019

Contents

List of Figures

List of Tables

Zusammenfassung

In dieser Arbeit untersuchen wir den Einfluss von supermassereichen Schwarzen Löchern (SMBH) auf die sie beherbergenden Galaxien und im speziellen deren stellare Kinematik, mit Hilfe von zwei Sets von Simulationen.

Das erste Set besteht aus zehn Paaren von kosmologischen Zoom-Simulationen, in dem jedes Paar die gleichen Anfangsbedingungen nutzt, aber nur eine der beiden Simulationen die energetische Rückwirkung des aktiven galaktischen Kerns (AGN) modelliert. Wir vergleichen dann die sich daraus entwickelnden Galaxien mit Hilfe von nachgebildeten Beobachtungen mit einem Integrativfeld-Spektographen (IFU) um den Einfluss des AGN zu untersuchen.

Bei hoher Rotverschiebung sind alle Systeme schnell rotierend und scheibenförmig. Nach $z \sim 1$ entwickeln sich die Galaxien mit AGN zu älteren, weniger metallreichen und langsamer rotierenden Systemen niedrigerer Masse und weniger scheibenförmigen Isophoten - in allgemeiner Übereinstimmung mit Beobachtungen. Zweidimensionale kinematische Karten von in-situ und akkretierten Sternen zeigen, dass diese Unterschiede Ergebnis einer aufgrund der AGN Rückwirkung reduzierten internen Sternentstehung sind. Eine vollständige Analyse der Sternenorbits zeigt, dass Galaxien mit AGN typischerweise triaxialer sind und einen höheren Anteil von X-Tuben und Box-Orbits und einen geringeren von Z-Tuben besitzen. Dieser Trend lässt sich auch mit der reduzierten internen Sternentstehung in späteren Stufen der Entwicklung erklären. Wir führen den globalen Parameter ξ_3 ein, um die Antikorrelation zwischen dem kinematischen Moment dritter Ordnung h_3 und der normierten Geschwindigkeit entlang der Sichtachse V/σ zu charakterisieren und vergleichen die Werte in Simulationen und der ATLAS^{3D}-Beobachtungen. Der kinematische Asymmetrieparameter ξ_3 kann eine nützlicher Kennwert für große IFU-Durchmusterungen sein, da es ein kinematischer Indikator fr die intrinschische Form und Orbitverteilung ist. Wir benutzen die selben Simulationen um zwei verschiedene Methoden zur Messung von Galaxienmassen zu testen. Einmal die anisotrope Jeans-Modellierung mit zwei verschiedenen Dichteprofilen, einem einfachen Potenzgesetz und der Summe der deprojizierten stellaren Masseverteilung unter Annahme eines konstanten Licht-Masse-Verhältnisses und eines Potenzgesetzes für die dunkle Materie. Hiermit erhalten wir erfolgreich die Masse und das Dichteprofil der simulierten Galaxien. Wir vergleichen die tatsächlichen und erhaltenen Anteile dunkler Materie unserer Simulationen mit Beobachtungen von ATLAS^{3D} und finden einen deckungsgleichen Bereich jener Anteile. Nichtsdestotrotz sind die dynamischen Modellierungsverfahren nicht in der Lage die durchschnittliche Geschwindigkeitsdis-

persion und die Steigung des Dichteprofils zu bestimmen. Die Abweichungen zeigen keine Korrelation mit den Eigenschaften der simulierten Galaxien oder der Einbeziehung der AGN-Rückwirkung. Dies mag teilweise dem Umstand geschuldet sein, dass die Modellierung versucht Artefakte, die aus der unzureichenden Auflösung resultieren, abzubilden. Dies zeigt, dass dynamische Modellierung nicht zuverlässig in der Anwendung auf heutige kosmlogische Simulationen ist. Die andere Methode zur Massenbestimmung ist die Rekonstruktion von gravitativ verzerrten Quellen. Wir haben Beobachtungen von gravitativ verzerrten Bildern mithilfe der simulierten Galaxien nachgebildet und dann mit einem Quellen-Rekonstruktions-Code die Masse der Galaxien innerhalb des Einstein-Radius mit guter Genauigkeit und wenig Anfälligkeit gegenber simulationsbedingkten Ungenauigkeiten bestimmt. Die AGN-Rückwirkung schein keinen Einfluss auf die Profilsteigungen unserer Galaxien zu haben.

Das zweite Set an Simulationen, das wir untersucht haben, besteht aus zwölf Simulationen von Verschmelzungen elliptischer Galaxien gleicher und unterschiedlicher Masse mit Sternen, Dunkler Materie und Schwarzen Löchern. Es wird angenommen, dass die gravitative Interaktion zwischen den Schwarzen Löchern und den Sternen während und nach der Verschmelzung die Sterne nach außen schiebt, was zu einer tangential verzerrten Galaxie mit einem Kern führt. Wir untersuchen diesen Effekt detailliert in dem wir eine volle Analyse der Sternenorbits und der dreidimensionalen Form des Ergebnisses der Verschmelzung druchfhren. Die Interaktionen des Schwarzen Löcher werden mithilfe des Integrators KETJU genau (bis zu post-newtonschen Termen) berechnet. Wir sehen, dass die verschmolzenen Systeme prolat sind und von X-Tuben dominiert werden, allerdings mit steigender Masse des zentralen Schwarzen Lochs sphrischer und werden und mehr Z-Tuben anstatt X-Tuben besitzen. Wir können die erwartete Abnahme des Anteils von Box-Orbits nicht bestätigen. Dies kann heißen, dass unser Verstndnis der Orbitstruktur von elliptischen Galaxien mit Kern unvollständig ist. Wir verbinden diese Ergebnisse mit beobachtbaren Merkmalen in den projizierten kinematischen Karten.

Abstract

In this thesis we investigate the impact of supermassive black holes (SMBH) on their host galaxies, and specifically on their stellar kinematics, using two sets of simulations.

The first set consists of ten pairs of zoom cosmological simulations, in which each pair uses the same initial conditions but one includes energy feedback from Active Galactic Nuclei (AGN) and the other does not. We then compare the resulting galaxies mocking maps from observational integral field unit (IFU) surveys to investigate the impact of AGN feedback. At high redshift all systems are mostly fast-rotating and disk-like. After $z \sim 1$ the AGN simulations result in lower-mass, older, less metal rich and slower-rotating systems, with less disky isophotes - in general agreement with observations. Two-dimensional kinematic maps of in-situ and accreted stars show that these differences result from reduced in-situ star formation due to AGN feedback. A full analysis of stellar orbits indicates that galaxies simulated with AGN are typically more triaxial and have higher fractions of x-tubes and box orbits and lower fractions of z-tubes. This trend can also be explained by reduced late in-situ star formation. We introduce a global parameter, ξ_3, to characterize the anti-correlation between the third-order kinematic moment h_3 and the line-of-sight velocity (V/σ), and compare to ATLAS^{3D} observations. The kinematic asymmetry parameter ξ_3 might be a useful diagnostic for large integral field surveys as it is a kinematic indicator for intrinsic shape and orbital content.

We use the same simulations to test two methods for measuring galaxy masses from observations. One is anisotropic Jeans modelling, using two different models for the density profiles: a single power-law and the sum of the deprojected luminosity distribution - assuming a stellar mass-to-light ratio - plus a power-law for representing dark matter. We successfully recover the mass and density profile of the model galaxy. We compare our real and recovered dark matter fractions with observations from the ATLAS^{3D} survey, finding that they cover the same range. However the dynamical models are generally not accurate in retrieving the average velocity anisotropy of the system and the density profile slopes. The deviations do not seem to correlate with other model galaxy properties or the presence of AGN feedback. This might be partly related to the modelling trying to capture simulation artifacts caused by insufficient resolution. It indicates that dynamical modelling cannot be reliably applied to current cosmological simulations. The other method is reconstruction of gravitationally lensed sources. We constructed mock lensed images using the simulated galaxies as lenses. Using a source reconstruction code we then recovered the mass of the lens within the Einstein radius to good accuracy and less sensitivity to

simulation limitations. AGN feedback does not seem to impact the profile slopes of our galaxies.

The second set of simulations we analyzed consists of twelve isolated simulations of equal- and unequal-mass mergers of elliptical galaxies with stars, dark matter and black holes. The gravitational interactions between black holes and stars during and after the merger are believed to push stars away, leaving a tangentially-biased, cored galaxy. We study this effect in detail by performing a full analysis of the stellar orbits and three-dimensional shape of the merger remnants. The black hole interactions are calculated accurately (to post-Newtonian terms) by employing the KETJU integrator. We find that our remnants are prolate and dominated by x-tube orbits, but with increasing black hole mass the central region becomes more spherical and z-tube orbits take the place of x-tubes. We do not observe the expected decrease in the fraction of box orbits. This could mean that our understanding of the orbital structure of cored elliptical galaxies is incomplete. We connect these results with observable features in the projected kinematic maps.

"Mei Figur, a Wunder dar Natur!"

DJ Ötzi

Chapter 1

Introduction

Galaxies are the quintessential building block of the cosmos. They are complex systems of stars, gas, dust and dark matter held together by gravity , and they come in many different shapes and sizes. Historically, they have been classified using the Hubble (1926) 'tuning fork' diagram (Fig. 1.1). Here galaxies range from large spherical galaxies, to flatter ellipticals, to lenticular galaxies, to (barred or not barred) spiral galaxies, to irregular galaxies. The continuity in this diagram hinted at an evolutionary sequence from elliptical and lenticular galaxies, known as early-type galaxies (ETG), to spiral and irregular ones, known as late-type galaxies (LTG). This initial interpretation was soon discovered to be wrong, but the terminology has stuck and is still used to this day. The reason why, is that early-type and late-type galaxies have vastly different properties, in addition to their different shapes. ETGs are made almost exclusively of old stars, that shine in red light and have low metallicity. LTGs instead have many young metal-rich stars, including many massive ones, that shine in blue light and typically dominate the luminosity output of the galaxy. The galaxy itself is not necessarily younger - the Milky Way is for instance a late-type galaxy and is almost as old as the universe - but due to the presence of active star formation the average age of its stars is much lower than in a typical elliptical galaxy. ETGs are quiescent systems, and often did not experience major star formation events in billions of years. Early- and late-type galaxies also live in different environments: ETGs are more commonly found in crowded galaxy clusters, while LTGs are more common in galaxy groups or in the field (although exceptions to both are often found). Furthermore, the most massive and luminous early-type galaxies have different properties from the lower mass ones. Lower luminosity ETGs are typically more flattened, rotate faster, have disky isophotes, and have extra light in their core. By contrast higher luminosity ETGs are more likely to be spherical, to not have net rotation, to have boxy isophotes, and to have a flattened luminosity profile in their central regions (e.g. Bender, 1988; Kormendy and Bender, 1996; Kormendy et al., 2009; Cappellari, 2016). What processes cause galaxies to obtain these different properties during cosmic time?
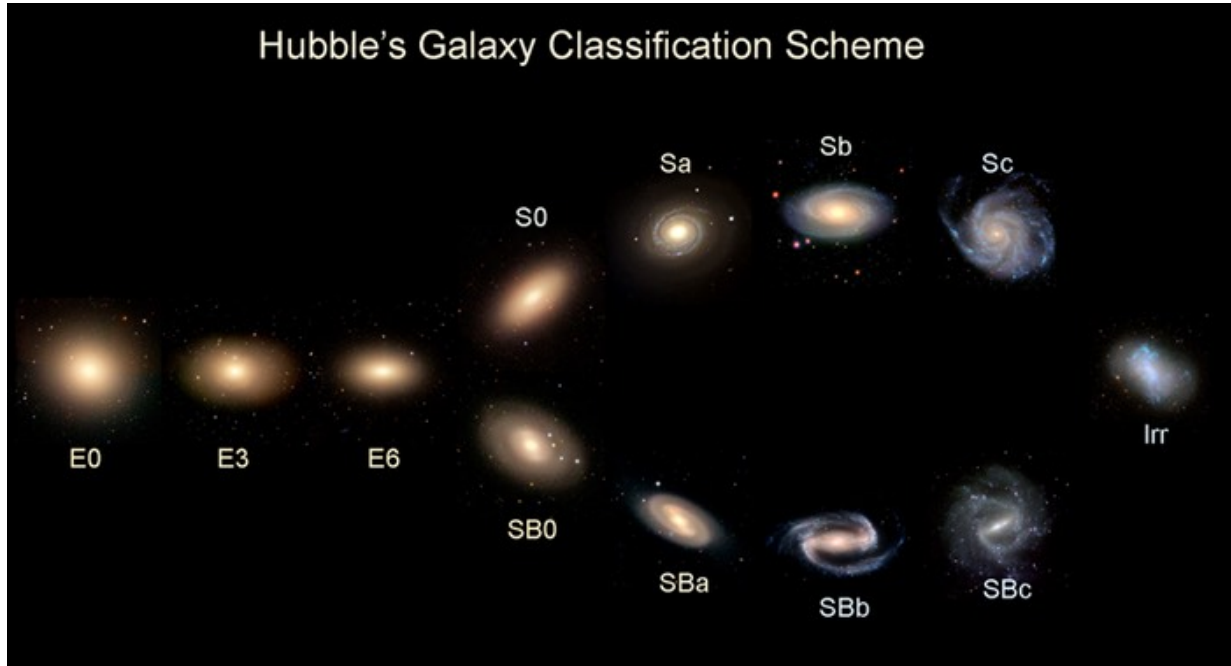
Figure 1.1: Hubble's 'tuning fork' diagram for classifying galaxies according to their shapes. Image credit: Galaxy Zoo project.

1.1   Galaxy growth: in-situ formation and accretion

The evolution of a galaxy is in large part determined by what mechanism lead it to grow its stellar component. There are two main ways: formation of stars *in-situ* within the galaxy and accretion of stars from other galaxies.

In-situ star formation requires the presence of cold gas within the galaxy. If the gas is cold and dense enough, it will undergo gravitational collapse and form stars. A criterion for this to happen was given by Jeans (1902). In order to collapse, the gas cloud must have a mass M larger than the Jeans mass M_J:

$$M_J = C\sqrt{T^3/n}\,, \tag{1.1}$$

where T is the gas temperature, n is the number density and C a constant which depends on the composition of the gas cloud. If it is made of atomic hydrogen, $C \sim 30000$. When $M > M_J$, the cloud's self-gravity will overcome its gas pressure, and the cloud will collapse until nuclear fusion ignites in the newly-born star, providing an energy source that stops the collapse. On a galactic scale, gas enters the galaxy's dark matter halo from the surrounding environment, and its gravitational energy gets converted to heat (virial shock heating, Birnboim and Dekel, 2003). If the halo is massive enough, this process prevents further collapse, forming a hot gaseous halo. This gas can then gradually cool down and fall to the center of the gravitational potential, where it can form stars. In less massive halos shock heating is negligible, and the gas falls directly to the center of the potential and cools

rapidly (Dekel and Birnboim, 2006). Gas typically collapses first along the direction of its angular momentum, producing a star-forming disk (like in spiral galaxies). The process of star formation is self-regulated thanks to what is known as supernova feedback. The short lives of massive stars (of the order of millions of years) end in type II supernovas, which inject a lot of energy into their surrounding gas. This heats up the gas and lowers its density, limiting further star formation.

The other main growth process of a galaxy is accretion. Galaxy mergers are ubiquitous in the universe, but make up only a small fraction of the mass of irregular and spiral galaxies. In massive elliptical galaxies they can however account for as much as 80% of their mass (Rodriguez-Gomez et al., 2016). Mergers between galaxies of equal-mass (major mergers) are relatively rare (Man et al., 2012). They however do happen and have a disruptive impact on the merging galaxies, changing their shape, flattening metallicity gradients (Di Matteo et al., 2009), and making the system dynamically hotter (more random motion instead of ordered rotation). Major mergers between spiral galaxies have long been known to produce elliptical remnants, but this is actually a rare occurrence (Ostriker, 1980). The current understanding of the formation of massive elliptical galaxies is the 'two phase' model, where they initially formed at high-redshift as compact systems, by in-situ star formation, and then slowly accreted stars through unequal-mass (minor) gas-poor mergers (Oser et al., 2010). Minor mergers are more likely to deposit the accreted stars in the outskirts of the larger galaxy (Naab et al., 2009; Hilz et al., 2012; Hilz et al., 2013), resulting in very extended elliptical systems. They also tend to make the system more spherical and lower its spin (Qu et al., 2010), and they are more efficient than major mergers at increasing the dark matter fraction of the galaxy (Hilz et al., 2013).

When gas is involved in the merger the picture gets more complicated, as the galaxy grows both by accretion of stars and by in-situ formation from the accreted gas. The gas tends to collapse to the central regions and form stars there (Barnes and Hernquist, 1996), which could then explain the extra light observed in the center of low-mass elliptical galaxies (Kormendy et al., 2009). The scenario that emerges is one in which the relative importance of in-situ formation and accretion is the main factor determining galaxy evolution.

1.2   The role of supermassive black holes

When comparing the mass distribution of galaxies in observations and simulations, we see that given the amount of gas available in the universe there should be many more galaxies than what we observe. Several studies have computed the ratio between stellar and halo mass as a function of halo mass (Figure 1.2), finding that this peaks at halo masses around $10^{12}\,M_\odot$, which is about the mass of the Milky Way's halo. More massive and less massive halos host galaxies with less mass relative to them. In other words, star formation is less efficient in these halos. This is known as the overcooling problem, and has been known for a long time (White and Rees, 1978). In the current understanding, star formation in low-mass halos is suppressed because of Supernova feedback. While it happens in galaxies of any mass, it is most efficient in low-mass galaxies, where gas is less dense. In the high-mass
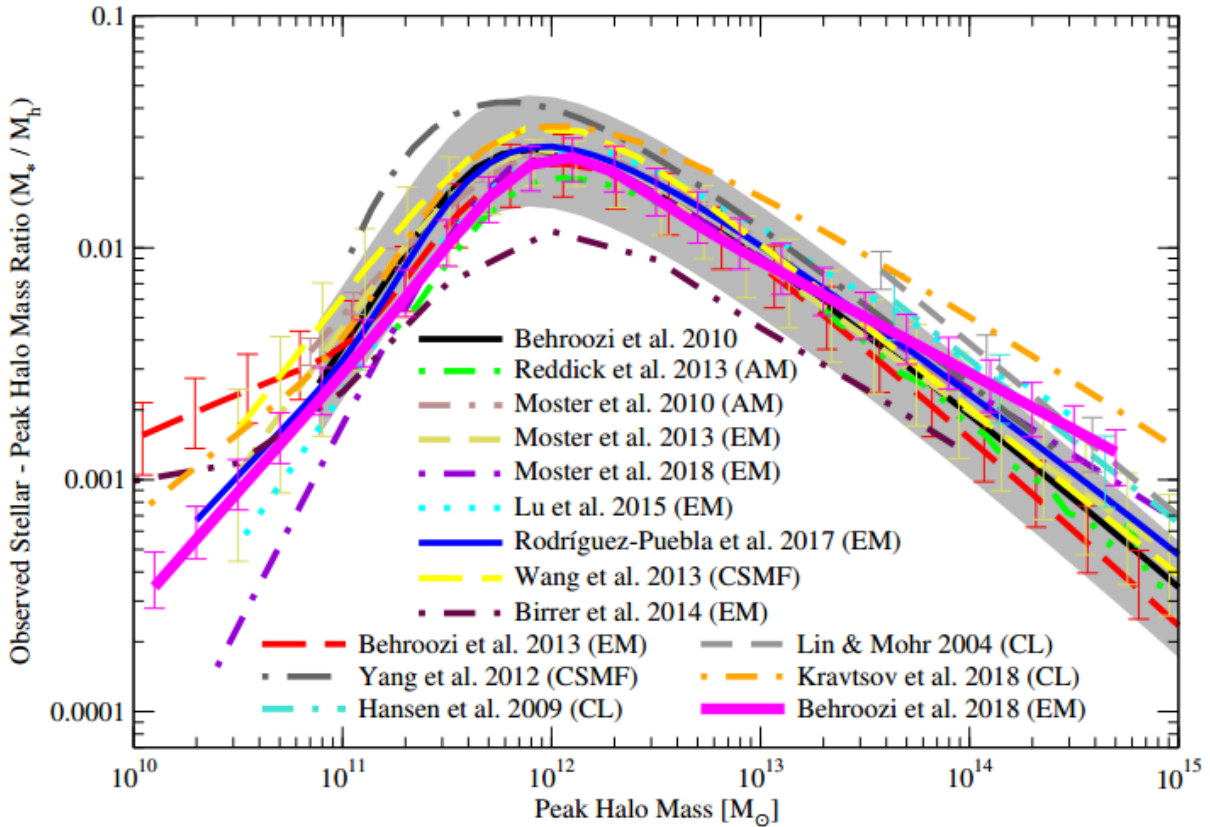
Figure 1.2: The observed stellar-to-halo mass function from various studies. Source: Behroozi et al., 2018.

end, the culprit is believed to be the energy output of supermassive black holes, known as AGN feedback (e.g. Puchwein and Springel, 2013; Schaye et al., 2015; Davé et al., 2016). Active Galactic Nuclei (AGN) are extremely bright regions in the centers of some galaxies, that emit light in stellar and non-stellar wavelengths (radio, x-rays, gamma rays). Many competing theories tried to explain their origin, but ultimately it was concluded that they are powered by supermassive black holes (Salpeter, 1964; Urry and Padovani, 1995), which are believed to reside in the center of every galaxy (e.g.Kormendy and Ho, 2013), including our own (Genzel et al., 1997). The conversion of the gravitational energy of infalling matter into thermal energy in the accretion disks of these black holes produces unfathomable amounts of energy, which can affect the whole host galaxy. The specific behavior depends on the accretion rate of the SMBH. At high accretion rates the AGN is in 'quasar mode', and its luminosity tipically reaches the Eddington (1916) limit, beyond which radiation pressure would overcome the gravitational force keeping the accretion disk together. Since the mass of SMBHs can be measured in billions of solar masses, this often means that it can outshine its host galaxy. The emitted radiation interacts with gas in the inter-stellar medium, heating it up substantially through Compton scattering. This is also accompa-

nied by strong winds coming from the core (Alatalo et al., 2011; Yuan and Narayan, 2014; Cheung et al., 2016), which can effectively drive gas out of the galaxy (Wylezalek and Zakamska, 2016). At low accretion rates the AGN is in 'radio mode', it is not bright and emits only in radio. Typically radio-mode AGNs have visible relativistic jets (e.g. the ones observed in M87), which are believed to contribute to counteract the cooling of the hot gaseous halos which surround elliptical galaxies (Churazov et al., 2005). Combining these effects AGN feedback is believed to be able to turn star-forming galaxies into quiescent ones, and keeping them that way (see Fabian, 2012 for a review on observational properties of AGN feedback). Because of this, simulations that include AGN feedback produce more realistic massive elliptical galaxies (e.g. Springel et al., 2005, Croton et al., 2006, Puchwein et al., 2008, Eisenreich et al., 2017; see Naab and Ostriker, 2017 for a review).

Supermassive black holes can also impact their host galaxy without feedback, simply because of their dynamics. During galaxy mergers their gravitational interaction with stars result in many of them being pushed out of the central region of the remnant galaxy. This can produce a cored density profile (Hills and Fullerton, 1980; Rantala et al., 2018a), which is observed in many massive elliptical galaxies. All of these results point towards a picture in which black holes and galaxies coevolve, and this could help explain the many correlations that have been observed between super massive black hole mass and various galactic properties, such as mass, velocity dispersion, and core size (see Kormendy and Ho, 2013 for a review).

1.3 Purpose and structure of this thesis

Recently, the study of galaxy evolution has been greatly advanced by the introduction of Integral Field Unit (IFU) spectrographs. These instruments collect a spectrum for each of their spatial pixels, so that one can observe the spatial distribution of spectrum-derived quantities, such as stellar and gas kinematics, metallicity or stellar age. Recently a number of large galaxy surveys have been performed with IFU spectrographs, such as MaNGA (Bundy et al., 2015), SAMI (Croom et al., 2012) and CALIFA (Sánchez et al., 2012), resulting in the mapping of thousands of galaxies. The MUSE spectrograph (Bacon et al., 2010) also delivered detailed 2D maps of galactic properties (e.g., Emsellem et al., 2014, Krajnović et al., 2018), including at high redshift (Guérou et al., 2016). This means that a huge library of data on the interaction between supermassive black holes and their host galaxies is available, and simulations can be compared to it to obtain a better understanding.

In this thesis we intend to use simulations of the formation of galaxies - both cosmological and isolated - to study the impact of black holes on galactic properties, with special focus on the stellar kinematics. The dynamics of stars are particularly interesting because, due to their collisionless nature, they preserve information about the formation processes of galaxies for a long time. While simulations have already been used to study how AGN feedback affects the angular momentum of galaxies (Dubois et al., 2013; Martizzi et al., 2014; Penoyre et al., 2017; Lagos et al., 2018; Schulze et al., 2018b) or how supermassive

black hole dynamics affect merger remnants (Rantala et al., 2018a), here we want to have a closer look at both things by studying in detail the stellar kinematics and orbital structures of a few systems simulated in high resolution.

Following is the structure of the thesis. Chapter 2 will present the theory and applications of stellar dynamics in galaxies, with particular focus on 2D kinematics, orbit analysis and dynamical modelling. Here we will also introduce a new parameter for characterizing the third-order kinematics of galaxies, which will be used in the following analysis. Chapter 3 will present the simulation code we used and our two sets of simulations: zoom cosmological and isolated. In Chapter 4 we will use mock IFU maps of the kinematics and stellar-population properties of our simulated galaxies to analyze how AGN feedback impacts them. The mock observational kinematics will be connected to the galaxies' formation history and accreted/in-situ fractions, as well as with the actual orbital structure of the galaxy. We will also compare our results with the ATLAS^{3D} survey. In Chapter 5 we will test how well the density profile of galaxies can be recovered through dynamical modelling or gravitational lensing estimates, and whether the presence of supermassive black holes affects the measured density profiles. In Chapter 6 we will analyze merger simulations with accurate black hole dynamics, to evaluate how the gravitational interactions between black holes and stars affect the orbital structure of the remnants. Chapter 7 will summarize our results and discuss potential future developments.

Chapter 2

Stellar dynamics

The movement of stars within a galaxy is a complex problem. The trajectory of a star is determined by the galactic gravitational potential, which can have complex shapes or evolve in time. It is not directly observable, and the fact that two of the main components of galaxies, dark matter and black holes, are invisible to us, makes estimating it even harder. From our point of view on Earth we only see the stellar velocities projected along the line-of-sight (LOS), and the orbital periods of stars are many orders of magnitude beyond our observation time-frame (with the exception of stars that orbit very close to a supermassive black hole (Schödel et al., 2002)). Furthermore, since stars interact almost exclusively through gravitational interactions, their orbits conserve an imprint from their formation or accretion processes, which are again unknown to us. The problem of the connection between stellar kinematics and galaxies has thus incomplete data, but the rewards for solving it are big: the dynamics of stars can provide us with a way to extrapolate the mass and potential of galaxies, and also uncover the formation processes that lead them to their current form. In this Chapter I will review the past theoretical and modelling efforts in understanding the stellar dynamics of galaxies and present the analysis tools used in my thesis work. In Chapter 2.1 I will describe how LOS stellar kinematics are treated in observations, what we can learn from them, and how we can reproduce them in simulations. In Chapter 2.2 I will describe the possible orbits of stars in a stationary galactic potential and how we can classify them. In Chapter 2.3 I will describe how the dynamics of galaxies can be modelled through the Jeans equations and used to estimate the potential and density profile of a galaxy.

2.1 Projected stellar kinematics

2.1.1 Stellar kinematics from IFU surveys

Integral field unit (IFU) spectrographs allow us to infer the spatial distribution of spectral-derived quantities (kinematics, metallicity, age,...). The velocity distribution of stars can be inferred thanks to the Doppler effect. Their spectral emission lines shift to lower or higher

wavelengths depending on their projected velocity along the line-of-sight (LOS). When observing a galaxy, each pixel of the spectrograph collects light from millions of stars, so what we observe is a distribution of these wavelength shifts, and thus a distribution of LOS-projected velocities. This distribution is typically shaped similarly to a Gaussian distribution, but often with significant deviations. The most common way used to describe this shape is by fitting the normalized histogram of the LOS velocity distribution with a fourth-order Gauss-Hermite function (van der Marel and Franx, 1993; Gerhard, 1993):

$$f(V) = \frac{e^{-y^2/2}}{\sqrt{2\pi}\sigma}(1 + h_3\,H_3(y) + h_4\,H_4(y)) \tag{2.1}$$

where $y = (V - V_{\mathrm{avg}})/\sigma$ and H_3 and H_4 are the Hermite polynomials of third and fourth order:

$$H_3(y) = (2\sqrt{2}\,y^3 - 3\sqrt{2}\,y)/\sqrt{6} \tag{2.2}$$

$$H_4(y) = (4\,y^4 - 12\,y^2 + 3)/\sqrt{24}. \tag{2.3}$$

The four fitting parameters V_{avg}, σ, h_3 and h_4 represent the shape of the distribution. The first part of Equation 2.1 is a regular Gaussian, with average V_{avg} and size σ. The additional terms add asymmetric and symmetric deviations to this Gaussian respectively. h_3 represents the skewness of the distribution: a positive h_3 value means that there are additional stars in the high velocity tail of the distribution, and viceversa for negative h_3. h_4 represents the kurtosis of the distribution: a distribution with positive h_4 has a thinner peak and more extended tails, while negative h_4 means the distribution is flatter but with smaller tails. Figure 2.1 shows an example of a LOS velocity distribution fitted with a Gauss-Hermite formula.

The accuracy of the extraction of these kinematic parameters depends on the quality of the signal. A trick used in IFU maps to reduce this problem is to group together pixels with low signal-to-noise ratio (S/N) until the signal reaches a desired quality. A common way of grouping pixels together is the Voronoi tessellation. In its simplest form, it is defined as the subdivision of an N-dimensional space into the regions closest to a set of points, called Voronoi seeds (Voronoi, 1908). The algorithm from Cappellari and Copin (2003) performs a 2D Voronoi tessellation on the field of view of the IFU, and subdivides it in cells called 'spaxels' so that each spaxel has the same total S/N. The seed points of each spaxel are then used as the position where the spectral information extracted from the spaxel is located. This technique can be used for analysing any spectral-derived quantity, but it is especially useful for the kinematics, as high S/N is required to recover higher-order moments (h_3 and h_4). Figure 2.2 shows a typical example of stellar kinematic maps of an observed galaxy (NGC 3115, seen from the MUSE spectrograph, Guérou et al., 2016). The four panels show the four best-fitting Gauss-Hermite parameters (V_{avg}, σ, h_3, h_4) for each spaxel.

The shape of the LOS velocity distribution of each spaxel is connected to the orbital composition of the galaxy. Systems supported by random motion of stars (pressure-supported
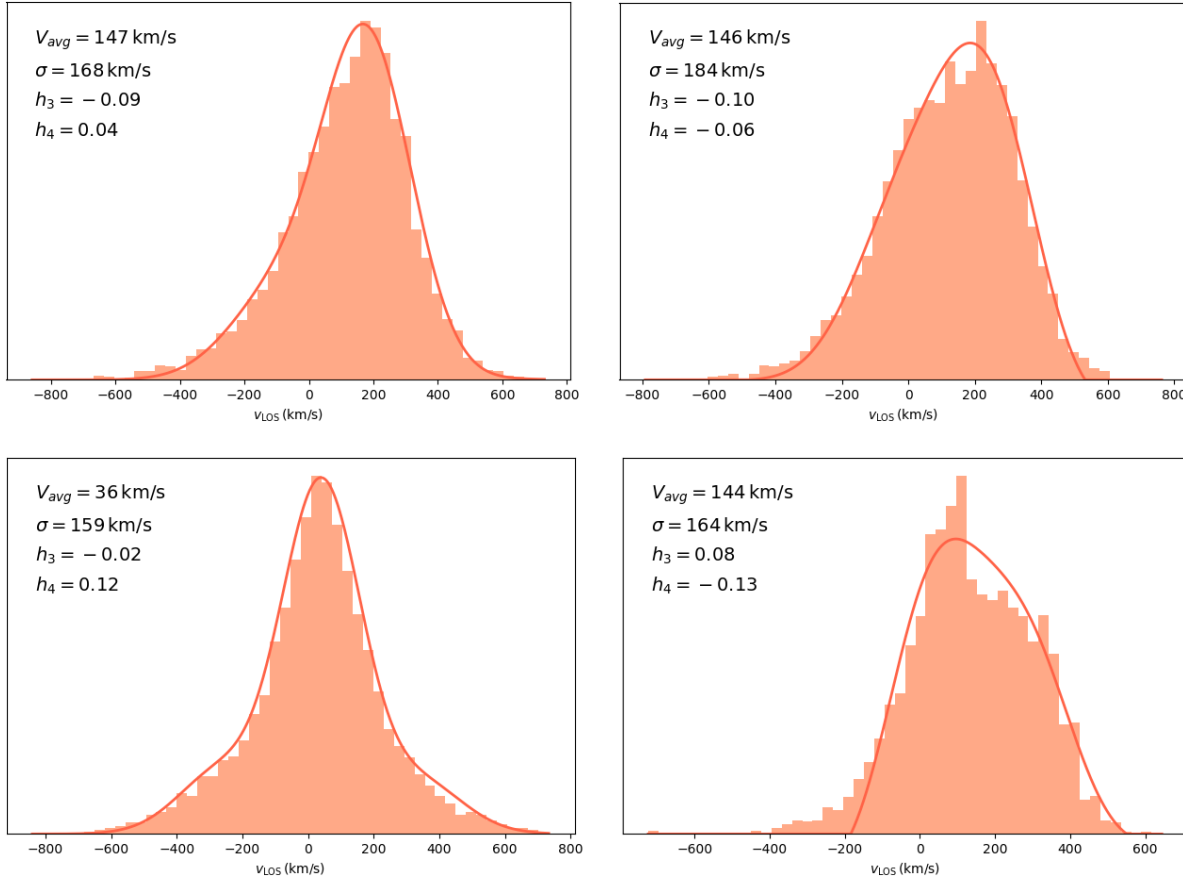
Figure 2.1: Example of four LOS velocity distributions (histogram) fit with the Gauss-Hermite formula (solid line, Eq. 2.1). The fit parameters $(V_{\mathrm{avg}},\sigma,h_3,h_4)$ are written in each panel. Each distribution is taken from a Voronoi spaxel of one of our simulations. The distribution in the top left panel is typical of a system dominated by rotational orbits, as most of the stars have negative LOS velocities except for a few stars on different orbit types, which result in an h_3 value of the opposite sign of V_{avg}. The distribution in the top right panel is also dominated by rotation, but has a larger component of other orbits with $v_{\mathrm{LOS}} \sim 0$, making σ larger, h_3 larger in absolute value and h_4 negative. The distribution in the bottom left is dominated by radial orbits, and thus is symmetric and centered at $v_{\mathrm{LOS}} \sim 0$, and has positive h_4. The distribution in the bottom right is an example of positive correlation between V_{avg} and h_3, which in this case happens because most stars are on random orbits but a sizeable few rotate orderly.
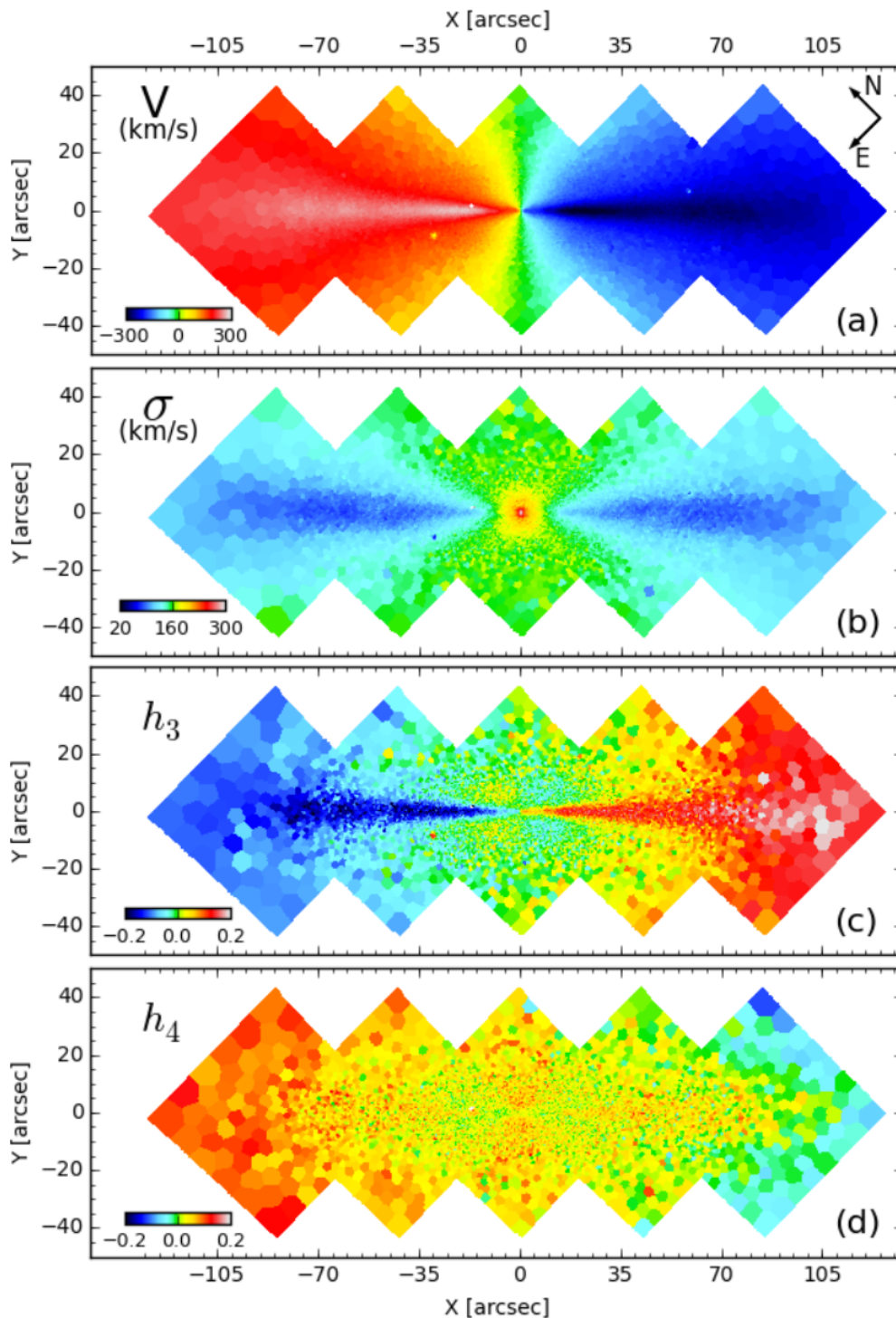
Figure 2.2: Kinematic maps of NGC3115 viewed by the MUSE spectrograph, taken from Guérou et al. (2016). The four panels from top to bottom show mean velocity, velocity dispersion, h_3, h_4. NGC3115 is an S0 galaxy, and displays clear signs of rotation, most notably the anti-correlation between the V and h_3 maps. The asymmetry in the outer parts of the h_4 map is due to a systematic error in the data reduction of the observations.

systems, like elliptical galaxies) tend to have low values of V_{avg} and high values of σ, which is typically peaked in the center where the density is higher. Systems that rotate orderly (rotation-supported systems, like spiral galaxies) will instead have symmetrically high values in the V_{avg} map, showing rotation, and have lower values of σ. Other typical features of rotating systems are the dumbbell shape in the velocity dispersion, which appears when the galaxy contains both a pressure-supported component and a rotating disk, and the anti-correlation between the h_3 map and the V_{avg} one, due to the low-velocity tail of stars that do not move along the LOS (this will be explained more in detail in Chapter 2.1.3). The galaxy in Figure 2.2 is an example of all of these features. h_4 is also connected to the orbital structure of the system, in that it roughly correlates to orbit anisotropy (van der Marel and Franx, 1993; Gerhard, 1993; Thomas et al., 2007). Negative h_4 values indicate the dominance of tangential orbits, while positive h_4 values correspond to radial orbits. This is in principle very useful, as the anisotropy of a stellar system is otherwise unknown, but the specific value of h_4 also depends on other factors, such as inclination (Thomas et al., 2007), making this connection harder.

2.1.2 Connection to physical properties of galaxies

Observationally, galaxies have been kinematically separated into two categories, slow-rotators and fast-rotators, with very different properties. Slow-rotators tend to have larger masses, higher metallicities, higher stellar ages and more 'boxy' isophotes, while fast-rotators tend to be less-massive young 'disky' systems. The most popular parameter employed to distinguish these two classes is λ_R (Emsellem et al., 2007), which is an adimensional proxy for the projected angular momentum of the galaxy. It is defined as:

$$\lambda_R = \frac{\sum_i F_i R_i |V_i|}{\sum_i F_i R_i \sqrt{V_i^2 + \sigma_i^2}}, \tag{2.4}$$

where the sum has been carried out over the spaxels of the kinematic maps, and F_i, R_i, V_i and σ_i are the flux, projected radius, average LOS velocity, and velocity dispersion of each spaxel, respectively. λ_R can range in value from 0 (pressure-supported system) to 1 (pure rotation-supported system). Figure 2.3 shows the λ_R values (within R_{e}) of a selection of galaxies from the SAMI survey (van de Sande et al., 2017), as a function of their ellipticity ϵ. This type of plot is commonly used to distinguish slow- and fast-rotators. According to Cappellari (2016), a galaxy is considered a slow-rotator when:

$$\lambda_R < 0.08 + 0.25\,\epsilon \quad \text{with} \quad \epsilon < 0.4. \tag{2.5}$$

The reason for the cut in ϵ is that we want to exclude galaxies with counter-rotating disks, which could have λ_R values typical of slow-rotators despite actually being a rotation-supported system. Looking at Figure 2.3 we can see that slow- and fast-rotators form two different sequences in the plot: slow-rotators have low values of λ_R even when they have relatively high values of ϵ while fast-rotators increase their λ_R rapidly with ϵ. For a given

fast-rotating galaxy λ_R and ϵ are biggest when the galaxy is seen in edge-on projection, and changing the inclination the values move along the sequence towards $\lambda_R = 0$, $\epsilon = 0$. Slow-rotators can have a more complex structure. With the KINEMETRY software (Krajnović, 2014), Krajnović et al. (2011) analyzed the regularity of the rotation of galaxies using IFU data. They found that fast-rotators are generally regular rotators, meaning that their velocity map is well represented by a simple $V = V_{rot} \cos\theta$ law, with V_{rot} being the amplitude of rotation and θ the eccentric anomaly. Slow-rotators instead are not well represented by this law and they can have a variety of more complex structures: kinematically-decoupled cores, kinematic twists, double dispersion peaks,... This complexity suggests that slow-rotators had a different kind of formation history, dominated by galaxy mergers instead of isolated in-situ star formation.

Simulations helped make this connection clearer. Generally, stars that form in-situ tend to have tangentially biased orbits and rotate orderly, because the gas that forms them collapses into disk-like shapes due to dissipation. Stars that were accreted from other galaxies instead tend to be radially-biased, and form pressure-supported systems with complex kinematics. Merger events can scramble orderly-rotating systems and turn them into pressure-supported ones. However, merger events can have many variables (mass ratio, impact parameter,...), and the availability of star-forming gas is impacted by many factors, such as energy feedback mechanisms (Supernovae, AGNs,...), making for a very complex picture. Naab et al. (2014) used cosmological simulations to connect the $z = 0$ kinematics of simulated galaxies to the type of formation history they went through, and found 6 different types:

- (A) Fast-rotators formed from gas-rich minor mergers.

- (B) Fast-rotators formed from late gas-rich major mergers.

- (C) Slow-rotators formed from late gas-rich major mergers, with central rotating regions causing a dip in the σ map.

- (D) Fast-rotators formed from late gas-poor major mergers, with a complex structure and relatively weak anti-correlation between h_3 and V_{avg}/σ.

- (E) Slow-rotators formed from late gas-poor major mergers, with an elongated shape.

- (F) Slow-rotators formed from gas-poor minor mergers, with a round shape.

Most notably, gas-rich major mergers can result in both fast- (B) and slow-rotators (C), depending on the orbital angular momentum of the merging galaxies. Similarly, while most gas-poor major mergers leave slow-rotating remnants (E), they can also result in fast-rotators (D). In real galaxies the situation could be even more complex, as these simulations did not include every known feedback mechanism (most notably, AGN feedback).
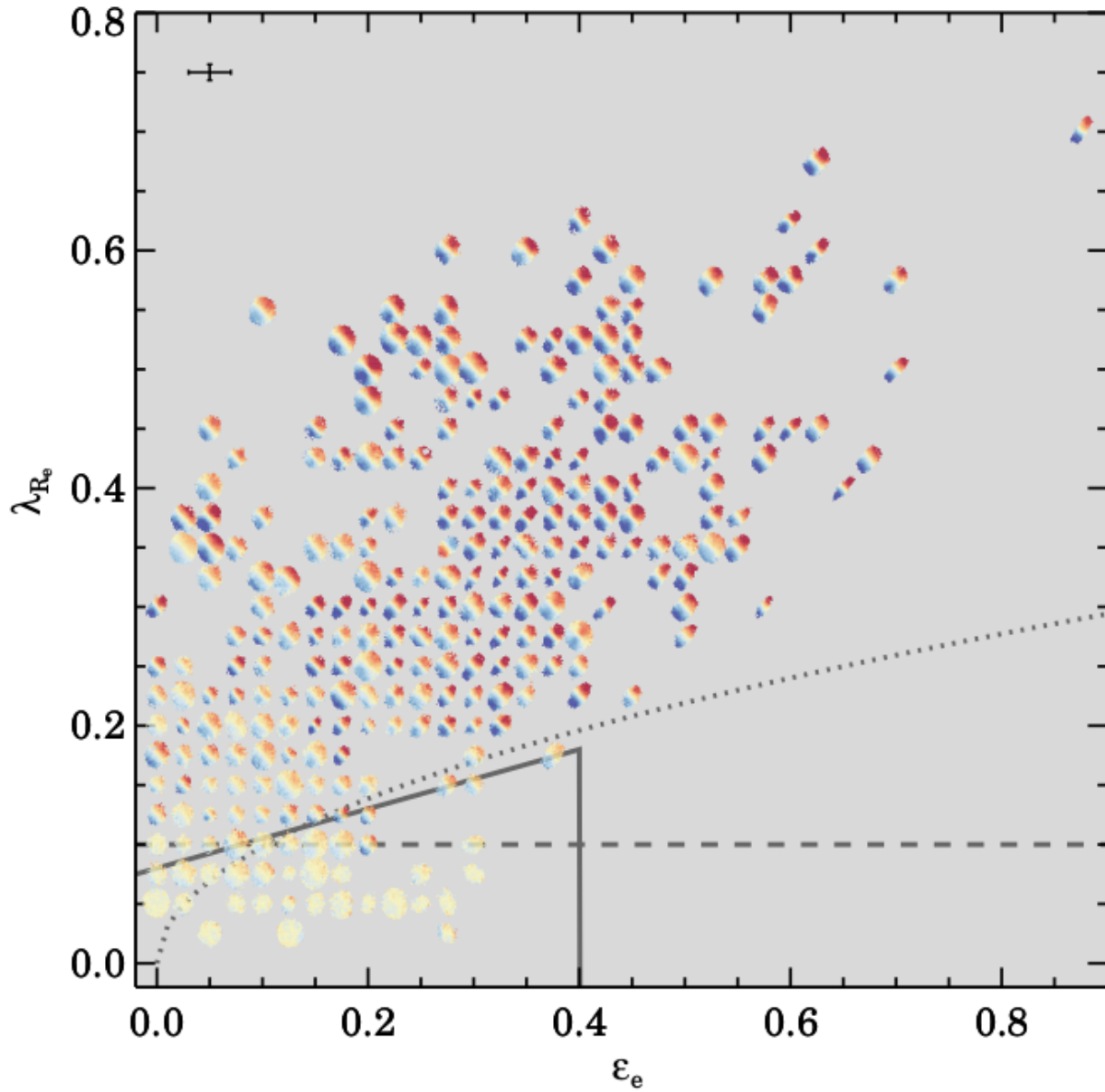
Figure 2.3: Distribution of observed galaxies from the SAMI survey in the λ_R - ϵ plane, taken from van de Sande et al. (2017). Each galaxy is marked by its velocity map. The solid line divides slow-rotators and fast-rotators according to the Cappellari (2016) criterion (Eq 2.5). The dashed and dotted lines are less recent criteria.

2.1.3   Higher-order kinematics

The higher-order moments of the LOS velocity distribution, h_3 and h_4, can provide additional information on the orbital structure of our galaxies. In rotating systems the h_3 parameter has been observed to be anti-correlated to the average LOS velocity V_{avg}, or more specifically to the V_{avg}/σ ratio (Gerhard, 1993; Krajnović et al., 2011; Veale et al., 2017; van de Sande et al., 2017). This anti-correlation indicates that the LOS velocity distributions typically have a steep leading wing and a broad trailing wing. Simple axisymmetric rotating stellar systems show this property due to projection effects - stars are typically on circular orbits and those with lower LOS velocities projected into each spaxel produce a broad trailing wing. The slope of this anti-correlation is then about 0.1 (Bender et al., 1994). However, if the galaxy is more complex, i.e not axisymmetric, it can also contain stars orbiting around different axes or radial orbits. This can make the trailing wing broader, as these stars have lower LOS velocities. The slope of the anti-correlation would then be steeper, and in some slow-rotating galaxies it can become extremely steep (see e.g. van de Sande et al., 2017). If the group of rotating stars becomes sub-dominant the correlation between h_3 and V_{avg} / σ can change sign and become positive. Here the few fast rotating stars create a broad leading wing in the LOS velocity distribution (Naab et al., 2006; Hoffman et al., 2009; Röttgers et al., 2014). This unusual property is typically seen in simulated gas poor mergers Naab and Burkert (2001) and Naab et al. (2014).

We characterize this variety of behaviours with a global parameter indicating the slope of the relation between h_3 and V_{avg} / σ for all spaxels of one galaxy. This definition is inspired by the finding in Naab et al. (2014) that different slopes indicate varying formation histories and by the improved empirical classifications of the SAMI and MASSIVE galaxy surveys (van de Sande et al., 2017; Veale et al., 2017). We define ξ_3 as:

$$\xi_3 = \frac{< h_3 \cdot V_{\text{avg}}/\sigma >}{< h_3^2 >} = \frac{\sum_i F_i \, h_{3,i} \cdot (V_i/\sigma_i)}{\sum_i F_i \, h_{3,i}^2}, \tag{2.6}$$

where the sum is calculated over each spaxel out to R_{e} from the center. When h_3 and V_{avg}/σ are correlated, this parameter estimates the inverse of the slope of the correlation to reasonable accuracy with a simple fraction of weighted sums; negative values indicate a negative correlation, while positive values indicate a positive one. This can be seen by assuming $< h_3 >= 0$ and $< V_{\text{avg}}/\sigma >= 0$ and rewriting the definition of the parameter as:

$$\xi_3 = \rho_{V/\sigma, h_3} \, \frac{\sigma_{V/\sigma}}{\sigma_{h_3}}, \tag{2.7}$$

where $\rho_{V/\sigma, h_3}$ is the Pearson (1895) correlation coefficient of V_{avg}/σ and h_3, and $\sigma_{V/\sigma}$ and σ_{h_3} are the dispersion values of the two parameters. If h_3 and V_{avg}/σ are linearly correlated then $\rho = \pm - 1$, and ξ_3 becomes exactly the slope of the correlation. Figure 2.4 shows an example of the h_3 - V_{avg} / σ spaxel values within R_{e} for four simulated galaxies with different LOS velocity distribution properties. The lines indicate the simple slope given by $h_3 = (1/\xi_3) \cdot V_{\text{avg}}/\sigma$. Purely rotating systems are expected to have $\xi_3 \sim -10$ or lower, while rotating systems with non-negligible fractions of different orbit types are expected to

lie in the $-3 < \xi_3 < -6$ range. When there is no correlation, or when the slope is almost vertical (both of which are observed in slow-rotating galaxies), the value of ξ_3 comes close to zero. Additionally, the dependence of ξ_3 on inclination seems to be weaker than other kinematic global parameters, making it potentially a good way of distinguishing different types of galaxies. In Section 4.2.2 we investigate inclination effects and show how this parameter correlates with other galaxy properties. van de Sande et al. (2017) have used best fitting elliptical Gaussians with a maximum log-likelihood approach to characterize the slope of the relation, which is slightly more complicated than our procedure. Veale et al. (2017) perform linear least square fits to calculate the slopes directly. Using the inverse of the slopes highlights the difference between slow rotators and the slow rotators get values around zero.

2.1.4 Kinematic maps in simulations

In my thesis projects I mock the observation and analysis of IFU stellar kinematic maps on simulated galaxies. These maps are constructed with a Python code developed for these thesis projects, following the analysis presented in Jesseit et al. (2007), Jesseit et al. (2009), Röttgers et al. (2014), and Naab et al. (2014). The code is included in the publicly available PYGAD analysis package [1]. Positions and velocities of the simulated galaxies are centered on the densest nuclear regions using a shrinking sphere technique on the stellar component. In the *AGN* simulations we center the galaxies on their central super-massive black hole particles, which we define as the most massive black hole particle within 1 kpc of the stellar density center. We then calculate the eigenvectors of the reduced inertia tensor (Bailin and Steinmetz, 2005) of all stellar particles within 10 % of the virial radius, and use them to align the galaxies' principal axes with the coordinate systems, such that the x-axis is the long axis and the z-axis is the short axis. To mimic seeing effects, each star particle in the simulation is split into 60 'pseudo-particles', which keep the same velocity as the original particle and the positions are distributed according to a Gaussian with $\sigma = 0.2$ kpc centered on the original position of the particle (see Naab et al., 2014). In projection, the pseudo-particles are mapped onto a regular two-dimensional grid, with pixel size 0.1 kpc (at $z = 0$). Adjacent bins of this grid are then joined together according to a Voronoi tessellation, using the Cappellari and Copin (2003) algorithm, so that each spaxel has similar S/N. In our simulations this means the same total stellar mass or luminosity, and the specific value depends on the project. The Voronoi grid is then used to construct the plots of stellar kinematics, metallicity and age shown in this thesis. For the age and metallicity maps, the value of every spaxel is calculated through a mass-weighted sample average. For the kinematic maps, we construct a histogram of the LOS velocity distribution of each spaxel, with the bin size determined by the Freedman and Diaconis (1981) rule. We then fit the histogram with the Gauss-Hermite function (Eq. 2.1) to derive the four fitting parameters V_{avg}, σ, h_3 and h_4, which we plot in the four panels of the kinematic maps. Using these values we also compute λ_R and ξ_3 always within R_{e}.

---

[1] https://bitbucket.org/broett/pygad
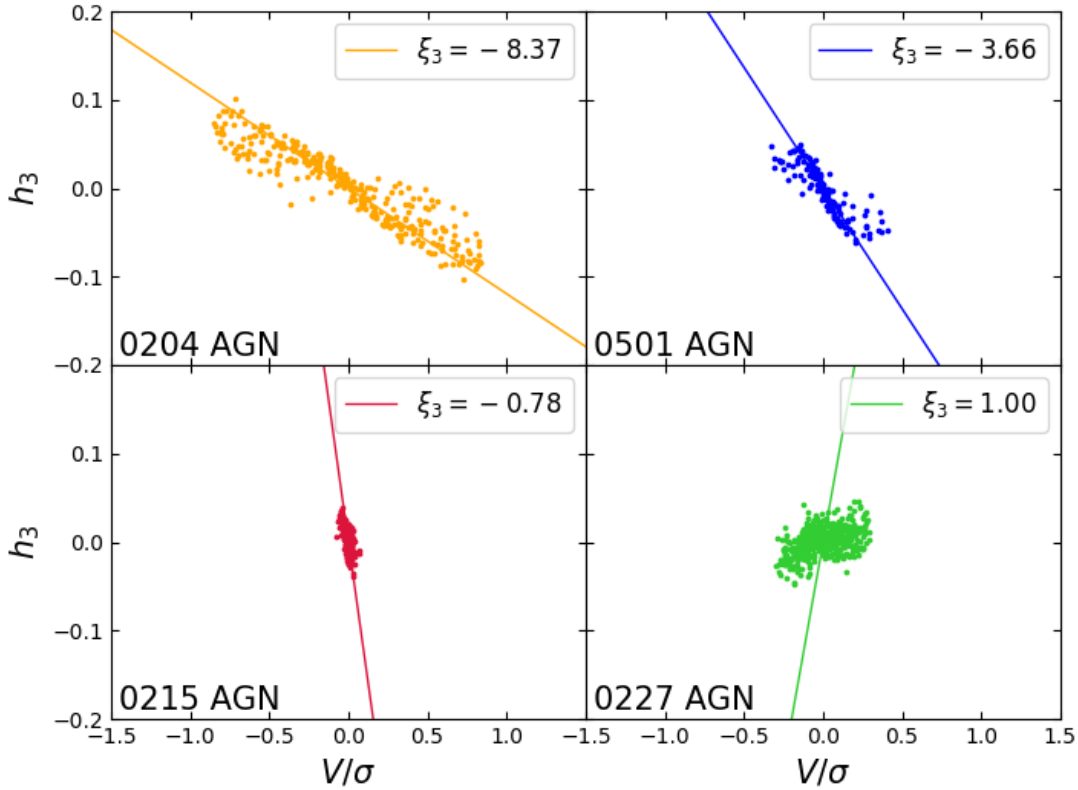
Figure 2.4: Four simulation examples for the relation between h_3 and V_{avg}/σ for the Voronoi bin within R_{e} with the corresponding ξ_3 values. The lines indicate $h_3 = (1/\xi_3) \cdot V_{\mathrm{avg}}/\sigma$. A typical axisymmetric fast rotator (0204 AGN) is shown in the upper left plot. It has the most negative ξ_3 value. The more complex fast rotator 0501 AGN (upper right panel) shows a steeper slope with a higher ξ_3. Slow rotators like 0215 AGN (bottom left panel) have ξ_3 close to zero. Unusual non-axisymmetric rotating systems like 0227 AGN have a weak positive correlation between h_3 and $V_{\mathrm{avg}}/\ \sigma$ resulting in a slightly positive value of ξ_3 (bottom right panel).

2.2 Stellar orbits

So far we looked at the directly-observable projected kinematics of stellar systems. Despite the wealth of information they can bring, something is inevitably lost in the projection along the line-of-sight. Each star moves on a specific tridimensional orbit with many possible shapes, and which is linked to the other properties of the galaxy. Here we will have a theoretical look at what kind of orbits are possible and how we can classify them in simulations. For a more thorough review, see Chapter 3 of Binney and Tremaine, 2008.

2.2.1 Hamiltonian description of orbits

The possible stellar orbits in a given galaxy are inextricably linked to the shape of its gravitational potential. A lot of their properties are determined by the integrals of motion available in that given potential. An integral of motion is a function of the phase-space coordinates $(\vec{x}, \vec{v})$ which is conserved along an orbit:

$$I(\vec{x}(t_1), \vec{v}(t_1)) = I(\vec{x}(t_2), \vec{v}(t_2)) \tag{2.8}$$

for any t_1, t_2. The dimensionality of an orbit, i.e. the number of dimensions in phase-space where the orbits lives, is given by $2n - i$, where n is the number of spatial dimensions and i the number of independent integrals of motion for this orbit. If there are at least three integrals, the motion in this potential can be described through action-angle canonical coordinates:

$$\dot{\theta}_i = \frac{\partial H}{\partial I_i} \equiv \Omega_i(\vec{I}) \tag{2.9a}$$

$$\dot{I}_i = -\frac{\partial H}{\partial \theta_i} = 0, \tag{2.9b}$$

where the Hamiltonian $H(\vec{x}, \vec{v}) = v^2/2 + \Phi(\vec{x}) = H(\vec{I})$ only depends on the three integrals. The action coordinates are integrals of motion and therefore constant, and the angle coordinates θ vary linearly with time with specific frequencies Ω_i, called fundamental frequencies. This makes the spatial motion of the particle $\vec{x}(t)$ expandable in a Fourier series with frequencies related to the fundamental ones; an orbit of this kind is called quasi-periodic. If there are more integrals of motion than three, the orbit is further constrained into less dimensions. This can for instance happen when there are resonances between the fundamental frequencies.

Any orbit that can be represented through action-angle variables is called a *regular* orbit. If however this is not possible, because the number of integrals is less than n (three), the orbit is considered *irregular*. In realistic gravitational potentials large regions of phase-space are populated by irregular orbit, which wander through phase-space in a process called Arnold diffusion. Irregular orbits however cannot cross the regions of phase-space where regular orbits live, thus constraining their motion to some degree. Irregular orbits that are very near regular regions of phase-space are called *sticky* orbits, and they behave similarly to the orbits in that regular region for many periods, but eventually manifest their irregular nature.

2.2.2   Permitted orbit types in a given potential

A number of integrals of motion are always available, depending on the properties of the potential, and this allows or forbids certain kinds of orbit. When the potential is static, the Hamiltonian is always an integral of motion. If the potential is also spherically-symmetric there are at least four integrals of motion: the Hamiltonian and the three components of the angular momentum. Therefore all possible orbits are not only periodic, but also move within a plane. If the orbit is bound, then the distance of the star from the center of the potential oscillates between an inner radius, called the apocenter, and an outer radius, called the pericenter. The periods of radial and azimuthal motion are generally independent, generating a rosette-shaped orbit. If the ratio between the periods is integer, then the frequencies are resonant and the orbit is closed, otherwise it is open. If the frequencies are equal (like in the case of a Keplerian potential), the orbit is an ellipse.
A spherically symmetric potential can be a good representation for globular clusters, for the surroundings of a super-massive black hole and for a few spherically-shaped galaxies, but in general galaxies have more complex shapes. An axysymmetric potential has at least three integrals of motion (H, L_z, and a third integral I which depends on the system), and the possible orbits are confined in a two-dimensional region in the meridional plane $R - z$, circulating around the origin.

If we allow for all axes to have different lengths, like in the case of a perfect ellipsoid[2], there are four possible kinds of orbits: box orbits, z-tubes and inner and outer x-tubes. *Box* orbits are confined in a rectangular box and do not have a particular sense of circulation around the origin. Particles on these orbits move radially and stop for a brief moment when they reach the furthest extent of their orbit. *Z-tube* orbits, or short-axis orbits, rotate around the z (short) axis of the galaxy in a fixed direction, and are analogous to the orbits available in an axisymmetric potential. *X-tube* orbits rotate around the x (long) axis, and they can be further divided into outer and inner x-tubes, depending on if they move along the x axis or not. X-tube orbits are only permitted if the potential is prolate or triaxial. Orbits that rotate around the y (intermediate) axis are always unstable. Figure 2.5 shows an example of these different orbit types, taken from Röttgers et al. (2014). If the potential is only approximately triaxial, all of these orbit types are possible, but additionally there can be many irregular orbits.

2.2.3   Classifying orbits from simulations

As previously discussed in Chapter 2.2.1, the motion of regular orbits has a discrete Fourier transform, with frequencies that are linear combinations of the fundamental frequencies. This means that if the spatial motion of a particle is known, the frequencies can be recovered

---

[2]Given by the density distribution:

$$\rho(x, y, z) = \frac{\rho_0}{1 + m^2}, \; m^2 = \frac{x^2 + (y/q_1)^2 + (z/q_2)^2}{a_0^2} \tag{2.10}$$
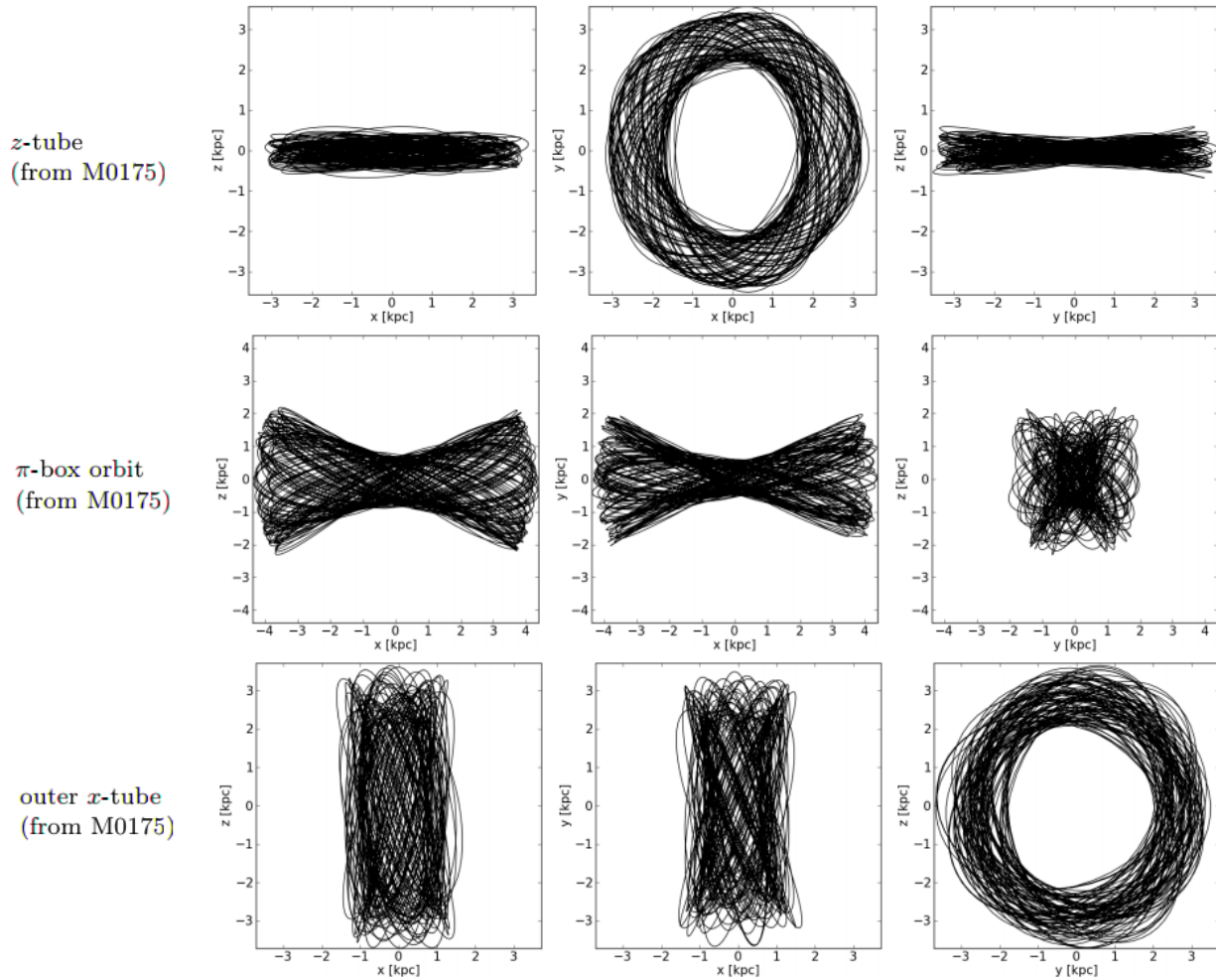
Figure 2.5: Examples of different kinds of orbits, taken from Röttgers et al. (2014). The top row shows a z-tube orbit, projected along the three principal axes. The middle and bottom rows show the same for a box orbit and for an x-tube orbit.

		Number of base frequencies			
		1	**2**	**3**	**4 or more**
Number of resonances	**0**	axial	2–D π–box	3–D π–box	irregular
	1	closed 0:m:n box^a closed 0:1:1 loop	thin π:m;n box thin π:1:1 tube	open π:m:n box open π:1:1 tube	
	3	closed l:m:n box closed l:1:1 tube	thin l:m:n box thin l:1:1 tube	open l:m:n box open l:1:1 tube	

^{a} The order of the indices does not change the classification name, just the spatial orientation.

Table 2.1: Summary of the Carpintero and Aguilar (1998) orbit classification scheme. π here indicates an irrational ratio between frequencies (no resonance).

through Fourier analysis, and from them the type of orbit can be inferred. In my project I analyze the orbital structure of simulated galaxies by, among other things, classifying the orbits of each specific star. In doing this we follow the approach of Jesseit et al. (2005) and Röttgers et al. (2014). This procedure starts by freezing the potential of the simulated galaxy at $z = 0$ and representing it analytically using the self-consistent field method (Hernquist and Ostriker, 1992): the density and potential are expressed as a sum of bi-orthogonal basis functions, which satisfy the Poisson equation. There are multiple such density-potential pairs. We used the one from Hernquist and Ostriker (1992), in which the zeroeth-order element is the Hernquist (1990) profile:

$$\rho_{000} = \frac{M}{2\,\pi\,a^3} \frac{1}{\frac{r}{a}(1 + \frac{r}{a})^3} \tag{2.11}$$

$$\Phi_{000} = -\frac{G\,M}{r + a}, \tag{2.12}$$

where a is the scale parameter of the Hernquist profile. Higher order terms then account for both radial and angular deviations. We then integrate the orbits of each stellar particle within this fixed analytical potential using a Runge-Kutta integrator. We do this for about 50 orbital periods, which is enough for identifying the orbit type, but not so much that quasi-regular orbits diverge from regular phase-space regions forcing us to classify them as irregular. These quasi-regular orbits are known as 'sticky' orbits, and while mathematically irregular, they can be regular during a galaxy's timescale.

The orbit classification itself is then done using the classification scheme by Carpintero and Aguilar (1998), which distinguishes different orbit families by looking at the resonances between their frequencies along different axes, obtained through Fourier analysis. This is summarized in Table 2.1. If there is a 1:1 resonance between the x and y frequencies,

then the orbit is classified as z-tube. If there is a 1:1 resonance between y and z it is classified as an x-tube. X-tubes can also be distinguished between inner and outer based on whether their orbit is convex or concave along the x axis, but in our analysis we do not distinguish them. Box orbits can have no resonances ($\pi-$box) or resonances different from 1:1 (boxlet).The number of base frequencies determines whether box and tube orbits are closed, thin (the orbit lives in a 2D manifold in configuration space) or open. If the analysis finds that the orbit has more fundamental frequencies than three, then these are not fundamental frequencies at all and the orbit is irregular. Each computed orbit is divided into three sections, and the analysis is done independently for each of them. If the classification for the three sections does not match, we consider it 'not classified'. In addition to these, we also distinguished prograde and retrograde z-tube orbits, depending on whether their angular momentum along the z-axis aligns with the overall galaxy or not.

2.3   Dynamical modelling

The link between a galaxy's potential and its stellar kinematics can also be used the other way around: to determine the mass and density profile of galaxies using the observed kinematics. There are two main possible approaches for doing this. One, Schwarzschild modelling, consists in constructing linear combinations of orbits of different types to create projected LOS velocity distribution that can be compared with the observed one. This allows to constrain at the same time the mass and the orbital structure of the system, but is very computationally expensive. Here we will present a simpler approach, Jeans modelling, in which dynamical models are constructed from basic properties of gravitational systems under a certain set of assumptions. For a more complete derivation, see Chapter 4 of Binney and Tremaine (2008).

2.3.1   Collisionless gravitational systems

A stellar system can be considered *collisionless*, meaning that two-body interactions are rare, and the potential can be approximated with a smooth function, as opposed to a set of point-like potential wells. The time it takes for an orbit calculated in the smooth potential to diverge from the real-orbit because of two-body interactions is the two-body relaxation time. For a globular cluster the relaxation time is of order $t_{\text{relax}} \sim 1\,\text{Gyr}$, but for a galaxy it is far longer than the age of the universe, meaning that galaxies can be treated as collisionless. We can then treat the stars as a 'fluid' and describe the evolution of this stellar fluid in phase-space using the collisionless Boltzmann (or Vlasov) equation:

$$\frac{\partial f}{\partial t} + \dot{\vec{q}} \cdot \frac{\partial f}{\partial \vec{q}} + \dot{\vec{p}} \cdot \frac{\partial f}{\partial \vec{p}} = 0, \tag{2.13}$$

where $f(\vec{x}, \vec{v}, t)$ is the distribution function of this fluid and q and p are two canonical coordinates. This is a consequence of the conservation of phase-space volume (Liouville's

theorem), and holds true for any two canonical coordinates. For cartesian coordinates $(\vec{x}, \vec{v})$ it can be written as:

$$\frac{\partial f}{\partial t} + \vec{v} \cdot \frac{\partial f}{\partial \vec{x}} - \frac{\partial \Phi}{\partial \vec{x}} \cdot \frac{\partial f}{\partial \vec{v}} = 0, \tag{2.14}$$

where $\Phi(\vec{x})$ is the potential. If we integrate Eq. 2.14 over all velocities we obtain for each coordinate i:

$$\frac{\partial \nu}{\partial t} + \frac{\partial(\nu \overline{v}_i)}{\partial t} = 0, \tag{2.15}$$

where $\nu(\vec{x}) = \int f d^3 \vec{v}$ is the spatial density of the stellar fluid and $\overline{v}$ is the mean stellar velocity. If we multiply Eq. 2.14 by $\vec{v}$ and then integrate over all velocities, we obtain:

$$\nu \frac{\partial \overline{v}_j}{\partial t} + \nu \overline{v}_i \frac{\partial \overline{v}_j}{\partial x_i} + \frac{\partial(\nu \sigma_{ij}^2)}{\partial x_i} = -\nu \frac{\partial \Phi}{\partial x_j}, \tag{2.16}$$

where $\sigma_{ij}^2 = \overline{v_i v_j} - \overline{v}_i \overline{v}_j$ is the velocity dispersion tensor. The line-of-sight velocity dispersion can be derived from it through a relatively simple projection[3]. Equations 2.15 and 2.16 are known as the Jeans equations (Jeans, 1922), and they are very useful because they relate the potential of the system with observable kinematic properties. They are however incomplete, and require further assumptions in order to be used.

2.3.2 Jeans models

In my project I model the kinematics of our simulated galaxies using the Jeans equations under a set of assumptions. The two main assumptions are that the system is stationary ($\partial f / \partial t = 0$, $\partial \Phi / \partial t = 0$) and axisymmetric ($\partial f / \partial \phi = 0$, $\partial \Phi / \partial \phi = 0$). The latter of these two assumptions is especially strong, as many galaxies (including several in our simulated sample) are believed to have a triaxial shape. Using cylindrical coordinates (R, z, ϕ) and applying these two assumptions, Eq. 2.16 can be rewritten as:

$$\frac{\partial(\nu \overline{v_R^2})}{\partial R} + \frac{\partial(\nu \overline{v_R v_z})}{\partial z} + \frac{\nu \overline{v_R^2} - \nu \overline{v_\phi^2}}{R} = -\nu \frac{\partial \Phi}{\partial R} \tag{2.18a}$$

$$\frac{\partial(\nu \overline{v_z^2})}{\partial z} + \frac{\partial(\nu \overline{v_R v_z})}{\partial R} + \frac{\nu \overline{v_R v_z}}{R} = -\nu \frac{\partial \Phi}{\partial z} . \tag{2.18b}$$

The equation for the third coordinate (ϕ) vanishes under the assumption of axisymmetry. These assumptions are however not enough to close the system yet, and some further assumption must be made on the velocity anisotropy. In this project I employed the JAM (Jeans Anisotropic Model, Cappellari (2008)) code[4], which solves the axisymmetric Jeans

---

[3]If σ_{LOS} is the LOS velocity dispersion, x_{LOS} the component of $\vec{x}$ along the line of sight and $\vec{v}_{LOS}$ the average LOS velocity, then:

$$\sigma_{LOS}(\vec{x}) = \frac{\int dx_{LOS} \, \nu (\hat{s} \cdot \vec{\vec{\sigma}} \cdot \hat{s} + (\hat{s} \cdot \overline{\vec{v}}(\vec{x}) - \overline{v}_{LOS})^2)}{\int dx_{LOS} \, \nu}, \tag{2.17}$$

where $\hat{s}$ is the unit vector in the direction of the line-of-sight and $\hat{s} \cdot \vec{\vec{\sigma}} \cdot \hat{s} \equiv \sum_{ij} \hat{s}_i \sigma_{ij}^2 \hat{s}_j$.

[4]Available at https://www-astro.physics.ox.ac.uk/ mxc/software/

equations with two further assumptions:

- that the velocity ellipsoid is aligned with the cylindrical coordinate system, so that the velocity dispersion tensor is diagonalized.

- that the anisotropy on the meridional plane b is a constant:

$$\overline{v_R^2} = b\overline{v_z^2}.$$

(2.19)

Applying these final assumptions, the Jeans equations become:

$$\nu\overline{v_z^2}(R, z) = \int_z^\infty \nu \frac{\partial \Phi}{\partial z} dz$$

(2.20a)

$$\nu\overline{v_\phi^2}(R, z) = b\left(R\frac{\partial \nu\overline{v_z^2}}{\partial R} + \nu\overline{v_z^2}\right) + R\nu\frac{\partial \Phi}{\partial R}.$$

(2.20b)

The stellar density ν needs to be derived from the observed stellar luminosity, while the potential needs to be calculated from an assumed total density profile ρ. In the JAM code both the stellar density and the total density are parametrized through the Multi-Gaussian Expansion (MGE) formalism (Emsellem et al., 1994; Cappellari, 2002). MGE represents the surface brightness of galaxies with a sum of 2D gaussians with variable intensity L_k, dispersion σ_k, and flattening Q_k:

$$\Sigma(X, Y) = \sum_{k=1}^N \frac{L_k}{2\pi\sigma_k^2 Q_k} \exp\left(-\frac{1}{2\sigma_k^2}(X^2 + Y^2/Q^2)\right),$$

(2.21)

where X and Y are the coordinates on the plane of the sky. This surface brightness (or density) can be deprojected into:

$$\nu(R, z) = \sum_{k=1}^N \frac{L_k}{(\sqrt{2\pi}\sigma_k)^3 q_k} \exp\left(-\frac{1}{2\sigma_k^2}(R^2 + z^2/q^2)\right).$$

(2.22)

The three-dimensional flattening of the Gaussians depends on the inclination of the galaxy with respect to the line-of-sight, i:

$$q_k = \frac{\sqrt{Q_k - cos^2 i}}{sin\, i}.$$

(2.23)

The total density (luminous + dark) can be represented by the deprojected luminosity MGE multiplied by a mass-to-light ratio or by fitting a one-dimensional MGE model to a radial density profile (e.g. Hernquist (1990) or Navarro et al. (1997)) or by a sum of both. The potential of a point mass can also be added in the center to represent a supermassive black hole. Projecting Eq. 2.20 along the line-of-sight we get an expression of the root mean squared velocity along the line-of-sight V_{rms} as a function of the position in the
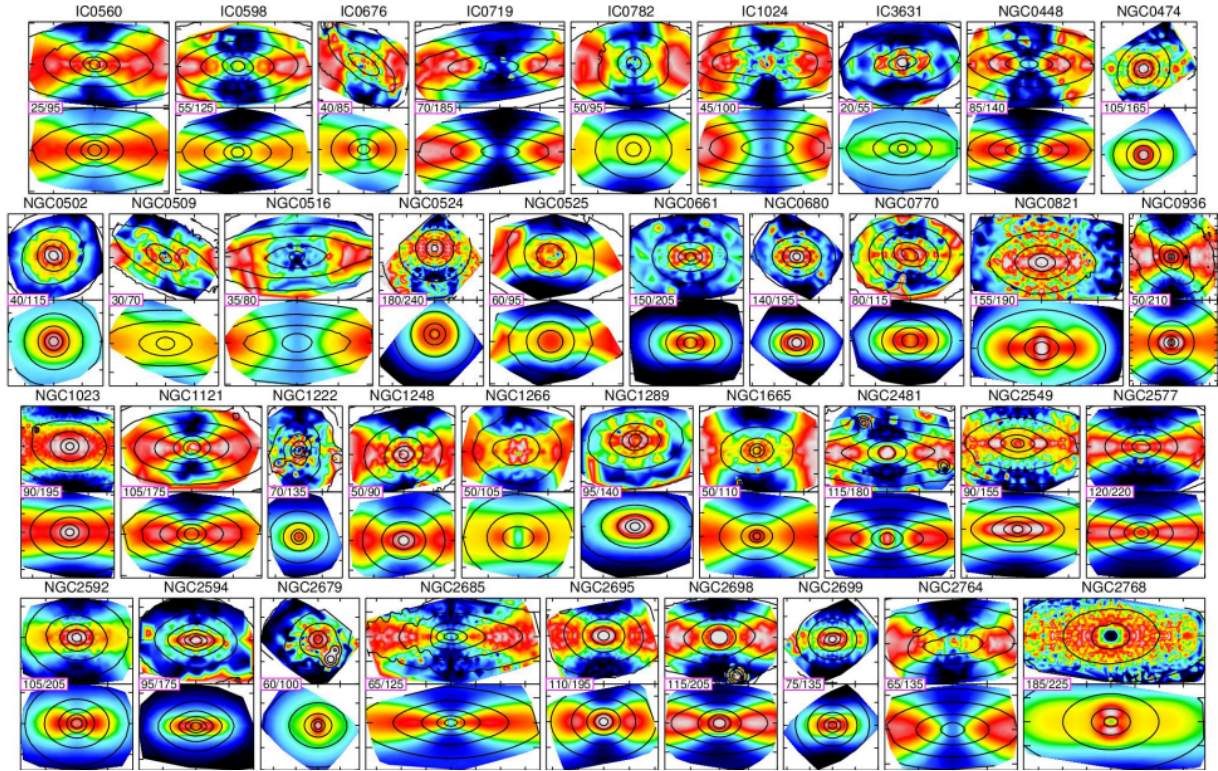
Figure 2.6: V_{rms} maps of observed galaxies from the ATLAS^{3D} survey compared with their best fitting JAM models, taken from Cappellari et al. (2013a). For each galaxy the top panel is the observed map and the bottom panel is the dynamical model.

plane of the sky. The full derivation can be found in Cappellari (2008). This V_{rms} from the Jeans model can be compared with the observed $V_{\mathrm{rms}} = \sqrt{V^2 + \sigma^2}$ from an IFU kinematic map. Then by varying the parameters of the model (inclination i, anisotropy b, and the parameters of the mass model) we can find the ones that result in the best fitting V_{rms}. The parameters of the mass model then give us an estimate for the galaxy's density profile. Figure 2.6 shows many examples of V_{rms} maps from observed galaxies from the ATLAS^{3D} survey (Cappellari et al., 2013a) compared with its best fitting JAM model. In this project only the stellar kinematics are used, but Jeans modelling can be used for any kinematic tracer, using the corresponding surface brightness for ν.

Chapter 3

Simulations of galaxies

All our knowledge about galaxies comes from some kind of astronomical observation. Observations are however inherently limited by the fact that the evolution of galaxies happens on timescales far longer than human observation timescales; often in fact longer than humans have existed on Earth at all. We can get a rough idea of how the distribution of galaxies evolved on a cosmological timescale because of the finiteness of the speed of light: further objects are seen further back in time. We however do not get to see a single galaxy evolve in time. This is where theory comes in. Analytical models have helped us understand some aspects of galaxy formation, but ultimately, the real universe proved too complex to be represented analytically. Computer cosmological simulations are therefore necessary to truly understand galaxy formation.

In my PhD project I try to connect the observable kinematics of simulated galaxies to their formation processes. Depending on the process being studied, different kinds of simulations are better suited. In Chapter 3.1 I present the simulation code we used in all our simulations. In Chapter 3.2 we present the zoom cosmological simulations that we use in the first two parts of my project (Chapters 4 and 5). In Chapter 3.3 I present the isolated simulations that we use in the last part of my project (Chapter 6).

3.1   Simulations with GADGET

The code we used for running the set of simulations in my project is GADGET3 (GAlaxies with Dark matter and Gas intEracT, Springel, 2005). It runs cosmological (or isolated) simulations including dark matter, gas, star and black hole particles. The cosmological framework means that many formulas in the code include a dependency on the scale parameter of the universe $a(t)$. a is computed from the Friedman-Lemaitre model for a given set of cosmological parameters. When running an isolated simulation, a is set to 1. small GADGET is a Tree-SPH code, meaning that it uses a hierarchical tree structure for computing the gravitational force and smooth-particle hydrodynamics (SPH) to compute the motion of gas particles. In addition, it includes models for star formation and for feedback from stars and black holes.

3.1.1   Computation of the gravitational force

The gravitational force acting on particle i has to be computed by summing the potentials of all other particles j:

$$f_i = -\sum_j m_i m_j \frac{\partial \psi(x_j - x_i)}{\partial x_i} . \tag{3.1}$$

The potential of each particle is calculated from the Poisson equation.

$$\nabla^2 \psi(\vec{x}) = 4\pi G \tilde{\delta}(\vec{x}), \tag{3.2}$$

if the simulation has vacuum boundary conditions. If the simulation box has periodic boundary conditions, it takes the form

$$\nabla^2 \psi(\vec{x}) = 4\pi G \left(-\frac{1}{L^3} + \sum_{\vec{n}} \tilde{\delta}(\vec{x} - \vec{n}L) \right), \tag{3.3}$$

where L is the size of the box and the sum over $\vec{n} = (n_1, n_2, n_3)$ extends over all integer triplets. The density distribution of each particle $\tilde{\delta}(\vec{x})$ is the convolution of a Dirac δ with a softening kernel. Softening makes the gravitational force weaker when two particles are closer to each other than a softening length r_{soft}. This is necessary, as the simulation particles can have very large masses, and close interactions between them would result in unrealistically strong gravitational kicks. In GADGET, the softening is done through a cubic spline kernel (Monaghan and Lattanzio, 1985):

$$\tilde{\delta}(\vec{x}) = W_3(|\vec{x}|, 2.8\, r_{soft}) \tag{3.4}$$

with

$$W_3(r, h) = \frac{8}{\pi h^3} \begin{cases} 1 - 6(r/h)^2 + 6(r/h)^3 & r/h \leq 0.5 \\ 2\,(1 - r/h)^3 & 0.5 > r/h \geq 1 \\ 0 & r/h > 1 \end{cases} \tag{3.5}$$

This way, a point mass has the potential of a Plummer (1911) sphere $-Gm/\sqrt{r^2 + r_{soft}^2}$ within r_{soft}, but acts like a normal Newtonian point mass elsewhere.

The direct summation approach of Eq. 3.1 is very expensive computationally (it scales as $\propto N^2$ if N is the number of particles). In a 'tree' code like GADGET, distant particles are grouped together to achieve a faster performance (Barnes and Hut, 1986). This grouping is done hierarchically, with the simulation box subdivided in eight equal cells, each cell further subdivided in eight smaller cells and so on. Each time the gravitational force acting on a particle is computed, the coarsest level of the tree (the 'root') is first considered for each cell. If the accuracy of this approximation is good enough, this level is kept, and the cell acts like a single particle in the center-of-mass of the particles in the cell. If the accuracy is not enough, finer and finer levels are considered until the desired accuracy is achieved. The accuracy level for force computation can be set by the user for each simulation. Using

this algorithm makes the computational cost scale as $\propto N \log N$ instead of $\propto N^2$. GADGET achieves even faster performance by including a particle mesh (PM) algorithm for long-range interactions. In a PM algorithm the simulation is represented with a grid where each cell has a density value. From this structure, the gravitational force can be computed using Fourier-transform-based methods. These Fourier transforms are computed using the FFTW library (Frigo and Johnson, 2005). Details for the hybrid Tree-PM implementation can be found in Springel (2005).

Once the force has been computed, the motion of the particle is calculated with a leapfrog integrator, which is based on a property of Hamiltonian systems. If the Hamiltonian is separable into its kinematic ($H_{kin}(\vec{p})$ and potential ($H_{pot}(\vec{x})$) parts, then the time evolution of the position and momentum coordinates in a discrete time δt can be computed independently with the so-called drift and kick operators:

$$D(\Delta t) : x_i \rightarrow x_i + \frac{p_i}{m_i} \int_t^{t+\Delta t} \frac{dt}{a^2} \tag{3.6a}$$

$$K(\Delta t) : p_i \rightarrow p_i + f_i \int_t^{t+\Delta t} \frac{dt}{a} \, . \tag{3.6b}$$

In GADGET time evolution is done with a kick-drift-kick operator for each time-step Δt:

$$U(\Delta t) = K(\frac{\Delta t}{2})D(\Delta t)K(\frac{\Delta t}{2}). \tag{3.7}$$

An important feature of GADGET is that the time-steps are variable. This means that small-scale processes which happen on short timescales can be properly resolved, while the rest of the simulation box can be computed at a lower time resolution to save resources. Particles can have smaller or larger time-steps by factors of two, so that they can synchronize together. The class of time-step to which each particle belongs depends on its acceleration. The kick-drift-kick approach with variable time-steps results in accurate integration of orbits for a small computational cost (Springel, 2005).

3.1.2   Smoothed-particle hydrodynamics

The time-evolution of gas particles must be treated differently from that of collisionless ones (stars, dark matter, black holes). A commonly used method is smoothed-particle hydrodynamics, or SPH (see Springel (2010) for a review). In this framework, gas particles act as tracers of an underlying continuous density field, the time evolution of which follows hydrodynamical equations. Each particle has a kernel $W(r, h)$ associated to it, from which the density field (or other continuous quantities) in $\vec{x}$ can be computed:

$$\rho(\vec{x}) = \sum_{j=1}^{N_{ngb}} m_j W(\vec{x} - \vec{x_j}, h_j) \, , \tag{3.8}$$

where m_j are the masses of gas particles, $\vec{x_j}$ their locations, and h_j their SPH smoothing length. The sum is performed over the nearest N_{ngb} SPH particles, called neighbours.

The smoothing length varies from particle to particle depending on the local density, so that $h_j \rho(\vec{x_j})$ = constant. In the original implementation of GADGET2 the cubic spline kernel (Eq. 3.5) was used as SPH kernel. Once the density is computed, the equation of motion for the particle can be derived from hydrodynamical equations. This classic SPH implementation however requires the density distribution to be always differentiable, which is not always the case in astrophysics. It has in fact been shown to be inaccurate in modelling discontinuities in the fluid, such as shocks and shear flow (Agertz et al., 2007; Springel, 2010). Modern SPH codes improved significantly on this problem by introducing a series of features. One is to change the base SPH quantities from density and entropy to pressure and entropy (Hopkins, 2013). In the pressure-entropy implementation pressure is evaluated from the kernel as:

$$P(\vec{x}) = \left(\sum_{j=1}^{N_{ngb}} m_j A_j^{1/\gamma} W(\vec{x} - \vec{x_j}, h_j) \right)^{\gamma} , \tag{3.9}$$

where A_j is the entropy and γ the politropic index ($P = A\rho^{\gamma}$). The equation of motion is computed from pressure and entropy, as are other thermodynamical variables (most notably, the density). This formulation results in a much better treatment of fluid mixing. Our simulations are run with SPHgal (Hu et al., 2014), a modern implementation of GADGET with a pressure-entropy formulation and other improvements. Instead of the cubic spline kernel, it uses a Wendland (1995) C_4 kernel, which has been shown to be less computationally expensive and immune to pairing instability, allowing to use a higher number of neighbouring particles (in our simulations, $N_{ngb} = 200$) and achieve higher accuracy (Dehnen and Aly, 2012). A common feature of SPH codes is artificial viscosity, which adds dissipation and generates heat and entropy. This is necessary in situations like shocks, which would otherwise be unresolved in SPH. SPHgal includes artificial viscosity and improves the criterion for when and how much it should be applied. It also includes a model for artificial thermal conductivity, which results in an even better representation of shocks. Further details of SPHgal are given in Hu et al. (2014).

3.1.3   Star formation and stellar feedback

Our simulation code includes a model for the formation of stellar populations from gas particles, representing star formation, and for stellar feedback. The stellar populations provide thermal and kinetic feedback as well as metals to the inter-stellar medium. The chemical enrichment was originally described by Scannapieco et al. (2005) and Scannapieco et al. (2006) and later improved by Aumer et al. (2013) and Núñez et al. (2017) with an updated feedback model. Gas particles are stochastically converted into star particles depending on the density of the gas, in a way that reproduces the Kennicutt-Schmidt relation (Kennicutt, 1998). To be eligible for conversion into stars, SPH particles need to have a temperature lower than $12,000\,\mathrm{K}$ and a density higher than $1.94 \times 10^{23}\,\mathrm{g\,cm^{-3}}$. The probability for conversion during a time step of δt is $1 - e^{-p_{\mathrm{SF}}}$, where:

$$p_{\mathrm{SF}} = \epsilon_{\mathrm{SFR}} \sqrt{4\pi G \rho}\, \delta t \tag{3.10}$$

and ϵ_{SFR} is set to 0.02 (see e.g. Springel, 2000). The newly-created star particles are then treated as collisionless. Each particle represents a single stellar population assuming a Kroupa (2001) initial mass function, with a given age and the metallicity of the original gas particle. This stellar population then exerts feedback to the surrounding gas. This takes the form of type Ia and II supernovae and of winds from asymptotic giant branch (AGB) stars. Supernovae Type II happen at a given time $\tau_{SNII} = 3\,\mathrm{Myr}$ after the creation of the star particles, where τ_{SNII}. This is on the short end of the typical delay time distributions for supernovae type II. Supernovae type Ia and AGB winds are added continuously every 50Myr after the star particle creation. Each event provides momentum and thermal energy to the surrounding gas. The total feedback energy is given by:

$$E = \frac{1}{2}\, m_{\mathrm{ejected}}\, v_{\mathrm{out}}^2, \tag{3.11}$$

where m_{ejected} is the mass ejected by the stellar population and v_{out} is the assumed ejecta velocity. These are determined depending on the mass, age and metallicity of the particle and on the type of event. We assume $v_{\mathrm{out}} = 4500 km s^{-1}$ for SNIa and SNII and $v_{\mathrm{out}} = 10 km s^{-1}$ for AGB stars. The ejecta mass is taken from Woosley and Weaver (1995) for SNII and from Iwamoto et al. (1999) for SNIa. This energy and mass is then added to the surrounding gas both as thermal (heating) and as momentum feedback (pushing). The relative fraction depends on the density and distance between the supernova-undergoing stellar particle and the 10 neighbouring gas particles, mimicking the evolution of blast waves (a simplified version of the three-phase model adopted in Núñez et al. (2017); see Hirschmann et al. (2017)). The feedback events also distribute metals to the surrounding gas. Eleven elements are tracked for every gas and star particle (H, He, C, N, O, Ne, Mg, Si, S, Ca, and Fe), and their abundances are used to compute the cooling rate of the gas with the yields from Karakas (2010), Iwamoto et al. (1999) and Woosley and Weaver (1995) for AGB winds and supernovae type Ia and II, respectively. All details can be found in Aumer et al. (2013), Aumer et al. (2014), and Núñez et al. (2017).

3.1.4 AGN feedback

AGN feedback is represented through the model developed by Choi et al. (2012) and used in Choi et al. (2014), Choi et al. (2015), and Choi et al. (2017). This model includes both a radiative and a kinetic (wind) component (see Naab and Ostriker, 2017 for a discussion of alternative numerical implementations). For massive galaxies this results in efficient and realistic suppression of star formation, as well as good agreement with the observed black hole mass relations and X-ray luminosities (Choi et al., 2015; Eisenreich et al., 2017). Here we summarize the most important elements used for this study. Black holes are first seeded at the center of halos exceeding a mass of $10^{11}\,M_\odot$, with an initial mass of $M_{\mathrm{BH}} = 10^5\,M_\odot$. They can then grow either by merging with other black hole particles or by accreting neighbouring gas particles according to a modified Bondi-Hoyle-Lyttleton (Hoyle and Lyttleton, 1939,

Bondi and Hoyle, 1944, Bondi, 1952) accretion rate:

$$\dot{M}_{\mathrm{BHL}} = \left\langle \frac{4\,\pi\,G^2\,M_{\mathrm{BH}}^2\,\rho}{(c_s^2 + v^2)^{3/2}} \right\rangle, \tag{3.12}$$

where M_{BH} is the mass of the super massive black hole, ρ is the density of the gas, v its relative speed and c_s is its speed of sound. The angle brackets indicate SPH kernel averaging. Of the gas particles which could be accreted, 90% are re-emitted as a wind parallel to the angular momentum of the gas next to the black hole (see Ostriker et al., 2010). This simulates the broad-line winds commonly emitted by AGN (de Kool et al., 2001; Somerville and Davé, 2015; Naab and Ostriker, 2017). The remaining 10% are accreted, increasing the mass of the black hole particle. The model also includes radiative feedback, in two forms. There is an Eddington radiation pressure force, which depends on the accretion rate and represents low energy photons providing momentum to the gas isotropically. We are also representing the higher energy X-ray photons, using the formulae from Sazonov et al. (2005) for Compton scattering. This component provides both momentum and thermal energy to the gas. As in Hirschmann et al. (2017), our simulation code differs from the one used in Choi et al. (2017) in not including metallicity-dependent heating, which was shown to have negligible impact (Choi et al., 2017).

3.1.5 KETJU - regularized integrator for accurate black hole dynamics

An important limit of simulations with GADGET is that the introduction of softening and of approximate potential calculations makes it unable to accurately resolve close encounters between particles. This is a problem when the simulation particles do not represent a population of objects, but an actual massive compact object, like in the case of a supermassive black hole. In order to have a realistic representation of the dynamics of stars interacting with supermassive black holes, we used the KETJU regularized integrator module for GADGET. Including an accurate integrator in a code for cosmological simulations allows us to represent accurately at the same time the vicinity of the black hole and the host galaxy and surrounding large scale structure, as well as interactions between these two scales. KETJU ('chain' in finnish) is presented in detail in Rantala et al. (2017), and is based on the AR-CHAIN integrator (Mikkola and Merritt, 2008). It uses modified equations of motion in which the leapfrog method yields exact results for a Newtonian two-body problem; this approach is called 'algorithmic regularization' (see Appendix A of Rantala et al. 2017 for details). In order to reduce round-off errors, the code defines the positions of particles within the regularized region as relative to each other, in the form of a chain (hence the name KETJU). This chain is constructed starting from the two particles with the strongest gravitational interaction with each other, and then adding the two particles that have the strongest interaction with the first two, and so on. Interactions between particles are then calculated in the chain coordinates. KETJU also uses an extrapolation method to calculate the correct orbits. Each timestep is subdivided into n subtimesteps, which are integrated
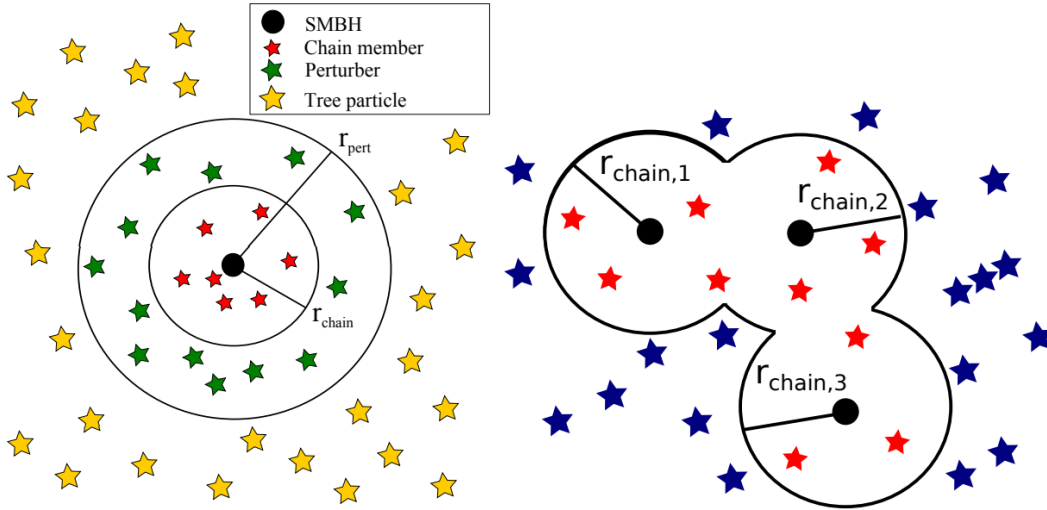
Figure 3.1: Left: Illustration of a chain system with a single black hole (black dot), with the surrounding particles distinguished between chain particles (red stars), perturber particles (green stars) and tree particles (yellow stars). Right: Illustration of a chain system with three black hole particles. The red stars indicate chain particles, while the blue stars indicate perturber particles. Both pictures are taken from Rantala et al. 2017.

numerically. The same calculation is then done increasing n, and the limit for $n \to \infty$ is calculated using a polynomial extrapolation. All of these techniques allow to calculate Newtonian two-body orbits correctly to numerical precision. Post-Newtonian corrections are also included, in the form of additional terms in the relative accelerations between particles. They reach up to the seventh inverse order in c (speed of light), which includes the orbital effect of the emission of gravitational waves. These Post-Newtonian corrections are negligible in most cases, but are important for accurately representing the interaction between two black hole particles. The particles in the simulation are divided into three groups:

- The chain particles: the orbits of these particles are calculated with the regularized integrator described previously.

- The perturber particles: the movements of these particles are calculated like they would be in a normal version of GADGET, but they exert tidal forces on the chain particles, and to satisfy Newton's third law their acceleration receives a correction from neighbouring chain systems.

- The tree particles: these particles are treated like ordinary GADGET particles in every way.

A particle belongs to a chain if it is a black hole particle or if it lies in the vicinity of one, as defined by:

$$|\vec{r} - \vec{r}_{\mathrm{BH}}| < r_{\mathrm{chain}}, \tag{3.13}$$

where $\vec{r}$ is the position of the particle and $\vec{r}_{\mathrm{BH}}$ the position of the nearest black hole. Similarly, the perturber particles are defined by not belonging to a chain but having position:

$$|\vec{r_j} - \vec{r}_{\mathrm{BH}}| < r_{\mathrm{pert},j}, \tag{3.14}$$

where $r_{\mathrm{pert},j}$ in principle depends on the mass of the particle. In our simulations $r_{\mathrm{pert},j} = 2\,r_{\mathrm{chain}}$. All particles that are not in the chain or perturbers, are tree particles. The left panel of Figure 3.1 shows an illustration of this concept. The value of r_{chain} is user-selected, but it should be larger than $2.8 \times r_{\mathrm{soft}}$ to ensure that interactions between black holes and other particles are never softened. However having a too large value for r_{chain} would slow down the code without improving the accuracy significantly, so the optimal choice depends on the number density of particles around the black hole for each simulation. If multiple black hole particles get close enough, their chain subsystems can connect (see the right panel of Figure 3.1 for an illustration). All the particles within a chain are treated internally by KETJU, while GADGET sees the whole chain as a single large particle positioned in the center of mass of the chain.

3.2   Zoom cosmological simulations

In the first two projects of my thesis (Chapters 4 and 5) I analyzed a set of twenty cosmological *zoom* simulations to study the impact of AGN feedback. They were run from a set of ten initial conditions, each simulated once with and once without the AGN feedback model. A zoom simulation is based on a previously run standard cosmological simulation (the 'parent'), but focuses on a single halo. In the zoom most of the cosmological box is represented by low-resolution (high mass) dark matter particles, while the region that eventually collapses into the halo of interest is represented in high resolution and including gas, star formation and feedback. This allows to achieve very high resolutions in a cosmological context, for only a small fraction of the computational cost of running the full box. Here we will describe how the initial conditions for our zoom simulations were generated and how they were run. We will also present the simulations themselves and their properties.

3.2.1   Initial conditions

The initial conditions for the simulations were based on a $(100\,\mathrm{Mpc})^3$ parent dark matter only simulation, run with a WMAP3 cosmology (Spergel et al., 2007): $h = 0.72, \Omega_{\mathrm{b}} = 0.044, \Omega_{\mathrm{dm}} = 0.216, \Omega_{\Lambda} = 0.74, \sigma_8 = 0.77, n_{\mathrm{s}} = 0.95$. Each of the ten selected halos to zoom into have high mass and are relatively isolated, in order to make the simulation less computationally expensive. For each halo, all particles within twice the virial radius in any of the simulation snapshots were identified. Considering all the snapshots ensures that halos which interact with the main one are also represented in high resolution. The region where the traced particles lie in the initial conditions of the parent is the zoom region. The zoom initial conditions were then constructed using GRAFIC2 (Bertschinger,

2001), so that the zoom region is surrounded by four shells with particles of gradually lower resolution. Only the zoom region includes gas particles. Further details on the construction of the zoom initial conditions are presented in Oser et al. (2010) and Oser et al. (2012). The same initial conditions were used in e.g. Naab et al., 2014 , Hirschmann et al., 2012; Hirschmann et al., 2013; Naab et al., 2014 and Hirschmann et al., 2017, but here we simulate at higher resolution. In our case (high-resolution) dark matter particles have a mass of $m_p = 3.62 \cdot 10^6 \, M_\odot \, h^{-1}$ and gas particles initially have mass of $m_p = 7.37 \cdot 10^5 M_\odot \, h^{-1}$.

3.2.2 Simulation details

The simulation code is the same as the one used in Hirschmann et al. (2017), with the models for star formation, stellar feedback and AGN feedback described in Chapter 3.1. It does not include the KETJU integrator. In the simulations without AGN feedback, black hole particles are not present at all.

The simulations are run from $z = 43$ to $z = 0$ with gravitational softening lengths of $0.2 \, \mathrm{kpc}$ for gas, star and black hole particles and $0.45 \, \mathrm{kpc}$ for dark matter particles at the highest resolution level. We saved 95 snapshots throughout the simulations to look at the evolution with time of galactic properties. By $z = 0$ our galaxies have $\sim 10^6$ stellar particles, which ensures accurate stellar dynamics. Their stellar masses range from 0.5 to $5 \, 10^{11} \, M_\odot$. Their physical properties will be discussed further in Chapter 4. Figure 3.2 shows a mock V-band picture of the whole sample. The first two rows show the galaxies simulated without AGN feedback, while the bottom two rows show the same galaxies with AGN feedback. The two cases will be labelled *NoAGN* and *AGN* throughout the thesis. The ID of the galaxy (0175, 0204,...) identifies the halo in the parent simulation from which the zoom initial conditions were constructed. Previous works that used the same initial conditions (Oser et al., 2010; Oser et al., 2012, Hirschmann et al., 2012; Hirschmann et al., 2013, Naab et al., 2014 and Röttgers et al., 2014, Hirschmann et al., 2017) used the same identifiers, so the simulations can be compared. However their simulations used different versions of GADGET and had lower resolution, so the resulting galaxies might have different properties.

3.3 Isolated merger simulations

In the third project of this thesis, described in Chapter 6, we analyze a series of isolated merger simulations. These lack the cosmological context of the zoom simulations, but are extremely useful for understanding specific phenomena, in this case, the dynamical impact of supermassive black holes during galaxy mergers. These simulations do not include gas particles, and thus also do not include star formation and feedback. They however include the KETJU integrator, in order to evaluate accurately the gravitational interactions between supermassive black holes and stars.
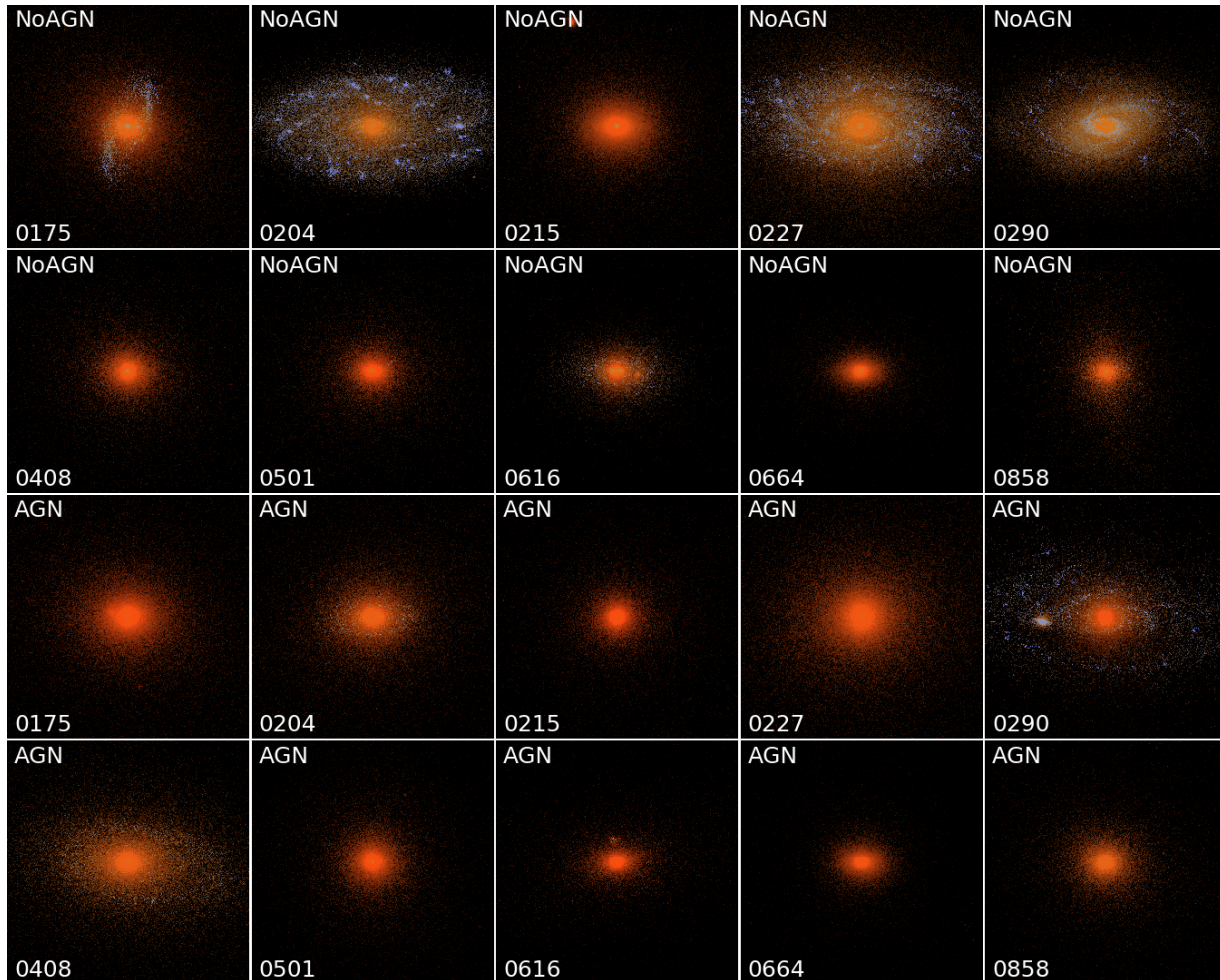
Figure 3.2: Mock stellar luminosity images of our sample of zoom cosmological simulations (Chapters 4 and 5), run without (top two rows) and with (bottom two rows) AGN feedback, at $z = 0$. All galaxies are viewed at an angle of 30 degrees. Stars are colour-coded by V-band weighted age based on Bruzual and Charlot (2003). Many of the galaxies simulated without AGN feedback show the presence of young stellar disks, despite being massive ellipticals.

3.3.1 Initial galaxy models

The initial galaxy models for these simulations are spherically symmetric and made of three components: stars, dark matter, and a central black hole. Both stars and dark matter follow a Dehnen (1993) density profile:

$$\rho(r) = \frac{(3-\gamma)\,M}{4\,\pi\,a^3}\,\frac{1}{(\frac{r}{a})^\gamma\,(1+\frac{r}{a})^{4-\gamma}}. \tag{3.15}$$

This density profile reduces to the Hernquist (1990) for $\gamma = 1$, and to the Jaffe (1983) profile for $\gamma = 2$. In our simulations the stellar component follows the $\gamma = 3/2$ profile, which when projected reproduces the de Vaucouleurs (1948) luminosity profile ($L \propto \exp(-R^{1/4})$), which fits observed massive elliptical galaxies. The dark matter component follows instead the Hernquist profile ($\gamma = 1$), which is a good representation of inferred dark matter profiles and has a finite total mass (unlike the Navarro et al. (1997) profile, which needs to be cut at a certain radius). The cumulative mass distribution for these density profiles is given by:

$$M(r) = 4\,\pi \int_0^r \rho(r)\,r^2 dr = M\left(\frac{r}{r+a}\right)^{3-\gamma}, \tag{3.16}$$

and the (three-dimensional) half-mass radius is given by:

$$r_{1/2} = \frac{a}{2^{1/(3-\gamma)} - 1}. \tag{3.17}$$

The projected half-mass radius (or effective radius) is well approximated by $R_e \simeq 3/4\,r_{1/2}$. In all our models we picked the size parameter a for the dark matter profile so that the dark matter fraction within the stellar $r_{1/2}$ is always $f_{\mathrm{DM}}(r_{1/2}) = 0.25$. The black hole is represented by a point mass at the center of the model.

The generation of the galaxy models themselves was done through Eddington's formula (Binney and Tremaine, 2008). The velocities of particles are assigned according to a distribution function $f(\varepsilon)$:

$$f(\varepsilon) = \frac{1}{\sqrt{8}\pi^2} \int_{\phi_T=0}^{\phi_T=\varepsilon} \frac{d^2\rho_i}{d\phi_T^2}\,\frac{d\phi_T}{\sqrt{\varepsilon - \psi_T}}, \tag{3.18}$$

where $\varepsilon = -v^2/2 - \phi_T$, ρ_i is the density of component i (stars or dark matter) and ϕ_T is the total potential of the system (stars plus dark matter plus black hole). The potential for a Dehnen density profile is given by:

$$\phi(r) = \frac{GM}{a} \cdot \begin{cases} -\frac{1}{2-\gamma}\left(1 - (\frac{r}{r+a})^{2-\gamma}\right) & \text{if } \gamma \neq 2 \\ \ln\frac{r}{r+a} & \text{if } \gamma = 2 \end{cases}. \tag{3.19}$$

Using the distribution function in Eq. 3.18 ensures that the system will be gravitationally stable, and makes the velocity distribution isotropic.

The physical parameters of the model are $M_\star$ (mass of the stellar component), M_{DM} (mass

Progenitor	$M_\star$ $[10^{10}M_\odot]$	M_{DM} $[10^{13}M_\odot]$	M_{BH} $[10^9 M_\odot]$	R_e [kpc]	f_{DM} $(r_{1/2})$	$N_\star$ $[\times 10^6]$	N_{DM} $[\times 10^6]$
IC-1	8.30	1.50	1.70	3.50	0.25	0.83	2.00
IC-2	10.34	1.88	2.13	4.16	0.25	1.04	2.50
IC-3	13.83	2.50	2.93	4.95	0.25	1.38	3.33
IC-4	20.75	3.75	4.25	5.90	0.25	2.08	5.00
IC-5-bh6	41.50	7.50	8.50	7.00	0.25	4.15	10.00
IC-5-bh5			6.80				
IC-5-bh4			5.10				
IC-5-bh3	⋮	⋮	3.40	⋮	⋮	⋮	⋮
IC-5-bh2			1.70				
IC-5-bh1			0.85				
IC-5-nobh			0.				

Table 3.1: Properties of the initial condition models for our isolated simulations (Chapter 6). From left to right, stellar mass, dark matter halo mass, black hole mass, stellar effective radius, dark matter fraction within (three-dimensional) half-mass radius, number of stellar particles, number of dark matter particles.

of the dark matter halo), M_{BH} (mass of the black hole), R_e (effective radius of the stellar component). The number of particles per galaxy model was chosen so that the stellar particles have mass $m_\star = 1.0 \times 10^5 M_\odot$ and the dark matter particles mass $m_{\mathrm{DM}} = 7.5 \times 10^6 M_\odot$. Table 3.1 shows a summary of the properties of the 11 different models we used.

3.3.2   Simulated sample

Our sample consists of 12 merger remnants, that can be divided in two groups: equal-mass mergers (mergers of identical galaxies, varying their black hole masses) and minor mergers (mergers of galaxies with different masses).Table 3.2 summarizes the whole simulation sample. In each merger simulation the two galaxy models start at a distance of 30 kpc from each other and move on nearly parabolic orbits, with pericenter distance $r_p \sim 0.5 \times R_e$ of the larger galaxy. The simulations are run for $t = 2\mathrm{Gyr}$, which is usually enough for the two black holes to merge. A special case is M5x5, which is the remnant of five successive minor mergers. In this case the satellite galaxies come each time from random directions, and the new satellites are introduced only once the previous merger finished. These simulations were also analyzed in Rantala et al., 2018a and Rantala et al., 2018b, and further details can be found there.

Label	Merger description	Mass ratio	$M_\star$ $[10^{10}M_\odot]$	$M_{\rm DM}$ $[10^{13}M_\odot]$	$M_{\rm BH}$ $[10^9 M_\odot]$
Equal-mass mergers					
M1-bh6	IC-5-bh6 + IC-5-bh6	1:1	83.00	15.0	17.00
M1-bh5	IC-5-bh5 + IC-5-bh5				13.60
M1-bh4	IC-5-bh4 + IC-5-bh4				10.20
M1-bh3	IC-5-bh3 + IC-5-bh3				6.80
M1-bh2	IC-5-bh2 + IC-5-bh2	$\vdots$	$\vdots$	$\vdots$	3.40
M1-bh1	IC-5-bh1 + IC-5-bh1				1.70
M1-nobh	IC-5-nobh + IC-5-nobh				0.00
Unequal-mass mergers					
M5	IC-5-bh6 + IC-1	5:1	49.80	9.0	10.20
M4	IC-5-bh6 + IC-2	4:1	51.88	9.38	10.20
M3	IC-5-bh6 + IC-3	3:1	55.33	10.0	10.20
M2	IC-5-bh6 + IC-4	2:1	62.25	11.25	10.20
Multiple merger generations					
M5x5	IC-5-bh6 + 5 × IC-1	5:1-9:1	83.00	15.0	17.00

Table 3.2: Physical properties and merger configuration of our set of isolated simulations (Chapter 6). From left to right: label of the simulation, merger configuration, merger ratio, final stellar mass, final halo mass, final black hole mass.

Chapter 4

The impact of AGN feedback on kinematics

The connection between active galactic nuclei (AGN) and their host galaxies has been subject of research for more than two decades. Soon after the discovery of super-massive black holes (SMBH) in the centers of early-type galaxies, correlations have been found between their mass and galactic properties such as galactic bulge mass and velocity dispersion (Dressler, 1989; Kormendy, 1993; Gebhardt et al., 2000). This connection has been in the focus of theoretical work with the conclusion that the energy feedback from accreting black holes could be necessary to reproduce these scaling relations as well as the correct masses and abundances of early-type galaxies in cosmological simulations (see e.g. Croton et al., 2006; Schaye et al., 2015; Vogelsberger et al., 2014b and reviews by Kormendy and Ho (2013), Somerville and Davé (2015) and Naab and Ostriker (2017)). However, the impact of AGN might go beyond affecting global properties. The cosmological simulations of Choi et al. (2015) and Choi et al. (2017) showed that in low-redshift galaxies the fraction of stars that form in-situ is much lower when including AGN feedback. This has strong repercussions on the morphological and kinematic properties of these galaxies: in-situ formed stars tend to form orderly-rotating disks, while stars which are accreted from other galaxies form round dispersion-supported systems. Because of this connection, many studies attributed the difference in properties of present-day galaxies to stellar origins. The more massive early-type galaxies, whose stellar component has been for a significant part accreted, tend to have smaller angular momentum (Emsellem et al., 2011) and more complex kinematics (Krajnović et al., 2011), while intermediate and low-mass galaxies, which have formed most of their stars in-situ, are simple fast-rotating systems (see Cappellari (2016) for a review). Naab et al. (2014) and Röttgers et al. (2014) linked the present-day kinematics of simulated galaxies to the type of galaxy mergers they experienced during their formation: minor or major, and with or without gas. This picture would however be incomplete without including AGN feedback. Dubois et al. (2016) and Penoyre et al. (2017) showed that only with AGN feedback they were able to obtain realistic abundances of slow-rotating systems in cosmological simulations.

In this Chapter we analyze a small sample of high-resolution cosmological zoom simu-

lations for a more in-depth look at the impact of AGN feedback on the kinematic and stellar-population properties of galaxies, but also extending the analysis to higher-order kinematics and orbital structure. The simulations consist of ten different cosmological initial conditions, each run once with AGN feedback and once without. Throughout the thesis the two cases will be labelled as *AGN* and *NoAGN*. The details on the simulations and how they were constructed were presented in Chapter 3.2, and Figure 3.2 gives us a visualisation of the sample. Comparing the *AGN* and *NoAGN* galaxies in Figure 3.2 we can already notice that the *NoAGN* galaxies are bluer (younger) and more massive. Here however we want to compare our simulated galaxies by mocking the images produced by integral field unit (IFU) spectrographs, so that we can also compare our results with observations. Our method for generating these mock IFU plots has been presented in Chapter 2.1. The results presented in this Chapter have been published (on arXiv at the time of writing this) in Frigo et al., 2018. Following is the structure of this Chapter. In Chapter 4.1 we look at the effect of AGN feedback on one exemplary simulated galaxy, through our mock IFU maps. In Chapter 4.2 we analyze the full simulation sample, to get an idea of the general impact of AGN feedback. In Chapter 4.3 we discuss and summarize our conclusions for this work.

4.1   A typical galaxy simulated with and without AGN feedback

Our study involves a small sample of 20 massive galaxies. As a test case, we first discuss the formation history, global galaxy properties, stellar kinematics, stellar age and metallicity, morphology and redshift evolution for one prototypical galaxy. Simulating this initial condition with and without AGN feedback allows us to investigate the impact of AGN feedback on the final properties of the galaxy.

4.1.1   Formation history and global properties

Galaxy 0227 is an early-type galaxy, with an effective radius of 4.0 kpc and a stellar mass of $2 \cdot 10^{11} \, M_\odot$ in the *AGN* case and $5 \cdot 10^{11} \, M_\odot$ in the *NoAGN* case. Its formation history is characterized by a major merger at redshift $z \sim 0.25$, with mass ratio of $1 : 1.7$ and $1 : 1.2$ in the *NoAGN* and *AGN* cases. The presence of AGN has a strong influence on the evolution after the merger. Figure 3.2 shows a mock V-band image of this galaxy with and without AGN feedback. In the absence of AGN feedback (left panel) the galaxy is still forming new stars in an extended disk. Instead, in the case with AGN feedback (right panel) the system is spheroidal with a very old stellar population.

Figure 4.1 shows the age distribution of stars in galaxy 0227 simulated with and without AGN feedback. The oldest stars (age > 10 Gyr) have very similar age distributions, with the bulk forming around $z \sim 2$. Towards lower redshifts, star formation gets quenched in the *AGN* case; a behaviour found in all our simulations. While in the *AGN* case not
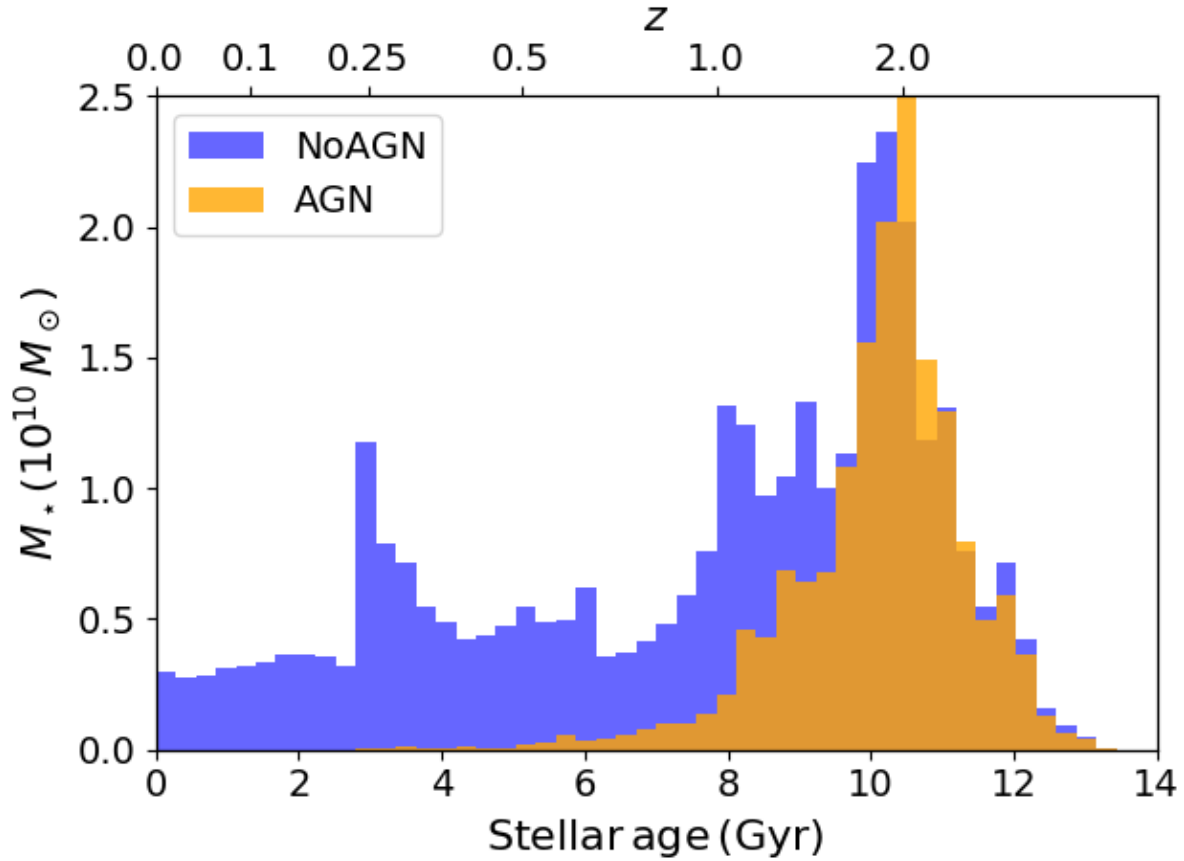
Figure 4.1: Age distribution of star particles in the case study galaxy (0227) for the run with AGN feedback (orange) and the one without (blue). The top x-axis shows the corresponding redshift at which the stars have formed. Star formation proceeded at a similar rate up $z = 2$. Then it is rapidly terminated in the presence of AGN feedback. Without AGN feedback star formation continues all the way to $z = 0$.
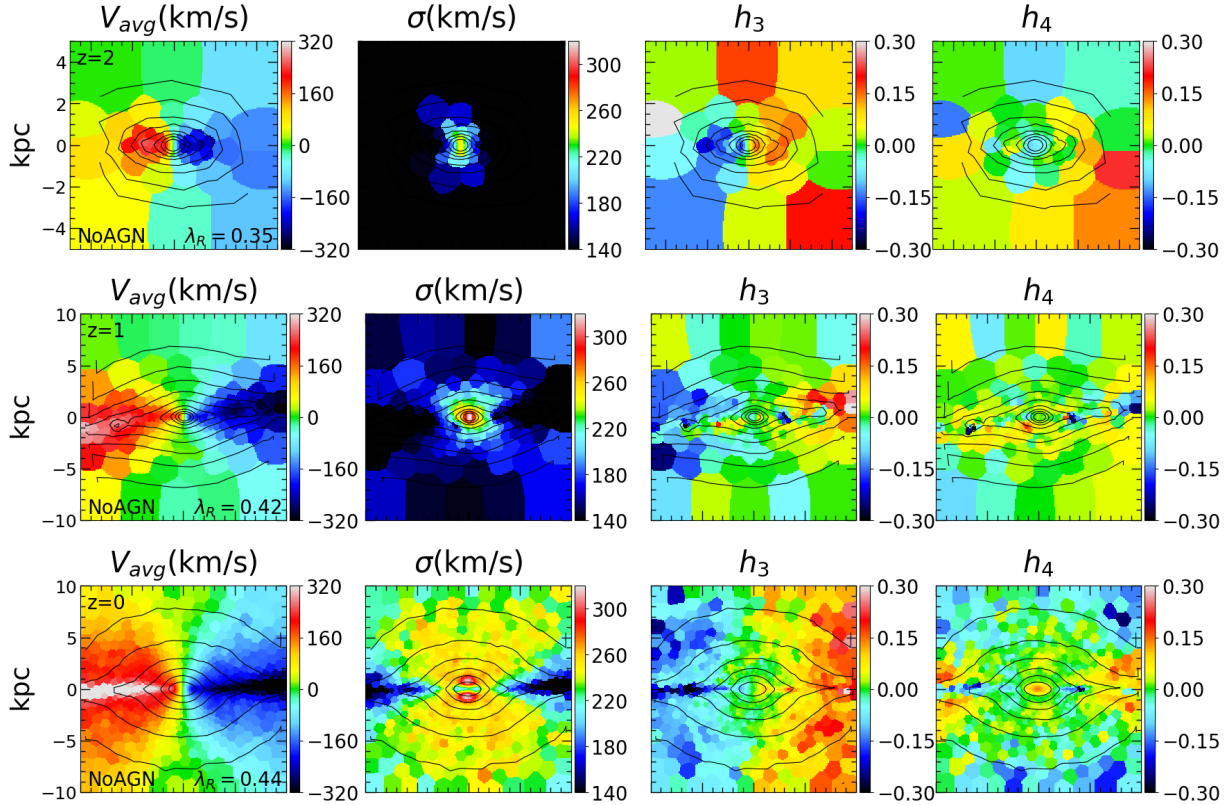
Figure 4.2: Edge-on two-dimensional line-of-sight stellar kinematics (V_{avg}-σ-h_3-h_4 from left to right) of galaxy 0227 simulated without AGN feedback at $z = 2$, $z = 1$, and $z = 0$ (from top to bottom). The maps show typical features of systems with a disk-like component: high LOS velocity in the mid-plane, dumb-bell shaped velocity dispersion with a suppression in the mid plane disk region, anti-correlation of line-of-sight velocity and h_3 negative h_4 along the disk. These features become strongest at $z = 0$, when the disk is most prominent and can clearly be seen in the surface density contours (black lines).
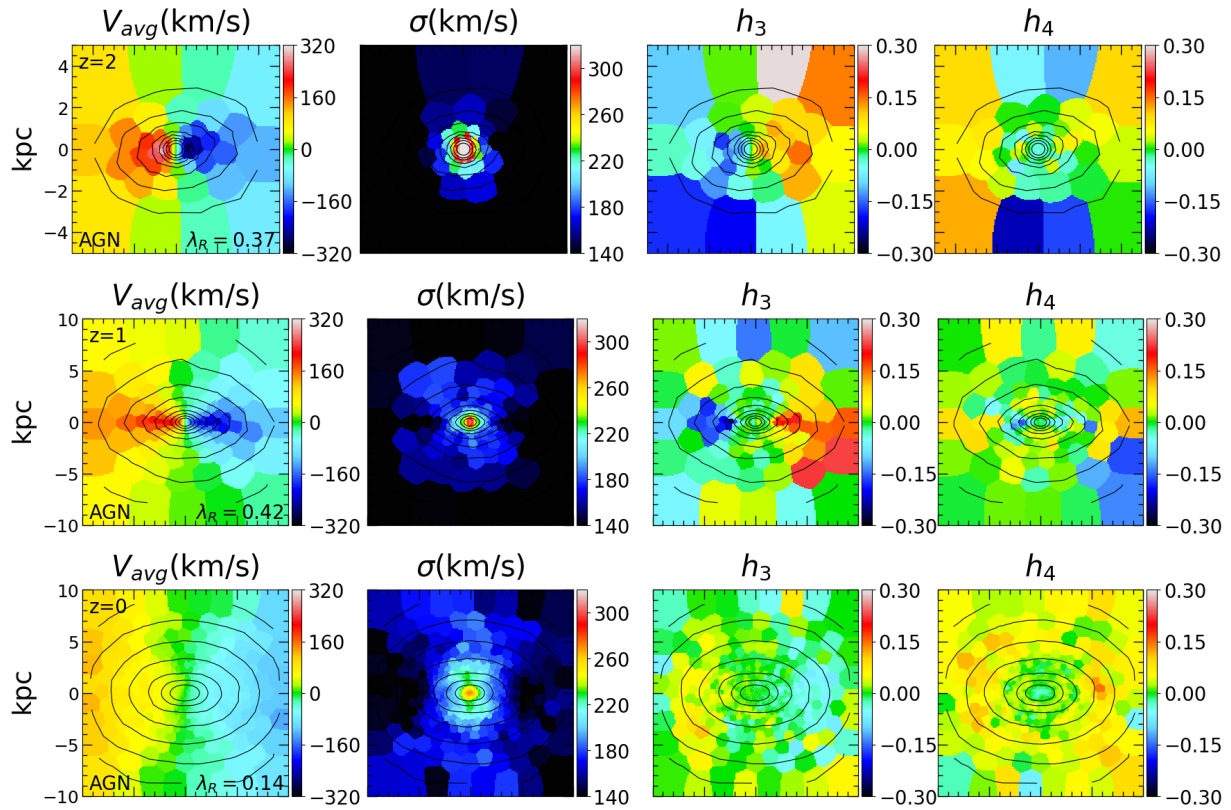
Figure 4.3: Same as Fig. 4.2 for galaxy 0227 simulated including AGN feedback. The kinematics is qualitatively similar to the case without AGN at $z = 2$ and $z = 1$. By $z = 0$ however the strong rotational signatures are gone, and the galaxy looks more like a typical slow-rotator without kinematic disk signatures: low average LOS velocity, high velocity dispersion, no h_3 anti-correlation signal, positive h_4.

many stars form after $z \sim 1$, in the *NoAGN* case star formation continues throughout the simulation, including a starburst at $z \sim 0.25$ during the major merger.

4.1.2   LOS kinematics

In order to identify features in the stellar kinematics originating from the impact of AGN feedback, we construct two-dimensional maps visualising kinematic properties, as detailed in Sec. 2.1.4. The galaxy is oriented so that the intermediate axis is aligned with the line-of-sight. This is done using the eigenvectors of the reduced inertia tensor (Bailin and Steinmetz, 2005):

$$\tilde{I}_{i,j} = \sum_{\text{Particles } k} m_k \frac{r_{k,i}\, r_{k,j}}{r_k^2}, \tag{4.1}$$

where m_k and $\vec{r}_k$ are the masses and positions of the particles. The eigenvalues of this tensor are proportional to the length of the axes of the galaxy, and the eigenvectors follow their orientation.

We first show the stellar line-of-sight velocity, velocity dispersion, and the higher order moments h_3 and h_4 in Figs. 4.2 and 4.3 for galaxy 0227 without and with AGN feedback at $z = 2$, $z = 1$, and $z = 0$. Initially (at $z = 2$ and $z = 1$) there are only moderate differences between the *AGN* and *NoAGN* simulations. The *AGN* and *NoAGN* galaxies (in brackets) have similar stellar masses of $M_* = 0.59 * 10^{11}\, M_\odot$ ($M_* = 0.54 * 10^{11}\, M_\odot$) at $z = 2$, while at $z = 1$ they are $M_* \sim 1.16 * 10^{11}\, M_\odot$ ($M_* \sim 1.97 * 10^{11}\, M_\odot$). The effective radii are $\sim 0.18\,\text{kpc}$ ($\sim 0.35\,\text{kpc}$) at $z = 2$ and 0.95kpc (1.53kpc) at $z = 1$. Down to $z = 1$, the galaxies are supported by rotation. The average stellar line-of-sight velocities reach values of $\sim 200\,\text{km/s}$, and the velocity dispersion values around $300\,\text{km/s}$. The velocity increases only slightly from $z = 2$ to $z = 1$, but the rotating component becomes more extended for both cases. The h_3 parameter is anti-correlated with the LOS velocity - a typical signature for axisymmetric rotating systems (Krajnović et al., 2011; Naab et al., 2014). The origin of this effect is explained in detail in Chapter 2.1.3, as well as in Naab and Burkert (2001), Naab et al. (2006), Röttgers et al. (2014), and Naab et al. (2014) in the context of idealized models, merger simulations and cosmological simulations. At redshift $z = 0$, the situation is markedly different. In the *NoAGN* case the rotation signatures are significantly enhanced. The LOS velocities reach up to $320\,\text{km/s}$ in an extended disk. The velocity dispersion map shows a dumbbell feature with reduced velocity dispersion in the mid plane, which is a signature of an edge-on rotation-supported disk embedded in a dispersion-supported spheroidal component. This can be seen by the isophotes (see Sec. 4.1.5). The LOS velocity distribution is asymmetric with anti-correlated h_3 values. The h_4 map shows characteristic features of disk rotation (bottom right panel of Fig. 4.2). In the central kpc region, h_4 is positive, indicating a more peaked Gaussian LOS velocity distribution with more extended wings towards lower and higher than the systemic velocity as individual pixels cover significant fractions of the stars' orbits. At larger radii (in the mid plane), h_4 becomes negative indicating coherent rotation with very weak tails towards high and low velocities. As h_4 is known to roughly correlate with the velocity anisotropy

(Gerhard, 1993; Thomas et al., 2007), a negative h_4 indicates that tangentially biased orbits are dominating, which is to be expected in a rotating disk. Kinematic maps of this kind are regularly found in observational surveys like $ATLAS^{3D}$ (Cappellari et al., 2011), CALIFA (Sánchez et al., 2012), or SAMI (Croom et al., 2012). They are, however, more common for less massive galaxies. It is very unlikely to observe an elliptical galaxy of this high mass with such a prominent fast-rotating disk. The kinematic galaxy properties are very different in the AGN case (Fig. 4.3). By $z = 0$, there are no signatures of a prominent rotating stellar disk, as the AGN feedback prevents further gas accretion and in-situ disk formation (see e.g. Brennan et al., 2018). The galaxy is slowly rotating at $\sim 80\,\mathrm{km/s}$ and dispersion dominated, with only weak features in the higher-order moments. Interestingly, h_3 is positively correlated with V_{avg} in the central part of the galaxy. This is rare for observed galaxies, but relatively common in the simulated remnants of gas poor mergers (see Naab and Burkert, 2001; Naab et al., 2006; Röttgers et al., 2014). This positive correlation must originate from a particular orbital distribution, which will be analyzed in Chapter 4.1.7. Also a core with negative h_4 is still visible. Values for h_4 are positive in most of the map indicating radially-biased orbits. All of the above features are typical properties of massive early-type galaxies.

4.1.3   Age and metallicity distribution at z=0

Figure 4.4 shows a comparison of the projected stellar age (top panels) and metallicity (bottom panels) distributions for the $NoAGN$ (left column) and AGN (right column) simulation at $z = 0$. At low redshifts the properties of the systems differ the most. In the $NoAGN$ case there is a distinct young $< 4\,\mathrm{Gyr}$ stellar disk embedded in an older $7 - 9\,\mathrm{Gyr}$ stellar bulge. A moderate positive age gradient towards younger ages away from the center is visible. The disk appears as a flattened metal enriched region in the mid plane, pretty much following the isophotes. These features indicate ongoing disk-like star formation and metal enrichment since $z = 1$. This is also consistent with the stellar age distribution in Fig. 4.1. In the AGN case (right panels of Fig. 4.4) the stellar population is older ($\sim 10\,\mathrm{Gyr}$, see also Fig. 4.1), less metal enriched - due to less ongoing star formation - with a shallower metallicity gradient. There is a mild positive age gradient with younger ages in the center caused by residual nuclear star formation. A more in-depth look at metallicity gradients can be found in Hirschmann et al. 2015; Rodriguez-Gomez et al. 2016.

4.1.4   Higher order kinematics and metallicity

The spatial dependence of kinematics and stellar population properties are not independent from each other. Figure 4.5 shows the kinematic maps from Figures 4.2 and 4.3 in a different format: the x and y axes indicate the values of V_{avg}/σ and h_3 respectively for each spaxel, and the size of the markers indicate their (projected) distance from the center. The markers are also color-coded according to the average metallicity of those spaxels (see Figure 4.4). The striking feature is that different parts of the galaxies seem to have different trends in
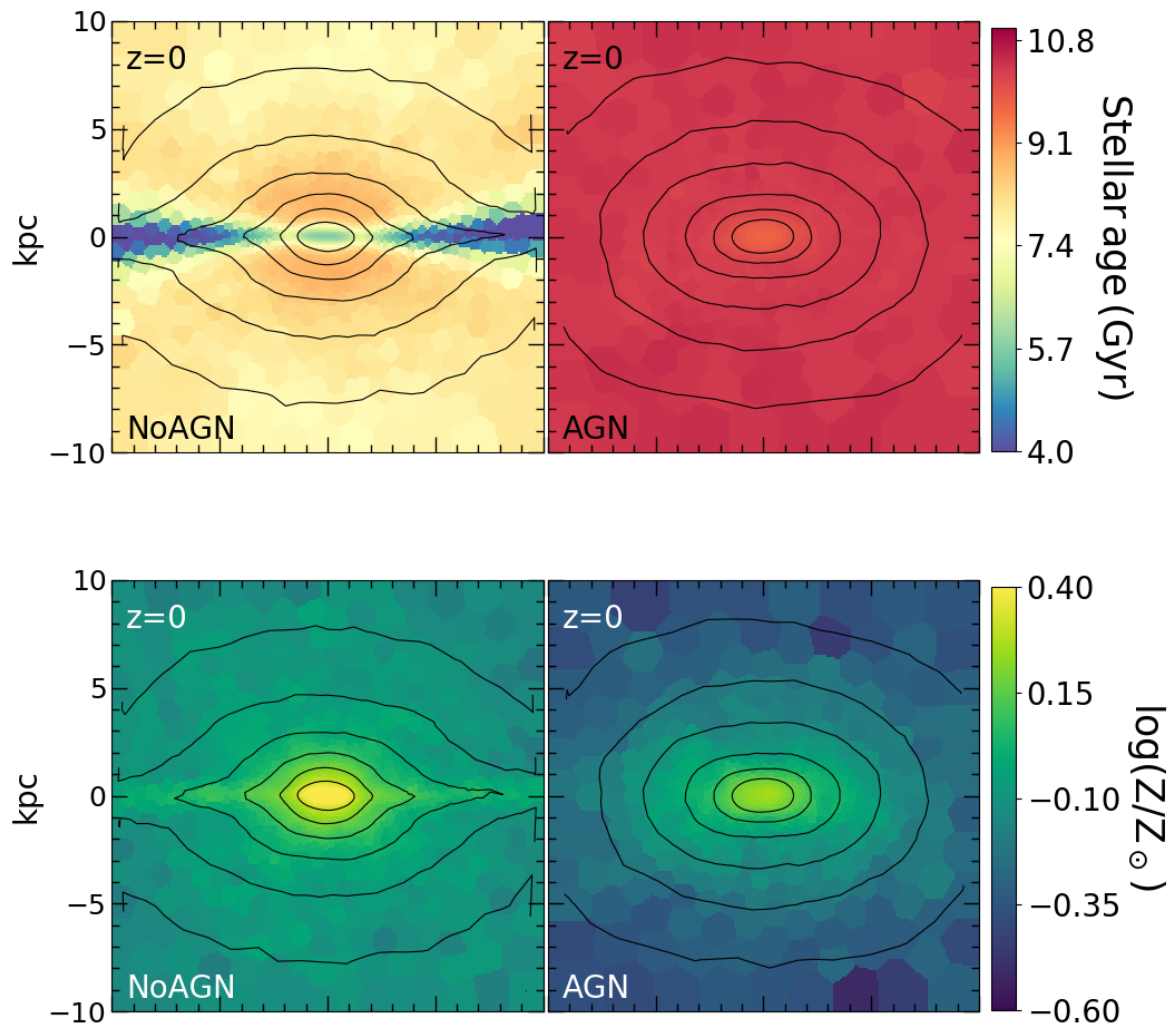
Figure 4.4: Voronoi binned maps of the (mass-weighted) average stellar age (top) and metallicity (bottom) for our case-study galaxy (0227), in the *NoAGN* (left) and *AGN* (right) AGN cases, at $z = 0$. Without AGN feedback the higher star-formation rate at low redshift produces an overall much younger system, especially in the midplane, where a young stellar disk forms. Higher star-formation rate also result in high metallicities. With AGN feedback (right panels) the galaxy is instead very old and the metallicities compare well with observed early-type galaxies.
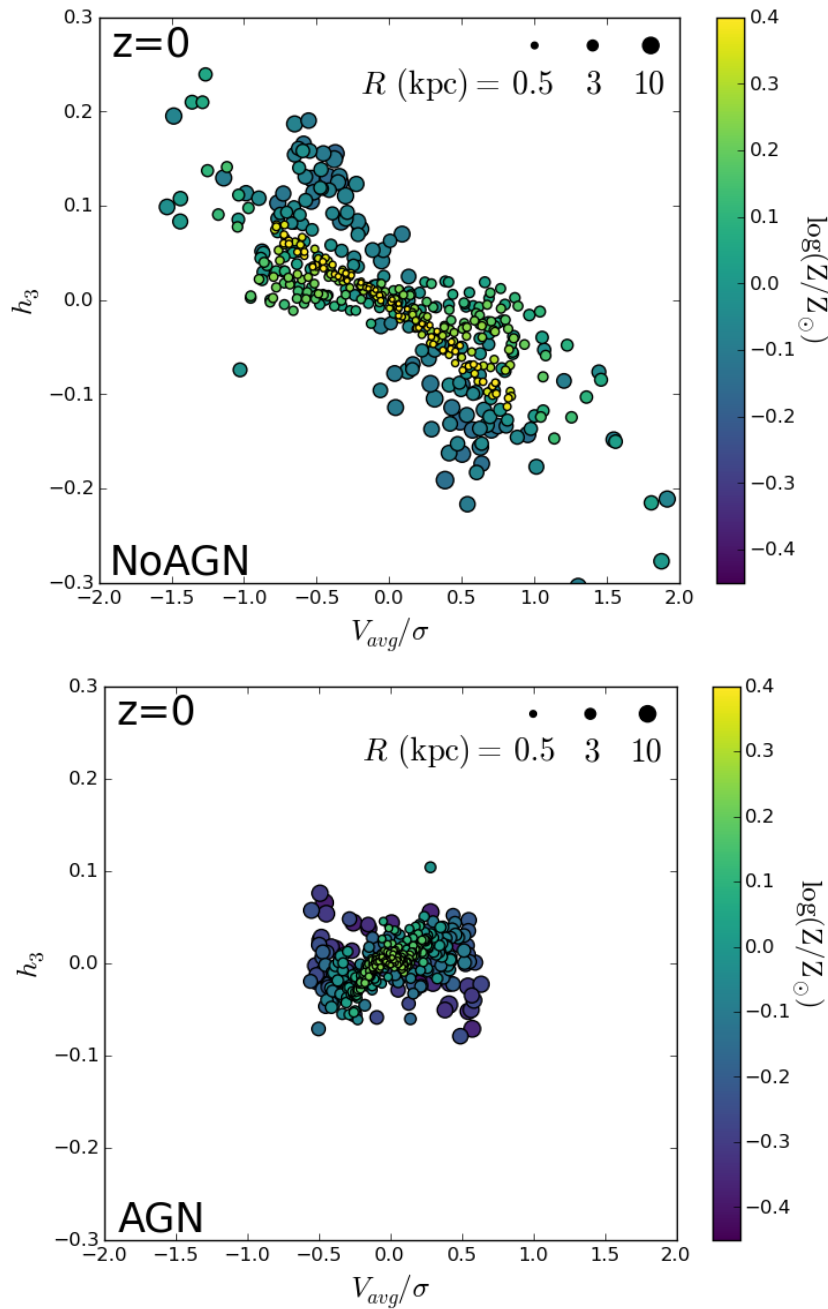
Figure 4.5: h_3 as a function of V_{avg}/σ for galaxy 0227 without AGN feedback (above) and with it (below), seen edge-on. Each marker indicates a spaxel in the colormap, and its size depends on the projected distance of that spaxel from the center. The spaxels are color-coded according to metallicity. In the *AGN* case there is a weak correlation between h_3 and V_{avg}/σ in the inner spaxels, which turns in a weak anticorrelation further out. In the *NoAGN* case there is always anti-correlation, but the slope is different in different parts of the galaxy. In both cases metallicity can be used to separate these different regions.

the h_3-V_{avg}/σ plane, as well as different metallicities. In the AGN case the central spaxels have a weak positive h_3-V_{avg}/σ correlation.

4.1.5 Redshift evolution of kinematic and photometric properties

Here we look at the evolution of three global parameters, λ_R, ξ_3 and a_4/a, through the whole formation history of our case-study simulation.

Angular momentum - λ_R

We first use λ_R (Eq. 2.4) to quantify the redshift evolution of angular momentum in the AGN and $NoAGN$ cases. Figure 4.6 shows the redshift evolution of λ_R from $z = 2$ to $z = 0$. After a tumultuous phase at high redshift caused by mergers, at $z = 1$ λ_R settles at around 0.3-0.4 in both cases. At $z = 0.25$ the angular momentum drops because of the major merger described in Chapter 4.1.1; the vertical dashed line marks the beginning of this merger. The subsequent evolution diverges for the two cases. In the $NoAGN$ simulation the system is more gas rich, and thus loses less angular momentum and even regains it after the merger. This is a typical feature of gas rich mergers and follow-up gas accretion (see review by Naab and Ostriker (2017)). In the AGN case the system is already gas poor, without significant star formation before the merger (see Fig. 4.1). The merger then reduces the angular momentum significantly. Qualitatively this process for gas poor mergers is discussed in detail in Naab et al. (2014). By $z = 0$ the two systems have very different rotation properties with a λ_R value typical of fast rotators in the $NoAGN$ case and a slow rotator value in the AGN case. This impact of AGN feedback on the rotation properties of massive galaxies has already been reported by Dubois et al. (2013) and Martizzi et al. (2014) and Dubois et al. (2016) for cosmological RAMSES adaptive mesh refinement simulations with different AGN feedback models. We therefore assume this to be a generic feature of AGN feedback.

Shape of the LOS velocity distribution - ξ_3

The major merger also affects the higher-order kinematic features. We quantify them using the parameter ξ_3 defined in Eq. 2.6 and plot it as a function of redshift, as shown in Figure 4.7. From $z = 1$ to $z = 0.25$ the two simulations show again the same behaviour, with the same degree of anti-correlation between h_3 and $V_{\mathrm{avg}} / \sigma$: $\xi_3 \sim -7.5$ in both cases. As discussed in Chapter 2.1.3, this value is typical for a system dominated by tangential orbits, but higher than the one expected from a purely rotational system (-10). This indicates that a small amount of other orbit types contributes to skew the LOS velocity distribution. The major merger at $z = 0.25$ again makes the two cases diverge. In the $NoAGN$ case the overall ξ_3 value stays the same. In the AGN case instead ξ_3 drops to 0 and the orbital structure of the system is more dispersion-supported - the correlation
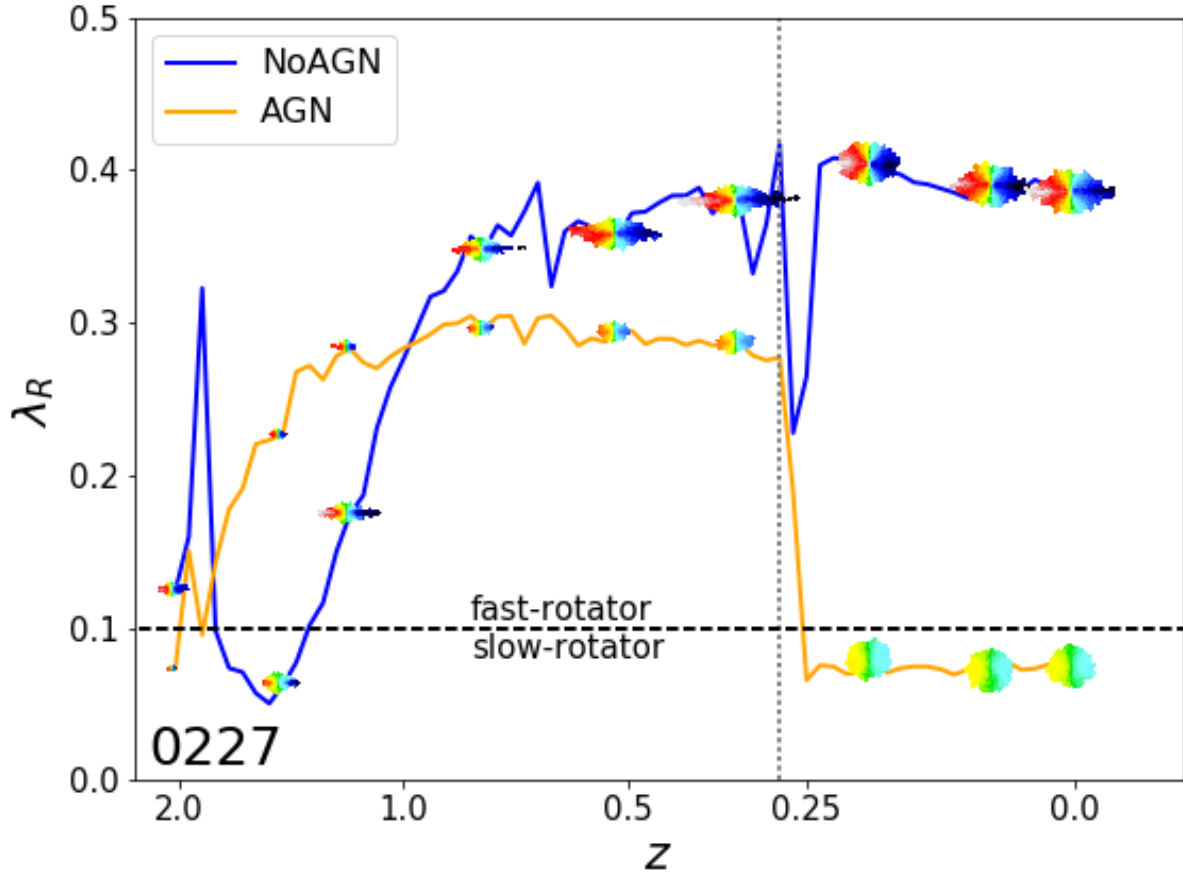
Figure 4.6: Evolution of λ_R for galaxy 0227, in the *NoAGN* and *AGN* cases. The values are indicated by inserted velocity maps out to the effective radius (isophote) of the galaxies. A major merger at $z \sim 0.25$ (vertical dashed line) strongly reduces the angular momentum of both systems. The *NoAGN* galaxy is less affected and can quickly regain angular momentum due to gas accretion and star formation. The *AGN* galaxy is instead unable to form new stars and remains a slow rotator.

between h_3 and V_{avg}/σ becomes weaker. The sign of ξ_3 oscillates a bit, but then settles to a weakly positive value, meaning that h_3 has the same sign as V_{avg} as already pointed out.

Isophotal shape - a_4/a

We investigate the evolution of the isophotal shape parameter a_4/a, which quantifies the deviation of isophotes if galaxies from ellipses. A positive a_4/a means that the isophotes are disky (excess of light in the vertices and covertices of the best-fitting ellipse), while a negative a_4/a means that the isophotes are boxy (lack of light in vertices and covertices; Lauer, 1985, Bender and Moellenhoff, 1987. To compute a_4/a in our simulations, we first calculate the real isophotes as lines of constant stellar surface mass density, and we fit them with ellipses to calculate the ellipticity ϵ. For each galaxy we use 10 isophotes between $0.25 R_{\mathrm{e}}$ and R_{e} and average their values to obtain ϵ . We then apply a Fourier transform to the deviation of the isophotes from the corresponding elliptical fits. The first, second and third order Fourier coefficients are negligible if the ellipse is centred correctly and has the correct ellipticity and orientation angle. The fourth order coefficient a_4, normalised to the zeroth coefficient a, represents the deviation of the isophote from a pure ellipse. The final a_4/a value for each galaxy is then given by the average over the ten isophotes, as is the case for the ellipticity. An example of these isophotes can be seen in the black lines of Figs. 4.2 and 4.3.

In Fig. 4.8 we show the evolution of a_4/a since $z = 2$ by computing it for every snapshot (oriented edge-on). Unlike in the previous cases, the *AGN* and *NoAGN* cases are already different at $z = 1$. The *NoAGN* case has systematically higher values of a_4/a - more disky isophotes. This difference would however not be as pronounced if the galaxy was not seen from an edge-on perspective. The value scatters due to minor mergers but drops to negative values after the major merger at $z = 0.25$. This is the common feature of major mergers destroying previously existing disk structures (see Naab et al., 1999; Naab and Burkert, 2003). Subsequently a new stellar disk forms and the a_4/a value becomes strongly positive again. In the *AGN* case the galaxy already lost its diskyness at high redshift, because of the suppressed inflow of high-angular-momentum star-forming gas, and it keeps its elliptical or mildly boxy isophotes to $z = 0$. The effect of mergers and AGN feedback on the isophotal shape points in the same direction as the effect on λ_R and ξ_3.

4.1.6 Kinematics of the accreted and in-situ-formed stellar components

Our kinematic maps can be generated for different stellar components of the galaxy, to shed light on their respective kinematic structure. One might use the stellar age to distinguish different components; we show this example in the appendix of Frigo et al., 2018. Perhaps even more interesting though, is to separate stellar particles according to their origin: either accreted from another galaxy or formed in-situ in the main progenitor following the accretion of gas. Due to their intrinsically different origin, we can expect these two
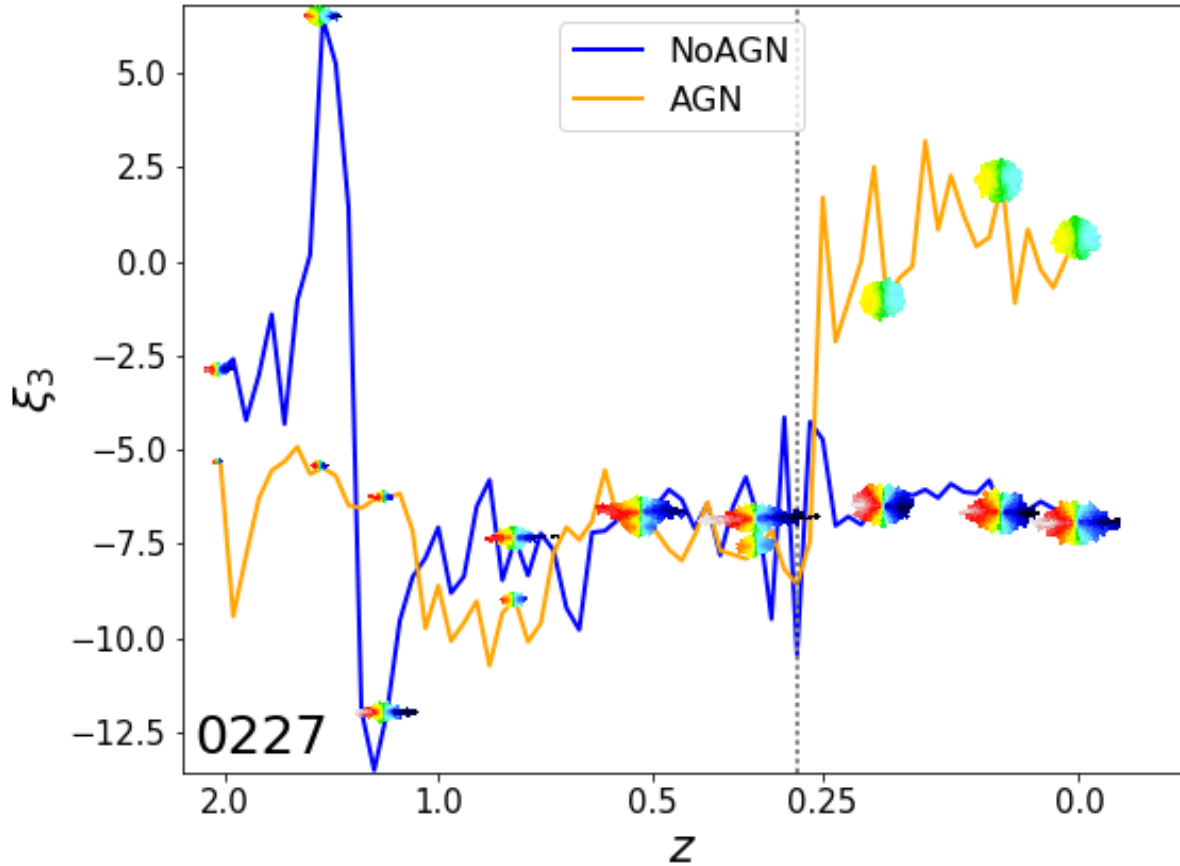
Figure 4.7: Evolution of ξ_3 for galaxy 0227, in the *NoAGN* and *AGN* cases. The values are indicated by small velocity maps out to the effective radius (isophote) of the galaxies. Up to $z = 0.25$ the value of ξ_3 is constant for both simulations and has a value as expected for a rotating system. However, after a major merger at $z \sim 0.25$ (vertical dashed line), the value for the *AGN* galaxy shifts towards zero and mildly positive values. This indicates that the galaxy lost its rotational support.
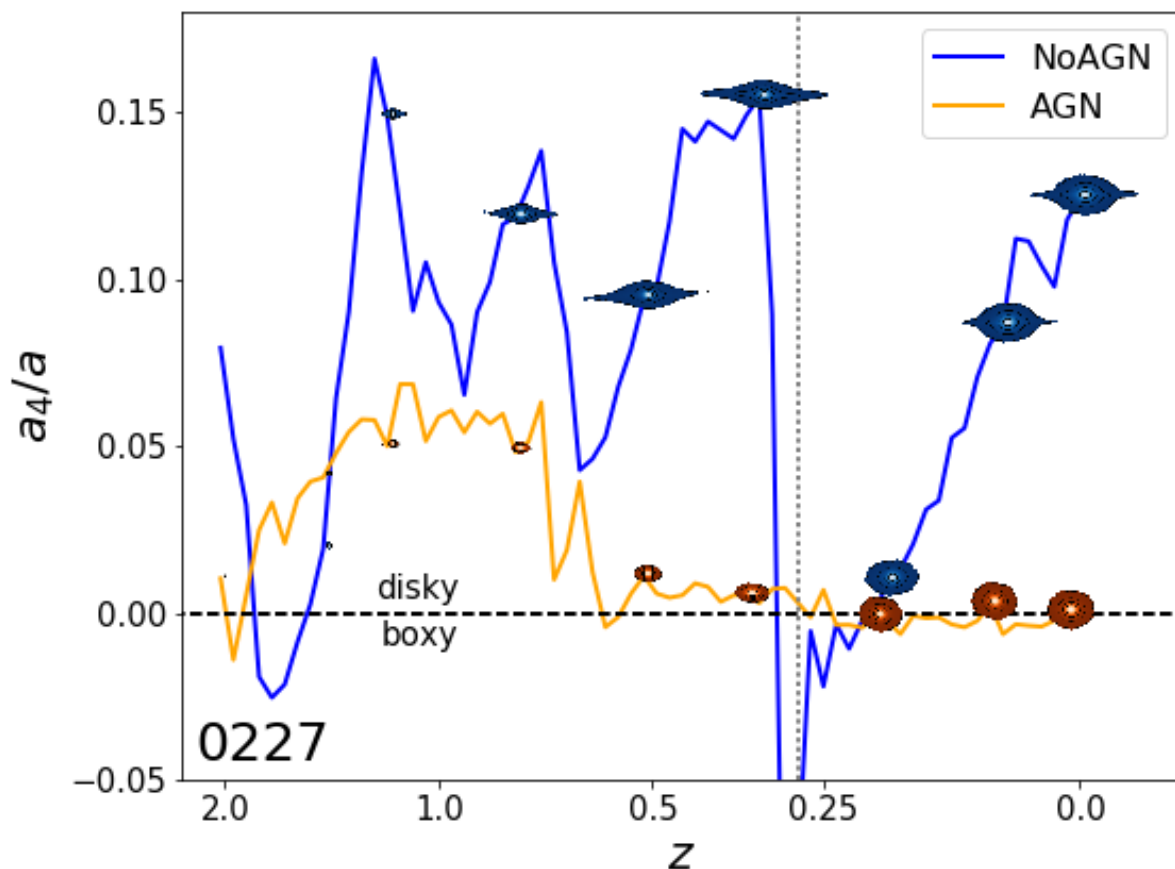
Figure 4.8: Evolution of the isophotal shape of galaxy 0227, in the *AGN* and *NoAGN* case, quantified by a_4/a. The markers are surface brightness maps cut along the effective isophote. The red line represents perfectly elliptical isophotes. 'Boxy' galaxies have negative, 'disky' galaxies have positive a_4/a values. Without AGN feedback the formation of a prominent disk results in disky isophotes at all times, despite the major merger at $z \sim 0.25$ (vertical dashed line). The *AGN* galaxy instead loses its diskyness after the merger because further star formation is suppressed by the AGN.
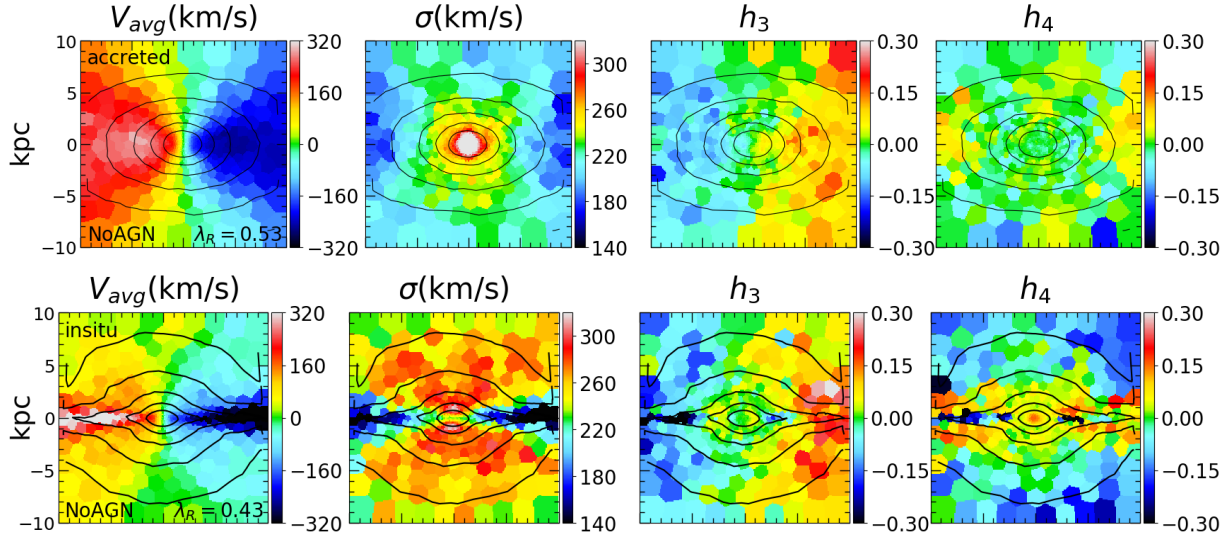
Figure 4.9: Stellar kinematics of galaxy 0227 (NoAGN) separated into its accreted component (above) and its in-situ formed one (below). The overall in-situ fraction is 50% . The two components have strikingly different kinematics. The accreted component is mainly pressure-supported, but also rotates fast. The in-situ component shows two distinct features: a fast-rotating disk in the midplane with low velocity dispersion, and a slow-rotating bulge with very high velocity dispersion. The disk feature formed after a recent major merger, while the surrounding bulge is older, and its originally rotational orbits have been scrambled by the merger.
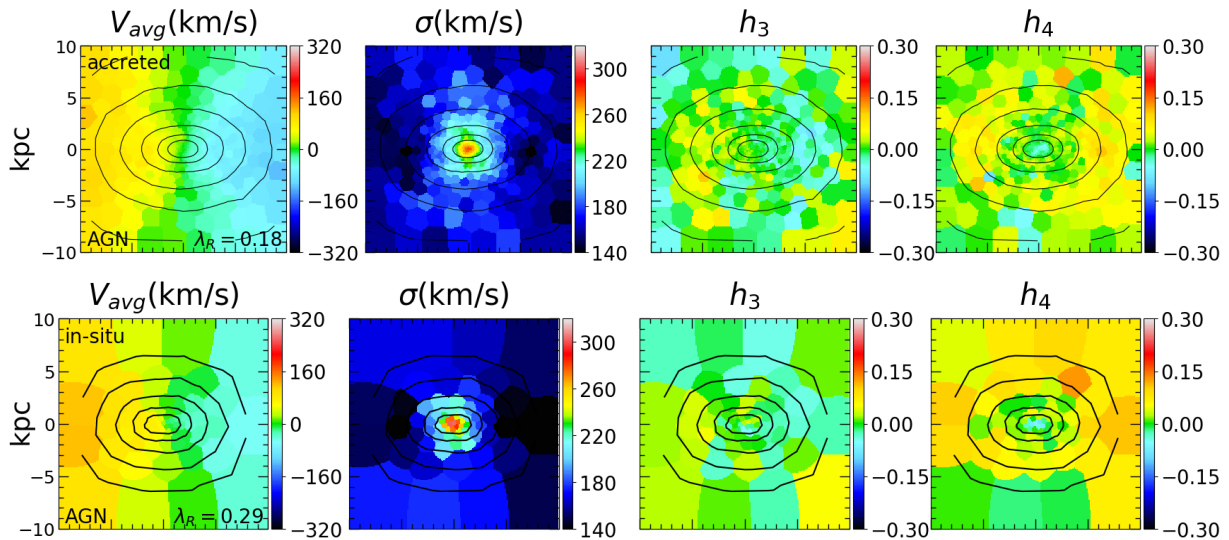
Figure 4.10: Stellar kinematics of the accreted (above) and in-situ formed (below) stars of galaxy 0227 simulated with AGN feedback. The overall in-situ fraction is 17% . In both cases the kinematics are pressure-supported, as no star formation happened since the last major merger at $z = 0.25$.

components to show very different kinematic (and stellar population) signatures (see e.g. Naab et al., 2014). To classify stars as in-situ or accreted, we trace stars in the galaxies throughout the simulation from $z = 2$ to $z = 0$, and label them as in-situ stars when they form within ten per cent of the virial radius (see Oser et al., 2010). All the remaining stellar particles are labelled as accreted. In the case of galaxy 0227 the in-situ fraction is $f_{\mathrm{in-situ}} = 0.50$ and $f_{\mathrm{in-situ}} = 0.17$ for the *NoAGN* and *AGN* cases, respectively. The values for the other galaxies are shown in Table 4.1.

Figures 4.9 and 4.10 show the stellar kinematic maps obtained for the separated in-situ and accreted components, in the *NoAGN* and *AGN* cases respectively. The accreted components (upper panels of Fig. 4.9 and 4.10) exhibit a very high velocity dispersion in both cases, but also have considerable net rotation, especially in the *NoAGN* case. This larger net rotation is probably caused by the potential being more oblate-shaped in the *NoAGN* simulation (the triaxiality parameter is $T = 0.41$; see Chapter 4.2). In the *AGN* case the galaxy has a very triaxial, almost prolate shape ($T = 0.86$), which hinders the amount of z-tube orbits (more on this in Chapter 4.1.7) causing less rotation.

The in-situ components are very different in the two cases. In the *AGN* case (lower panel of Fig. 4.10), the in-situ stars follow the same kinematics as the accreted ones. Almost all of these stars formed before the major merger at $z = 0.25$, which means that their original orbits have been scrambled, resulting in a dispersion-supported system. In the *NoAGN* case the number of in-situ-formed stars is larger, both before and after the major merger, and the corresponding kinematic maps are more complex. There are two distinct features. The first is an orderly fast-rotating disk in the midplane, with low velocity dispersion, a shallow $h_3 V_{\mathrm{avg}}/\sigma$ trend, and strongly negative h_4. The second is a slow-rotating bulge with high velocity dispersion and a much steeper trend with h_3. The first component is mostly made of young stars which formed after the $z = 0.25$ major merger, hence the orderly motion. The surrounding bulge is instead older. These stars formed in-situ at $z > 0.25$, and their orbits have been scrambled because of the major merger, resulting in less rotation. As the very high velocity dispersion suggests, there is also a counter-rotating component in this bulge, which explains why this component has a smaller net rotation than the accreted stars in the same potential.

This analysis implies that in-situ-formed stars and accreted stars tend to have intrinsically different kinematics from one another, at least until a major merger happens and scrambles their orbits. AGN feedback can thus significantly alter the present-day kinematics of galaxies by 'freezing' the kinematics at the most recent major merger, affecting the orbits of both accreted and in-situ-formed stars.

4.1.7   Orbit distribution

It is also of interest to directly study the distribution of stellar orbits, and how it is affected by AGN feedback. We classify star particles into three global orbit types: z-tubes (rotating around the z-axis), x-tubes (rotating around the x-axis, including inner and outer major axis tubes) and boxes (including π-boxes and boxlets). Figure 4.11 shows the fraction of these orbit families as a function of radius. In the *NoAGN* case, the fraction z-tube
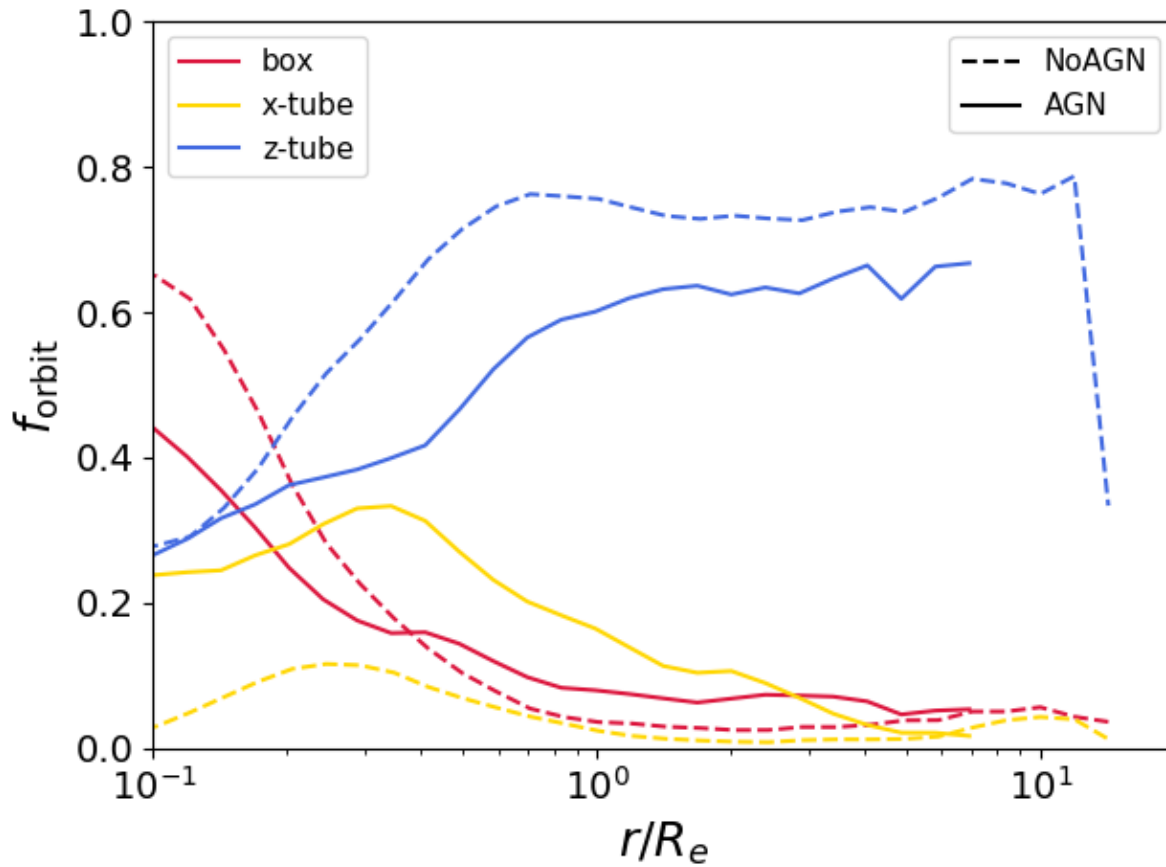
Figure 4.11: Radial frequency of three different types of orbits in our case study galaxy: z-tubes, x-tubes and boxes. The dashed line shows the *NoAGN* case, and the full line shows the *AGN* one. In the latter, the fraction of z-tube orbits drops considerably due to the suppression of disk formation, and the fraction of x-tube orbits increases due to the more triaxial potential.

orbits is larger at almost all radii. This is expected given the very prominent disk that has formed at low redshift. The central region is nevertheless dominated by box orbits, and x-tubes are very rare. In the *AGN* case there are significantly less z-tube orbits at all radii; the overall drop is from 65% to 49%, and the central regions are the ones that were impacted the most. The fraction of box orbits is slightly lower in the center and higher in the outskirts. What really changed is the fraction of x-tube orbits, which went from an overall 5% to 17%. The likely reason for this is that the potential of the *AGN* galaxy has a more prolate shape ($T = 0.86$, instead of $T = 0.41$ for the *NoAGN* case), allowing for this kind of orbits. This change in the balance of different orbit families also explains the positive correlation between h_3 and V_{avg}/σ; the bulk of the LOS velocity distribution is made of x-tube, box and retrograde z-tube orbits, and the prograde z-tube orbits add a high-velocity tail to it.

4.2   Results from the simulation sample

So far we focused on a single, example galaxy. Here we show more general results for all twenty galaxies in our sample. This analysis cannot reveal the statistical kinematic properties of quiescent galaxy populations from recent cosmological simulations (Dubois et al., 2016; Penoyre et al., 2017; Lagos et al., 2017; Schulze et al., 2018a). Instead, we would like to highlight the detailed impact of AGN feedback on massive galaxies for a few individual systems simulated at higher resolution. Table 4.1 shows for each galaxy in our sample the stellar mass $M_\star$ effective radius R_{e} the average stellar age, the in-situ formed fraction, the ellipticity ϵ the isophotal shape a_4/a , the triaxiality parameter T, λ_R , ξ_3 and the fraction of z-tube orbits $f_{\mathrm{z-tube}}$. The triaxiality parameter is computed using the reduced inertia tensor (see Chapter 4.1.2). The ratios between the square roots $\tilde{a} > \tilde{b} > \tilde{c}$ of the eigenvalues of this tensor are related to the axis ratios of a galaxy by:

$$b/a = (\tilde{b}/\tilde{a})^{\sqrt{3}} \quad \text{and} \quad c/a = (\tilde{c}/\tilde{a})^{\sqrt{3}} . \tag{4.2}$$

The triaxiality parameter can then be computed as

$$T = \frac{1 - (b/a)^2}{1 - (c/a)^2}. \tag{4.3}$$

When $T = 0$ the galaxy is perfectly oblate, while when $T = 1$ the galaxy is perfectly prolate. If the galaxy is close to spherical, the definition breaks down.
In Table 4.1 we see that in general all our galaxies have a lower stellar mass with AGN feedback due to the quenching of star formation, while the effective radius increases due to less dissipation (e.g. Crain et al., 2015; Choi et al., 2018). In the following sections we will look at the distribution of kinematic (λ_R , ξ_3 , orbit families) and morphological (a_4/a , triaxiality) properties at $z = 1$ and $z = 0$, and how AGN feedback affects them.

GalID		$M_\star$ $[10^{10} M_\odot]$	R_e [kpc]	¡age¿ [Gyr]	$f_{in-situ}$	ϵ	a_4/a	T	λ_R	ξ_3	$f_{\text{z-tube}}^{\text{pro}}$
0175	NoAGN	26.73	1.86	7.85	0.23	0.24	0.017	0.72	0.08	-0.05	0.56
0175	AGN	18.93	2.57	10.72	0.10	0.35	0.001	0.51	0.12	-6.58	0.45
0204	NoAGN	19.59	3.09	8.17	0.65	0.78	0.196	0.29	0.46	-7.07	0.14
0204	AGN	16.41	2.06	9.50	0.31	0.37	0.026	0.15	0.36	-8.19	0.38
0215	NoAGN	27.79	1.76	9.61	0.28	0.38	0.042	0.48	0.37	-5.14	0.39
0215	AGN	7.38	1.70	11.26	0.12	0.31	0.018	0.50	0.02	-0.79	0.15
0227	NoAGN	48.46	3.27	7.72	0.50	0.49	0.124	0.41	0.47	-8.10	0.27
0227	AGN	22.24	2.60	9.95	0.17	0.15	0.000	0.86	0.10	0.50	0.62
0290	NoAGN	26.32	2.95	8.55	0.56	0.71	0.112	0.28	0.52	-11.49	0.48
0290	AGN	12.67	2.57	10.45	0.29	0.38	0.045	0.66	0.06	-2.62	0.38
0408	NoAGN	7.57	1.88	9.12	0.32	0.24	0.020	0.68	0.07	1.82	0.68
0408	AGN	15.98	2.59	8.84	0.58	0.43	0.055	0.32	0.36	-6.41	0.27
0501	NoAGN	6.80	1.74	10.71	0.14	0.33	0.029	0.22	0.42	-6.74	0.59
0501	AGN	8.25	1.93	11.22	0.16	0.30	0.018	0.44	0.10	-3.55	0.62
0616	NoAGN	8.61	1.29	8.87	0.30	0.38	0.055	0.09	0.04	-1.02	0.17
0616	AGN	4.56	1.53	11.07	0.09	0.35	0.010	0.36	0.35	-7.27	0.08
0664	NoAGN	8.04	1.15	9.50	0.35	0.41	0.031	0.37	0.44	-5.74	0.69
0664	AGN	7.23	1.38	10.51	0.22	0.43	0.052	0.09	0.32	-7.61	0.56
0858	NoAGN	3.67	2.25	8.97	-1.00	0.36	0.045	0.25	0.49	-6.02	0.49
0858	AGN	6.99	1.93	8.11	0.49	0.26	0.006	0.38	0.31	-7.20	0.37

Table 4.1: General properties of our sample of simulated galaxies.
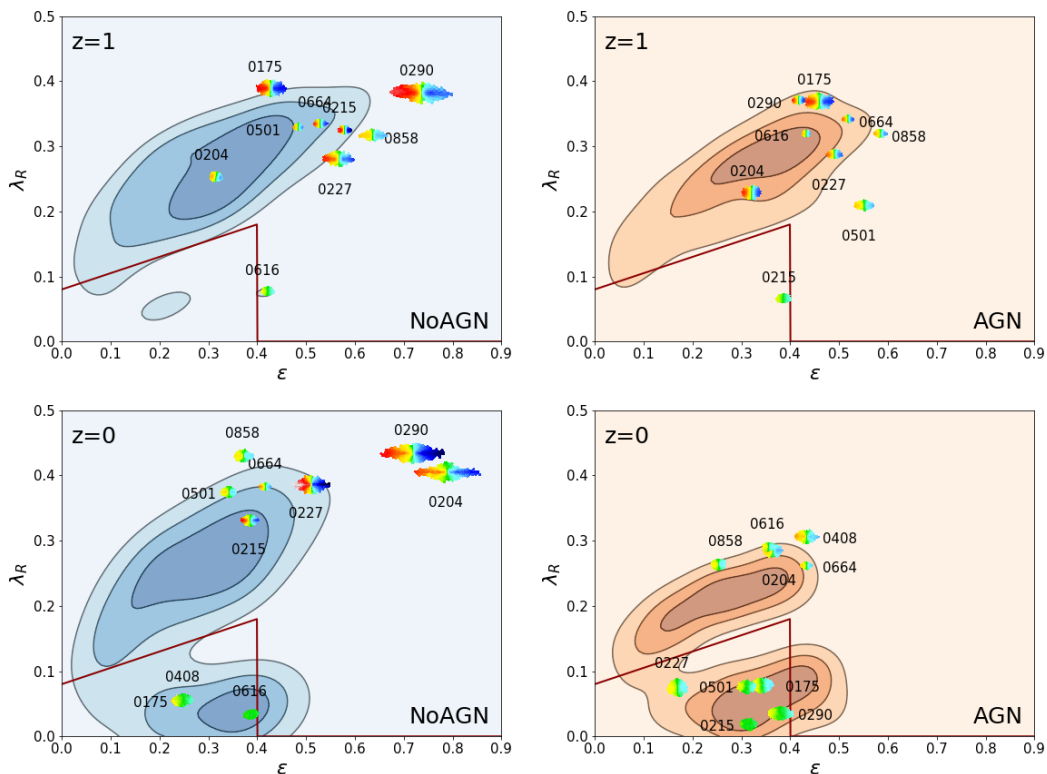
Figure 4.12: λ_R as a function of ellipticity ϵ for the galaxies at redshift $z = 1$ (top panels) and $z = 0$ (bottom panels), simulated without (*NoAGN*, left) and with (*AGN*, right) AGN feedback. The edge-on values are indicated by velocity maps. The coloured contours indicate the distribution of our galaxies when they are seen from 50 random orientations each. The dark red line marks the limit between slow- and fast-rotators according to Cappellari (2016). With AGN feedback the systems become rounder and rotate more slowly at z=0.
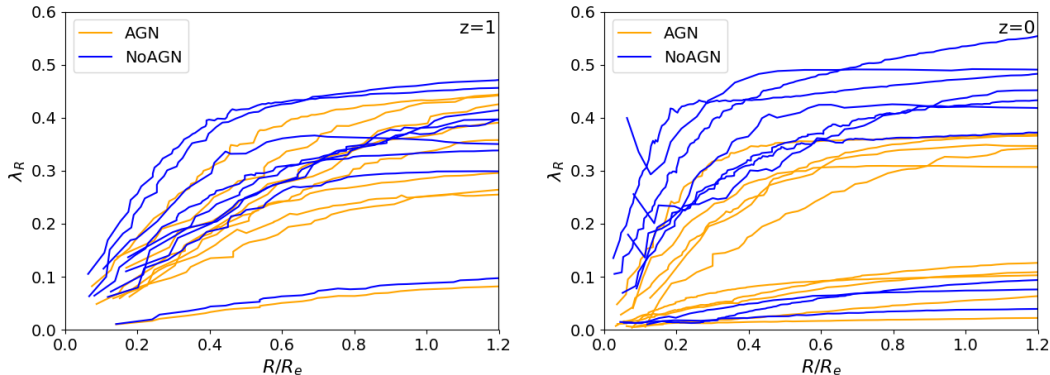
Figure 4.13: λ_R radial profiles of our galaxy sample at z=1 (left) and z=0 (right). The *AGN* galaxies (orange) evolve towards lower λ_R values than their *NoAGN* counterparts (blue).

4.2.1 Angular momentum

In Fig. 4.12 we plot the λ_R parameter of the sample galaxies versus their ellipticity ϵ for the simulations without (*NoAGN*, left panels) and with AGN (*AGN*, right panels) at redshift $z = 1$ (top panels) and $z = 0$ (bottom panels). The location of edge-on projections are indicated by the velocity maps. The blue/orange shaded regions indicate the typical distribution of these systems for random orientations (projection effects for λ_R based on simulations are discussed in e.g. Jesseit et al., 2009; Naab et al., 2014; Lagos et al., 2018). They were obtained by calculating λ_R and ϵ for 50 random lines-of-sight for each galaxy. The red line separates slow- and fast-rotators following to the definition by Cappellari (2016) (Eq. 2.5). The distribution of galaxies at $z = 1$ is similar between the *AGN* and *NoAGN* cases, with most galaxies being flattened fast-rotators with λ_R in the range $0.2 < \lambda_R < 0.4$. The ellipticity values are a bit higher in the *NoAGN* case ($0.3 < \epsilon < 0.8$) than in the *AGN* one ($0.3 < \epsilon < 0.6$), but qualitatively the two populations are very similar. By $z = 0$ many (7 out of 10) of the *NoAGN* galaxies are still fast rotators with a similar ellipticity distribution. This trend is in agreement with results for massive galaxy populations from cosmological box simulations without AGN feedback Dubois et al. (2016). Instead, in the *AGN* case by $z = 0$ the galaxies have become rounder ($\epsilon < 0.4$) and more slowly rotating, with λ_R no larger than ~ 0.35. More than half of the galaxies would be considered bona-fide slow rotators even in their edge-on projections. As discussed earlier, the trend towards slower rotation with AGN feedback is caused by the suppression of late in-situ star formation (see Brennan et al., 2018 for a discussion of ejective and preventative AGN feedback), which in most cases significantly reduces rotation observed at $z = 0$. The effect is strongest for the largest and most massive galaxies in our samples (lower numbers, like 0227), which - without AGN feedback - develop massive fast-rotating disk structures (In the case of galaxy 0175, this young disk structure is on a different plane, and thus does not increase λ_R significantly). We find a correlation between λ_R and

ϵ, at least for the fast-rotators: faster rotating galaxies tend to be more flattened. Most of our slow-rotating galaxies exhibit a relatively high ellipticity, which is a trend found in other simulation studies as well(Bois et al., 2010; Naab et al., 2014), and possibly due to resolution limits. An interesting case is galaxy 0616, which contradicts our expectations by being a slow-rotator when simulated without AGN feedback but turns into a fast-rotator when simulated with AGN feedback. What happens here? In the *NoAGN* case gas infall triggers a starburst that forms a disk that counter-rotates with respect to the rest of the galaxy. This lowers the projected λ_R value, but leaves a relatively high ellipticity. In the *AGN* case the gas is kept from forming this new disk and the galaxy retains most of the (projected) angular momentum of the older stellar component.

In Figure 4.13 we plot the λ_R radial profiles for all galaxies, at $z = 1$ and $z = 0$. Typically, the values increase from the center until they reach an asymptotic value, usually within R_e. This is consistent with previously published simulation data, even though we are missing systems with dropping λ_R profiles (Naab et al., 2014; Wu et al., 2014; Lagos et al., 2018). At $z = 1$ there is not much difference between the *AGN* and *NoAGN* galaxies, while at $z = 0$ galaxies simulated with AGN feedback show once again systematically lower λ_R values, even among the fast-rotators. Many galaxies that would be rotationally-supported without AGN, become pressure-supported when an AGN is present. Overall, AGN feedback results in more slow-rotating and dispersion-supported galaxies in agreement with previous simulations (Dubois et al., 2016) and the statistics of observed early-type galaxies.

4.2.2 Higher-order kinematics and orbital structure

As discussed in Chapters 2.1.3 and 4.1.5, rotating galaxies are expected to have anti-correlated h_3 and velocity fields, but the degree of this anti-correlation depends on the orbital structure of the galaxy, and we can employ our ξ_3 parameter to evaluate this for our sample. In Figure 4.14 we plot ξ_3 as a function of λ_R at $z = 1$ and $z = 0$. The edge-on values are plotted with velocity maps, while the contours represent the location of the sample in the ξ_3- λ_R plane for random orientations. Generally, the edge-on ξ_3 values are larger in absolute value, but for different inclinations the dependence of ξ_3 on the viewing angle is weak. At $z = 1$ all galaxies have a negative of ξ_3 and h_3 is anti-correlated with the velocity, as expected for fast-rotators. This is also true for the two galaxies which are slow-rotators (according to λ_R) at $z = 1$. At $z = 0$ the sample splits into two groups: slow-rotators with low values of λ_R tend to have $\xi_3 \sim 0$ (very steep correlation or no correlation), while all fast-rotators have $\xi_3 < -3$ (negative correlation). The specific value of ξ_3 for the fast-rotators depend on their orbital structure; the galaxies where a disk feature is particularly prominent (0204, 0227 and 0290 in the *NoAGN* case) have the lowest values, reaching about $\xi_3 = -11.5$. In other words, more flattened and simple rotating systems have a less steep correlation between h_3 and V_{avg}/σ than fast-rotators with more complex kinematics. A similar behaviour was also observed in real galaxies by Veale et al. (2017). This results in a weak correlation between ξ_3 and λ_R for the fast-rotators, that was not present at $z = 1$ when the kinematics of the galaxies were overall simpler. The

bi-modality of slow- and fast-rotators in the ξ_3-λ_R plane is seen in both the *NoAGN* and *AGN* cases, but with AGN feedback the group of galaxies with $\xi_3 \sim 0$ is larger. A few galaxies have a positive value of ξ_3 at $z = 0$. One of them, 0227 *AGN*, has already been extensively discussed. The other one, 0408 *NoAGN*, has a positive value because of a sub-dominant rotating component in an otherwise dispersion-supported system, producing a positive correlation between h_3 and V_{avg}.

If we compare these results with observational IFU surveys, we find a small discrepancy. In Figure 4.15 we plot the ξ_3 values of galaxies from the ATLAS^{3D} survey (Cappellari et al., 2011)[1], compared with the contours of our *AGN* simulations seen at random inclinations. The ATLAS^{3D} values also include a re-extraction of the kinematics from the subset of galaxies in the SAURON survey originally presented in Emsellem et al. (2004). To compute ξ_3 and λ_R for the ATLAS^{3D} sample, we only considered spaxels with $\sigma > 120$km/s, since the Gauss-Hermite moments can only be extracted from the data when the galaxy velocity dispersion is well resolved by the spectrograph (e.g. Cappellari and Emsellem, 2004). The distribution of ξ_3 values is similar between observations and simulations, and can be divided in two groups: slow-rotators with $\xi_3 \sim 0$ and fast-rotators with $-3 < \xi_3 < -10$. However, at given λ_R the ATLAS^{3D} galaxies seem to have lower ξ_3 (in absolute value) than the simulations. We believe there are at least three reasons for this difference. Several of the ATLAS^{3D} fast-rotators have strong bar features, which are not present in our sample of simulations. In their presence the kinematic maps often show a positive correlation between V_{avg} and h_3 (Chung and Bureau, 2004), causing ξ_3 values closer to zero or sometimes even positive. In Figure 4.15 galaxies with clear bars have been highlighted, but hidden or weak bars could be present in the other galaxies too, affecting the h_3 values. Secondly, as previously mentioned, constraining the h_3 value of each spaxel is harder in observations. The selection of spaxels with $\sigma > 120$km/s limits this problem, but does not eliminate it. This results in more noisy h_3 maps, which makes the h_3-V_{avg}/σ trend less tight, and thus moves the ξ_3 value of observed galaxies closer to zero. At equal σ, this effect is stronger for slower-rotating galaxies, as their LOS velocity distribution have lower h_3 values. Lastly, our (*AGN*) sample consists of only 10 massive galaxies, all of which have relatively low λ_R values. This means that our simulations do not explore the $\lambda_R > 0.3$ regime, but if they did, we would expect most of them to have $-10 < \xi_3 < -5$, like many of the galaxies in our *NoAGN* sample, matching the observations.

4.2.3 Orbit distribution and ξ_3

We would also like to see how closely connected ξ_3 is to the actual orbital structure of galaxies, measured in the same way as in Chapters 2.2.3 and 4.1.7. In Figure 4.16 we plot ξ_3 as a function of the fraction of prograde z-tube orbits within R_{e}, $f_{\mathrm{z-tube}}^{\mathrm{pro}}$, at $z = 0$. The plotted ξ_3 values are the average for 50 random views of each galaxy, and the error bars mark the dispersion (negligible for galaxies 0616 *NoAGN* and 0215 *AGN*). Most galaxies with high values of $f_{\mathrm{z-tube}}^{\mathrm{pro}}$ have a $\xi_3 < -3$ as expected, and there is a rough correlation

---

[1]Available from http://purl.org/atlas3d
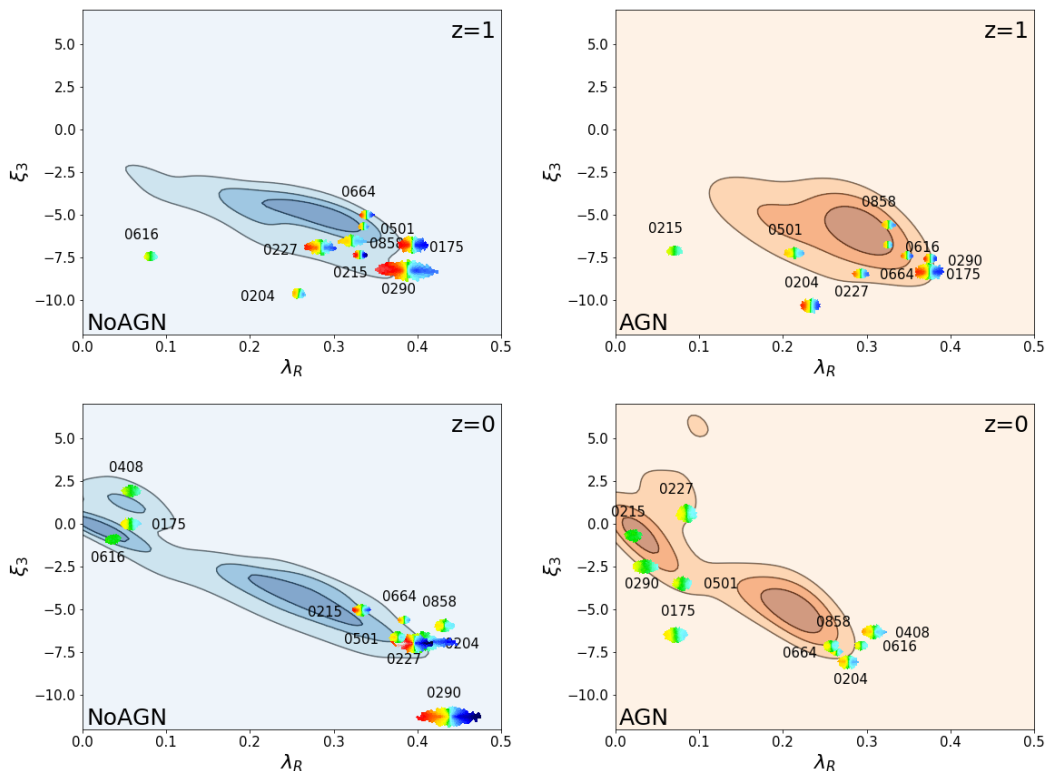
Figure 4.14: ξ_3 versus λ_R at $z = 1$ (top panels) and $z = 0$ (bottom panels), simulated without (left) and with (right) AGN feedback. The kinematic map markers indicate the values when the galaxy is seen edge-on, while the density contours indicate the distribution when our galaxies are seen through 50 random orientations each. At $z = 1$ all galaxies have have values of ξ_3 in the anti-correlation regime, typical of fast-rotators, while at $z = 0$ many galaxies have $\xi_3 \sim 0$ or in a few cases even positive, and this effect is stronger with AGN feedback.
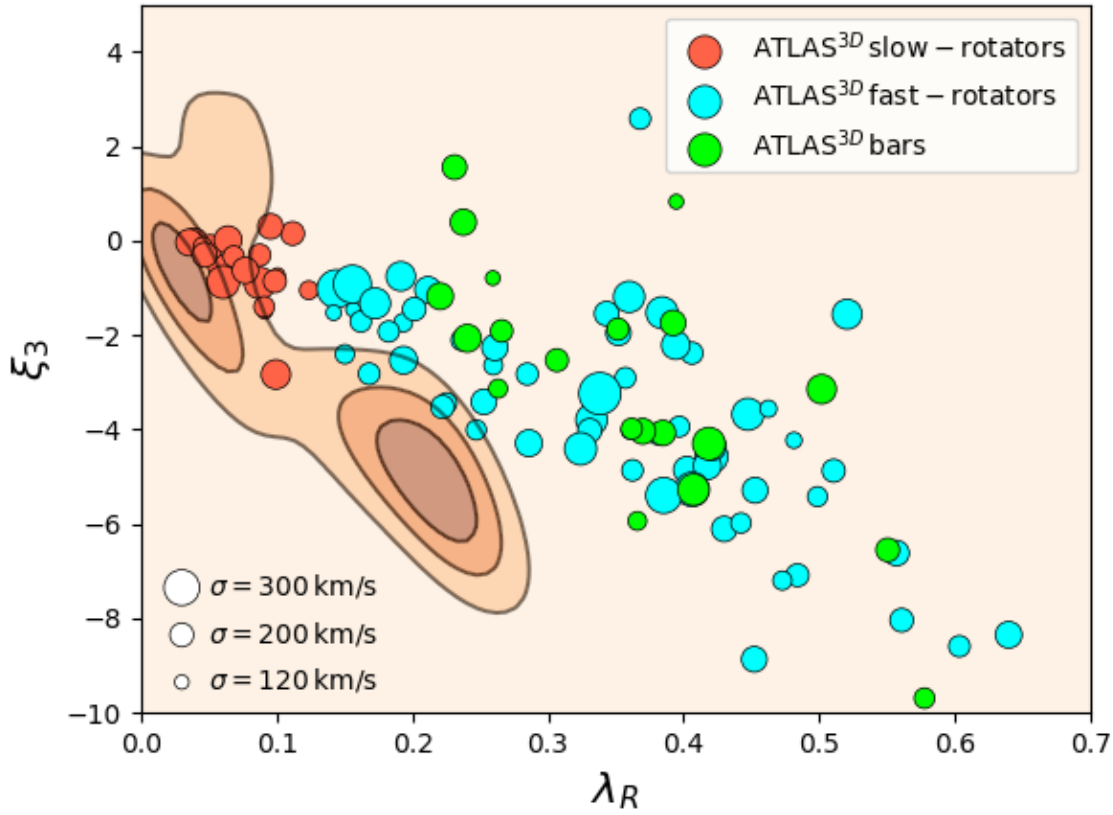
Figure 4.15: ξ_3 as a function of λ_R for the galaxies from the ATLAS^{3D} sample (circle markers), compared with our AGN simulations (orange contours; same as Figure 4.14). The ATLAS^{3D} galaxies are distinguished in slow-rotators (red) and fast-rotators (light blue) according to the Cappellari (2016) definition. At equal λ_R, observed fast-rotators seem to have smaller ξ_3 (absolute) values than the simulation, possibly because of more complex kinematic features (bars) and of more noisy h_3 measurements. Slow-rotators have $\lambda_R \sim 0$ and $\xi_3 \sim 0$ in both observations and simulations.

between the two quantities. The galaxy with the highest $f_{\mathrm{z-tube}}^{\mathrm{pro}}$ (0290 *NoAGN*) is also the one with the lowest value of ξ_3: ~ -11.5 when seen edge-on and ~ -6.5 when averaging between many different viewing angles. The reason for this is that when the system is dominated by orbits that rotate (progradely) around the z axis, these stars form the bulk of the LOS velocity distribution, and all other orbit types make the h_3 signal stronger for that given V_{avg}/σ. When non-rotational orbits are dominating ($f_{\mathrm{z-tube}}^{\mathrm{pro}} \sim 0$), then $V_{\mathrm{avg}}/\sigma \sim 0$ and consequently $\xi_3 \sim 0$.

A few galaxies (0175 *NoAGN*, 0408 *NoAGN* and 0227 *AGN*) have a positive correlation between h_3 and V_{avg}/σ in large parts of their kinematic maps, resulting in a positive value of ξ_3. This is likely connected to the fact that these galaxies have a prolate potential. We investigate this by plotting ξ_3 as a function of the triaxiality parameter T in Figure 4.17. There seems to be a rough correlation between the two quantities in our sample. The most prolate galaxies ($T \sim 1$) have positive values of ξ_3, while almost all oblate galaxies ($T << 1$) have negative values. The one exception is galaxy 0616 *NoAGN*, which as already discussed is made of two counter-rotating components and looks like a 'fake' slow-rotator. This connection between morphology and kinematics likely arises because different potential shapes allow different kinds of orbits; specifically, x-tubes are more common in prolate potentials. We see this by plotting ξ_3 as a function of the fraction of x-tube orbits f_{x-tube} in Figure 4.18. There is again a rough correlation, meaning that galaxies with higher f_{x-tube} are more likely to display a positive correlation between h_3 and V_{avg}/σ in their kinematic maps. This follows from the correlation between f_{x-tube} and the triaxiality T, which has previously been observed in isolated (Jesseit et al., 2005) and cosmological simulations (Röttgers et al., 2014). It should however be noted that in a pure prolate system only x-tube orbits and box orbits are allowed, and if there is net rotation around the long axis h_3 and V_{avg}/σ become anti-correlated again. We do not see this in our sample because none of our galaxies is dominated by x-tube orbits (at most $f_{x-tube} = 0.25$, for 0227 *AGN*).

4.2.4 Isophotal shape

In Fig. 4.19 we plot the a_4/a parameter of all our galaxies versus their ellipticity ϵ at $z = 1$ and $z = 0$. Like for Figs. 4.12 and 4.14, we also added contours to show the distribution of values for smaller inclinations. At $z = 1$ the panels with and without AGN feedback look qualitatively very similar. All galaxies have disky isophotes when viewed edge-on. When viewing the galaxies from different points of view both the ellipticity and the a_4/a values tend to become smaller. At $z = 0$, the cases with and without AGN behave as expected. The *NoAGN* galaxies show systematically higher a_4/a values, due to the formation of embedded stellar disks at low redshift. In the *AGN* case the a_4/a values are lower, meaning that the isophotes are less disky and closer to elliptical. Even though we do not have a clearly boxy galaxy in our sample, two galaxies (0175 and 0227) have almost perfectly elliptical isophotes.

We also studied the three-dimensional shape of our galaxies through the triaxiality parameter T (see Chapter 4.2 for its definition). The values of T for our galaxies are found in table 4.1, or in Figure 4.17. We found that with AGN feedback a bigger fraction of
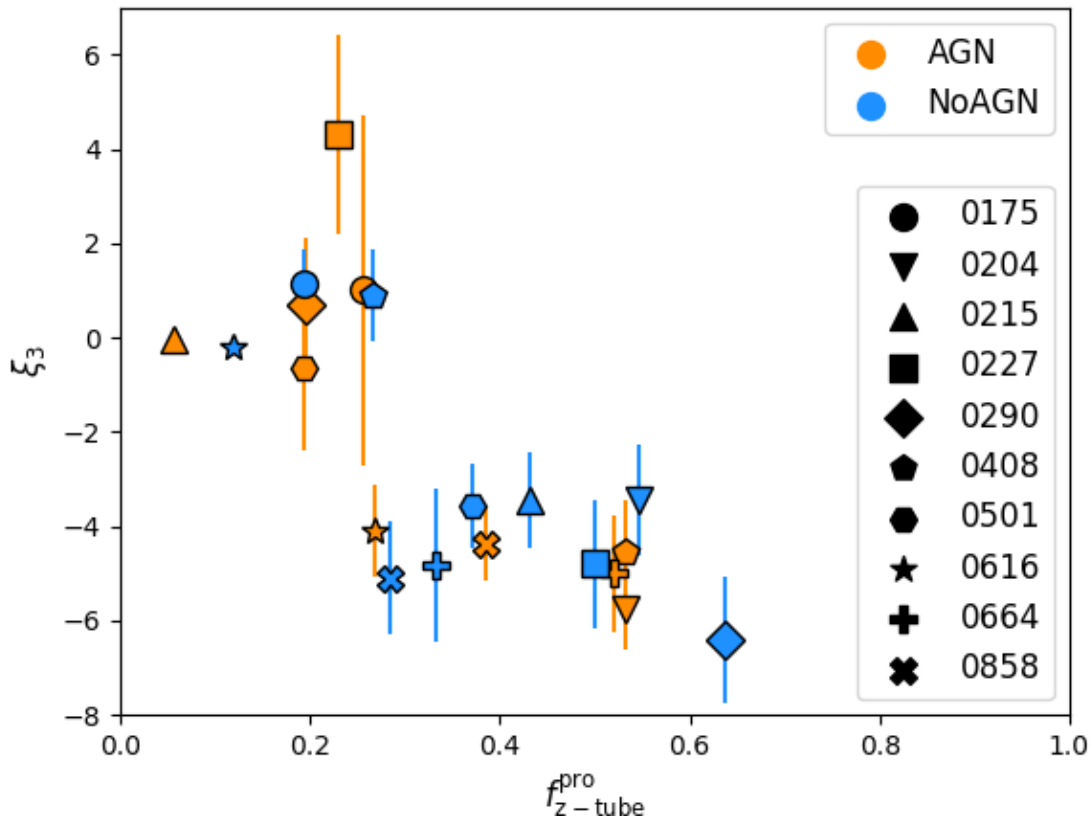
Figure 4.16: ξ_3 as a function of the fraction of prograde z-tube orbits f_{z-tube}^{pro} for our sample of simulated galaxies at $z = 0$. The ξ_3 values of each galaxy are an average over 50 random views, and the error bars are their standard deviation. Galaxies with high f_{z-tube}^{pro} tend to have $\xi_3 < -5$.
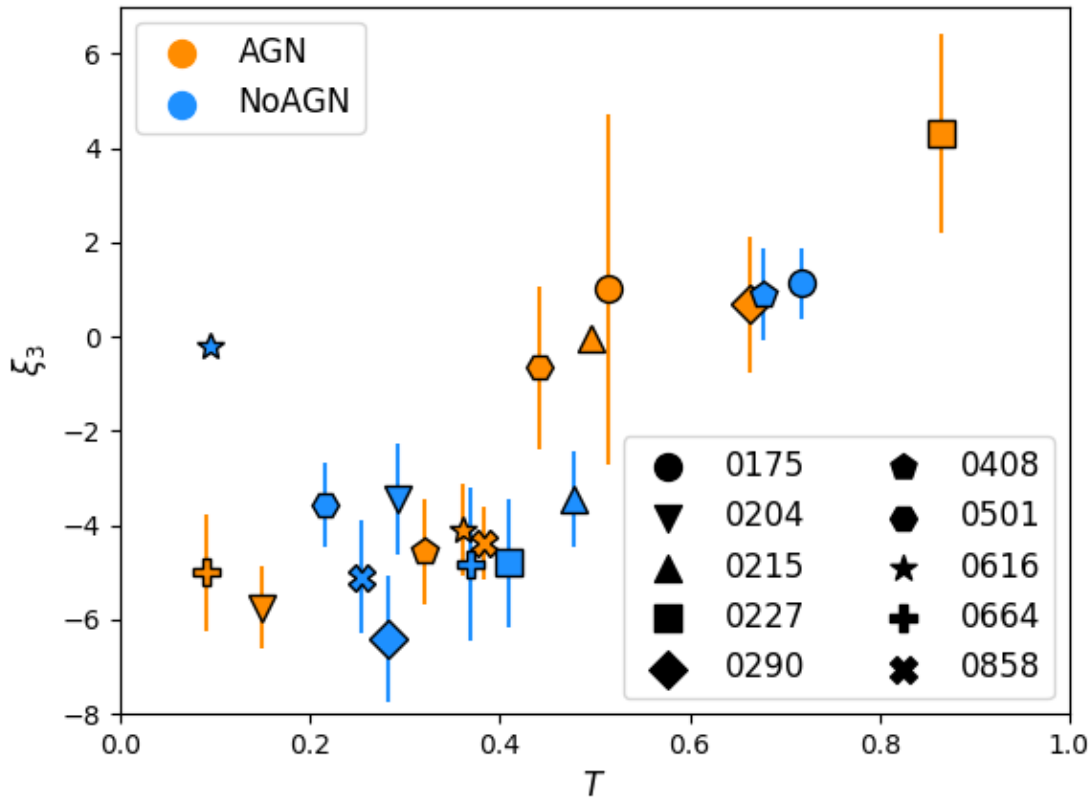
Figure 4.17: ξ_3 as a function of the triaxiality parameter for our sample of simulated galaxies at $z = 0$. The ξ_3 values of each galaxy are an average over 50 random views, and the error bars are their standard deviation. There is a weak correlation between the two parameters: prolate galaxies have positive values of ξ_3 , while oblate galaxies have negative values.
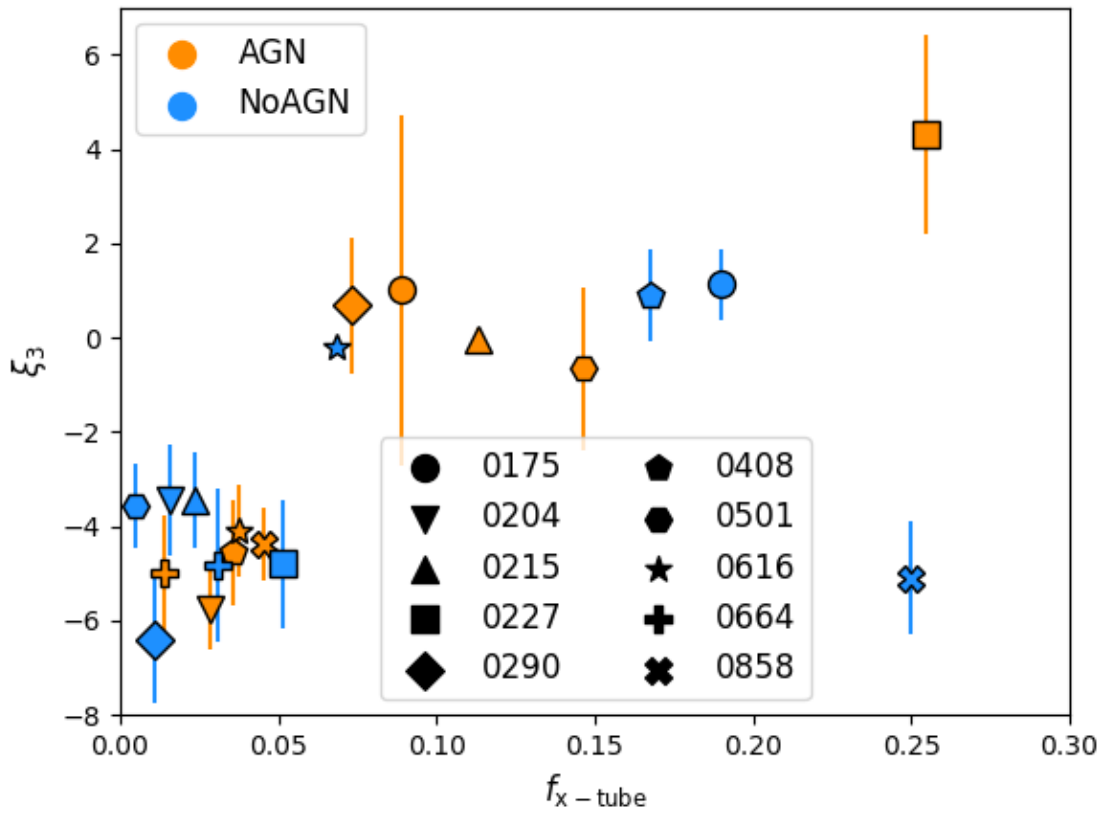
Figure 4.18: ξ_3 as a function of the fraction of x-tube orbits f_{x-tube} for our sample of simulated galaxies at $z = 0$. The ξ_3 values of each galaxy are an average over 50 random views, and the error bars are their standard deviation. Galaxies with high f_{x-tube} tend to have $\xi_3 > 0$.
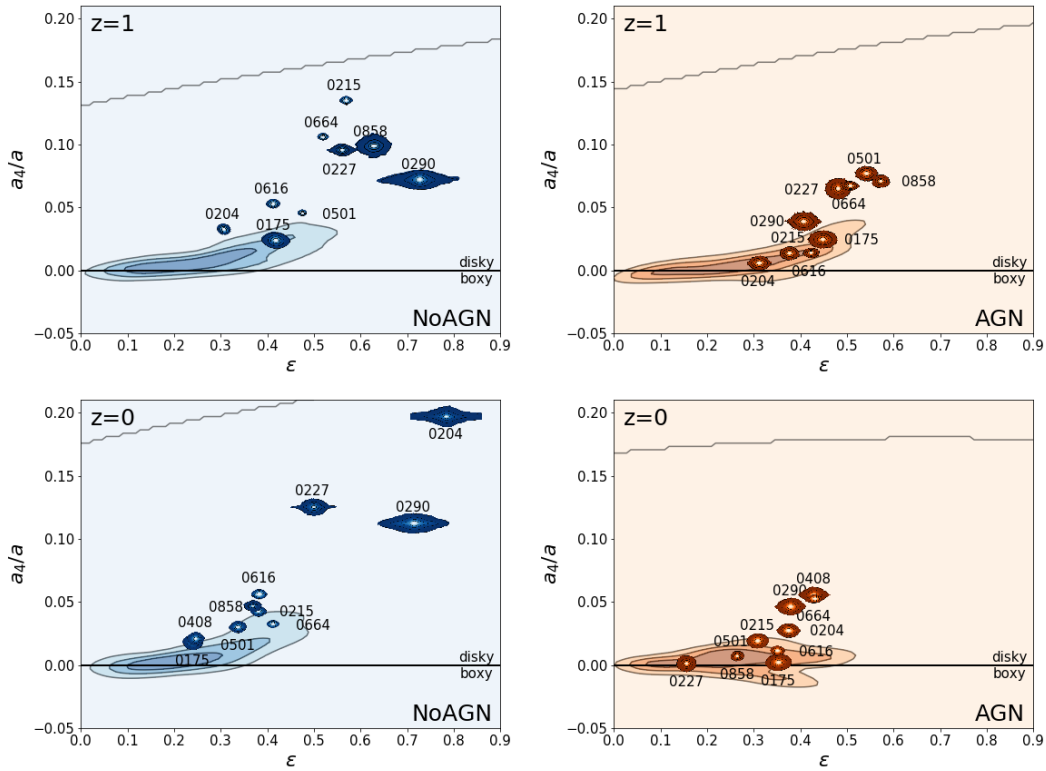
Figure 4.19: a_4/a versus galaxy ellipticity ϵ at $z = 1$ (top panels) and $z = 0$ (bottom panels), simulated without (left) and with (right) AGN feedback. The edge-on locations are indicated by the isophotal maps, while the density contours indicate the distribution of our galaxies when they are seen from 50 random orientations each. The black line indicates elliptical isophotes and separates boxy ($a_4 < 0$) from disky ($a_4 > 0$) galaxies. Galaxies with AGN feebdack are rounder and have more elliptical - in one case even boxy - isophotes at $z = 0$.

our galaxies (five out of ten, instead of two out of ten) has a triaxial or almost prolate shape ($T > 0.5$). A prolate shape is more common for massive ellipticals, as found in both observations (Tsatsi et al., 2017; Krajnović et al., 2018; Graham et al., 2018) and simulations (Li et al., 2017). Without AGN feedback more of our galaxies are oblate ($T \sim 0$) despite their larger mass, which makes them more similar to the significantly less massive fast-rotators we observe (Krajnović et al., 2011; Cappellari, 2016).

4.3   Summary

From the analysis of these simulated galaxies emerges a clear picture, which confirms the previous studies on the subject and adds new insights. The energy output of AGNs heats up and pushes away the interstellar gas, effectively suppressing the in-situ formation of stars. This affects the kinematics and morphology of the systems with a stronger impact at later cosmic times, when the central black holes become more massive. In our simulations AGN feedback results in realistic early-type galaxy properties at $z = 0$. From our detailed stellar assembly, stellar population, mock IFU, isophotal shape and stellar orbit analysis we get the following generic picture:

- The stellar kinematics of massive early-type galaxies is significantly affected by AGN feedback, as seen both in the mock observational kinematic maps and in the orbit analysis of our simulation. Without AGN feedback massive early-type galaxies would develop young fast-rotating stellar disks even at low redshift, giving them kinematic signatures typical of less massive fast-rotators. With AGN feedback massive early-type galaxies are instead more likely to become slow-rotators due to the suppression of late in-situ star formation, in agreement with previous studies (Dubois et al., 2013; Martizzi et al., 2014; Penoyre et al., 2017; Lagos et al., 2018).

- As shown in Figure 4.6, the slowing-down effect of AGN feedback is more pronounced in, but not limited to, late major mergers. Apart for some cases where mergers can cause a spin-up of the galaxy thanks to a favourable orbital configuration (Naab et al., 2014), most of the time mergers tend to disrupt the orbits of stars, reducing the angular momentum of the galaxy. However, without AGN feedback the further accretion of gas can produce a new rotating stellar disk and make the galaxy recover its angular momentum. With AGN feedback the in-falling star-forming gas is heated up and blown away. The origins of this mechanism lie in the different spatial and kinematic properties of in-situ-formed and accreted stars (Rodriguez-Gomez et al., 2016).

- AGN feedback starts having a significant impact on the stellar angular momentum only after $z = 1$, and is stronger for more massive galaxies. With some exceptions, like galaxy 0616 in our sample which without AGN feedback develops a counter-rotating core, having AGN feedback always decreases the angular momentum of the galaxies in our sample.

- We compute the ellipticity ϵ and the a_4/a isophotal shape parameter and follow their evolution through cosmic time. By suppressing the formation of disks, AGN feedback makes galaxies less flattened and their isophotes significantly less disky (more elliptical or even boxy), especially when seen edge-on. Like for the angular momentum, this difference starts arising at $z \sim 1$, and its effect is again stronger for the most massive galaxies of our sample.

- We introduce a new global parameter, ξ_3, to quantify the anti-correlation between the LOS-velocity and h_3 from two-dimensional kinematic maps. Slow- and fast-rotators have different typical values of this parameter, owing to their different orbital structures. AGN feedback pushes the ξ_3 value towards the slow-rotator regime ($\xi_3 \sim$ 0, meaning a very steep anti-correlation between V_{avg}/σ and h_3 or lack of such a correlation).

- We perform a full orbit analysis for all simulated galaxies and find that systems with AGN feedback have a higher fraction of x-tube and box orbits and a lower fraction of z-tubes. This is consistent with them being more triaxial due to the lack of late in-situ star formation and the more stellar accretion dominated assembly history. We find that the ξ_3 parameter is well correlated to the fractions of prolate z-tubes and x-tubes, as well as with the triaxiality of the galaxy.

- We compared the ξ_3 values of our simulations with observed galaxies from the ATLAS^{3D} sample, finding an interesting discrepancy. At equal λ_R, observed fast-rotators seem to have values of ξ_3 closer to zero and sometimes even positive; this could be because many of these galaxies show bar features, which cause a positive correlation between h_3 and LOS velocity, and/or possibly because of noise in the observed h_3 values. Our *AGN* sample also lacks galaxies with high λ_R values, which are instead very common in the ATLAS^{3D} sample.

Even though slow-rotating galaxies could also form without AGN feedback through particularly gas-poor formation paths, our simulations suggest that AGN feedback might be essential to produce the observed amount of quiescent, slow-rotating and non-disky early-type galaxies. The impact of AGN on the rotation properties are in line with earlier studies using different AGN feedback models and simulation codes (Dubois et al., 2013; Martizzi et al., 2014; Penoyre et al., 2017; Lagos et al., 2018). In this study we indicate that also higher-order properties in the isophotal shape and line-of-sight kinematics, as well as the underlying orbital content, are significantly affected by accreting supermassive black holes. The effects typically results in a better agreement with observations. The newly introduced kinematic asymmetry parameter ξ_3 might provide a useful diagnostic for large integral field surveys, as it is a kinematic indicator for intrinsic shape and orbital content.

Chapter 5

Testing observational methods for measuring the masses of galaxies

In this chapter we use our set of zoom simulations to test observational methods for determining the total mass and density profile of galaxies. Understanding the redshift evolution of a galaxy's mass distribution, and in particular of its dark matter content, is crucial for our understanding of galaxy formation. Cosmological simulations connected the dark matter fraction and density slope of galaxies to their formation processes: merger history, in-situ star formation vs accretion of satellites, feedback events,... (e.g. Remus et al., 2017, Peirani et al., 2019). However, evaluating them in real galaxies is not trivial. The total mass distribution of galaxies can be inferred through several methods with varying degrees of complexity and accuracy. Jeans dynamical modelling (e.g., Cappellari et al., 2013b) consists in fitting the 2D kinematics of a galaxy with the ones of a model produced from the Jeans equations under a certain set of assumptions (see Chapter 2.3.2). Schwarzschild dynamical modelling (e.g., Thomas et al., 2007) constructs model kinematic maps by summing orbits of different families, and then fits them to the observational maps to constrain both the mass and orbital distributions at the same time. Strong gravitational lensing can also provide accurate mass estimates (e.g., Auger et al., 2010) for the galaxies that exhibit lensing effects; more on that in Chapter 5.2. In all of these cases, the dark matter content is then calculated by subtracting the stellar and gas mass, which introduce their own complications: varying stellar mass-to-light ratios, dust absorption,... It is therefore not straight-forward to determine, and observational estimates typically have very large uncertainties. Because of this, simple mass-estimating formulas that only take into account the central velocity dispersion became popular (e.g., Cappellari et al., 2013a). These difficulties create a gap between the theoretical understanding of galaxies and modern observations. Simulations have been used in the past to test these methods. For instance Lablanche et al. (2012) tested Jeans dynamical modelling using N-body simulations of merger remnants that mimic specific galaxies, and Thomas et al. (2007) tested Schwarzschild modelling on simulated disk-disk merger remnants. In this Chapter we would like to test the mass estimates of Jeans dynamical modelling (Chapter 5.1) and gravitational lensing (Chapter 5.2) using our set of more realistic zoom simulations. We would also like to see whether

certain galactic properties correlate with the accuracy of the estimations and whether AGN feedback has a measurable impact on the density profile slopes.

5.1 Dynamical modelling

We modelled the kinematics of our simulated galaxies using the Jeans Anisotropic Model (JAM, Cappellari (2008)) code, which solves the Jeans equations under a certain set of assumptions (see Chapter 2.3.2). Most notably it assumes that the system is stationary, axisymmetric, and that the anisotropy of the meridional plane β_z is constant:

$$\beta_z \equiv 1 - \frac{\sigma_z}{\sigma_R} = cost. \tag{5.1}$$

The Jeans equations then allow to predict the LOS kinematics of a tracer (stars, gas,...), given its luminosity distribution and the galactic gravitational potential. By varying the parameters of the potential one can then minimize the difference between real and model kinematics, and thus obtain the best-fitting mass model.

5.1.1 Mock observational data

In the case of our simulations we used stars as the tracer and produced mock-observational stellar luminosity and stellar kinematics data to use in the modelling. The galaxy models were oriented at exactly 80 degrees (where 90 is edge-on), in order to avoid the extreme case of 90 degrees but still have a good view of the galaxy's rotation. We constructed kinematic maps in the same way as the previous Chapters (see Chapter 4.1.2), but instead of fitting the LOS velocity distribution with a Gauss-Hermite function we calculate the 'true' average and velocity dispersion:

$$V_{\text{avg}} = \frac{1}{N} \sum_i V_i \quad , \quad \sigma = \sqrt{\frac{1}{N} \sum_i (V_i - V_{\text{avg}})^2} \tag{5.2}$$

where the index i runs through the particle in each Voronoi spaxel. We did this because we need to compare this data with the output of the Jeans equations, which provide the true second moments of the velocity distribution. Additionally the Voronoi binning was done using V-band luminosity instead of stellar mass, so that each spaxel has the same total luminosity. This is more similar to what an observer would do. The luminosity values of each particle were calculated using a stellar population synthesis model (Bruzual and Charlot, 2003). This allows us to calculate the luminosity of each stellar particle in a given band, based on its metallicity and age (and mass). The kinematic maps reach out to a radius of $4R_e$. This is in the upper limit of what observations can achieve (e.g., Cappellari et al., 2015), and ensures that we sample parts of the galaxy where the dark matter starts dominating.

The second ingredient necessary for using the Jeans equations is the surface brightness
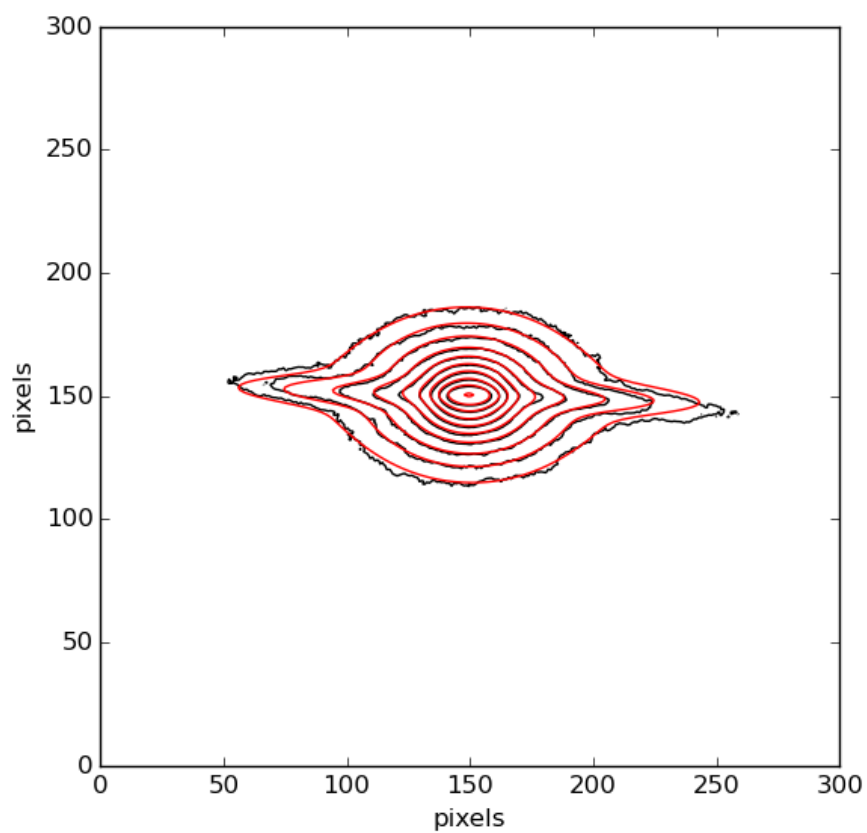
Figure 5.1: Comparison of the true isophotes (black lines) of one of our galaxies, 0227 *NoAGN*, with the isophotes derived with the Multi-Gaussian Expansion method (red lines).

of our kinematic tracer (stellar particles). Similarly to observations, we characterized the stellar surface brightness using the Multi-Gaussian Expansion code (MGE, Cappellari (2002)), which represents the luminosity distribution of a galaxy with a sum of 2D Gaussian functions with varying normalizations, dispersions, and flattenings. Figure 5.1 shows an example of a galaxy's true isophotes (black lines) compared with the corresponding MGE isophotes, showing a good fit. The luminosity of the stars, which we used as input for the MGE, was calculated in the V band using the Bruzual and Charlot (2003) stellar population synthesis model.

5.1.2   Mass models

JAM models need an assumption on the shape of the gravitational potential, and therefore of the mass distribution. The two most common choices are to assume that the mass distribution follows the light one and that the mass distribution can be represented by a power-law (e.g., Cappellari et al., 2013a). In the first case one needs to deproject the 2D luminosity distribution obtained from MGE, which can be done in a spherically symmetric way with this formula (Cappellari et al., 2013a):

$$M(r) = (M/L)_\star \cdot \sum_k L_k \left(\mathrm{erf}(h_k) - 2\,h_k \exp(-h_k^2)/\sqrt{\pi} \right) \tag{5.3}$$

$$h_k \equiv r/\sqrt{2}\sigma_k q_k^{1/3},$$

where the sum is done over the MGE Gaussians, erf is the error function and q_k is the intrinsic axial ratio of the Gaussian, from Eq. 2.23. $(M/L)_\star$ is the only free parameter of the model. Mass models can be much more complex, including a central SMBH mass and two different anisotropy values in the inner and outer parts of the galaxy, in addition to MGE and power-law components (Cappellari et al., 2015).

In this work we parametrized the potential with two different mass models. The first one is a generalized Navarro et al. (1997) (gNFW) profile:

$$\rho_{\mathrm{PL}}(r) = \rho_0 \left(\frac{r}{r_{\mathrm{break}}} \right)^{-\gamma} \left(1 + \frac{r}{r_{\mathrm{break}}} \right)^{\gamma-3}, \tag{5.4}$$

where r_{break} is set to $20\,\mathrm{kpc}$ and ρ_0 and α are free parameters. Throughout the Chapter it will be labeled as *PL* (power-law). The second type of mass model we considered is:

$$\rho_{\mathrm{MGE+PL}}(r) = (M/L)_\star \cdot L_{\mathrm{MGE}}(r) + \rho_{0,\mathrm{DM}} \left(\frac{r}{r_{\mathrm{break}}} \right)^{-\gamma} \left(1 + \frac{r}{r_{\mathrm{break}}} \right)^{\gamma-3} \tag{5.5}$$

where $L_{\mathrm{MGE}}(r)$ is the deprojected surface brightness from the Multi-Gaussian Expansion code (Cappellari, 2002), and represents the luminous matter, while the following gNFW profile is used to represent the dark matter. This model will be labelled *MGE+PL* throughout the Chapter. In this case there are three free parameters instead of two: the mass-to-light ratio and the normalisation and slope of the gNFW profile. In both models the anisotropy β_z and the inclination i also appear as free parameters, for a total of four parameters in the *PL* model and five in the *MGE+PL* one.

5.1.3 Parameter optimization

The quantity that the JAM models actually try to reproduce is the root mean squared velocity V_{rms}:

$$V_{\mathrm{rms}} = \sqrt{V_{\mathrm{avg}}^2 + \sigma^2}\,. \qquad (5.6)$$

In order to find the parameters that produce the best fitting V_{rms} map we ran a Markov Chain Monte Carlo (MCMC) algorithm, using the EMCEE code (Foreman-Mackey et al., 2013). This codes needs a prior function P(model) and a likelihood function P(data—model). We used a flat prior distribution, in the sense that the within the parameter boundaries we give the parameters have the same prior likelihood. For most of the parameters we picked very large boundaries, with the exception of the inclination, the range of which is limited by the MGE deprojection (see Eq. 2.23):

$$\arccos(q_{min}) \cdot \frac{180}{\pi} < i\,[\text{degrees}] < 90\,, \qquad (5.7)$$

where q_{min} is the axis ratio of the flattest MGE Gaussian. The likelihood function which evaluates how good is a set of parameters is given by:

$$P(\text{data}|\text{model}) = \exp\left(-\frac{\chi^2}{2}\right) \qquad (5.8)$$

with

$$\chi^2 = \sum_{\text{spaxels}} \left(\frac{V_{\mathrm{rms}}^{input} - V_{\mathrm{rms}}^{model}}{\varepsilon_{V_{\mathrm{rms}}}}\right)^2\,, \qquad (5.9)$$

where V_{rms}^{input} is the root mean squared velocity from the simulation and V_{rms}^{model} the one from the JAM dynamical model with the given set of parameters. $\varepsilon_{V_{\mathrm{rms}}}$ is the error on the measurements of V_{rms}^{input}, which we assume to be constant. The probability of a set of parameters being the right ones is then given by $P(model|data) = P(data|model) \cdot P(model)$.

5.1.4 A typical example of a JAM fit

In general the fits work to reasonable accuracies, but some galaxies stand out, either on the positive or negative side. Galaxy 0227 *NoAGN* is a particularly interesting example because it is challenging to model, with its multiple components with different kinematics and stellar population properties. It is not the best fit we obtained, nor the worst, but perhaps the one that has the most to tell us. Figures 5.2 and 5.3 show the comparison of the input V_{rms} with the one from *PL* and *MGE+PL* JAM models respectively. The V_{rms} map has a 'butterfly' shape, with higher values along the midplane where the net rotation is fastest; this is typical of fast rotators. The two models reproduce the V_{rms} map quite well, but they have slightly lower values of V_{rms} along the midplane and slightly higher values above and below. The *MGE+PL* model does slightly better, and also has a dip in

V_{rms} the very center, which is also in the input map, but does not appear in the PL map. In Figure 5.4 we compare the density profile of our example galaxy (red dots) with the density profile of the best fitting PL model. The real density profile flattens in the central region due to the gravitational softening (0.2 kpc, dashed line in the Figure), which does not allow the formation of highly dense cusps. This happens in all our simulations. The PL model cannot represent this core, and as a result the best fitting density profile has a shallower slope compared to the real slope for $r > 1kpc$. Despite this, the fit works well and is reasonably accurate for $r > 0.5kpc$ and especially beyond 2 kpc.

The $MGE+PL$ model works better in the core, since the light distribution is also flattened, but comes with its own set of problems. Most notably the stellar M/L ratio is not constant with radius. Figure 5.5 shows the comparison between the real and model density profiles. We also separated the stellar (MGE) and dark matter (power-law) components real (model) density profile in yellow and black respectively. The central regions contain more young stars, which shine brighter, making the model overestimate the mass within 0.8 kpc by a factor of ~ 2. Instead the density profile between 0.8 and 3 kpc is slightly underestimated. Remarkably, the power-law component perfectly fits the dark matter profile (except for the flattened region within 1 kpc, once again the effect of the softening length: 0.45 kpc for dark matter particles).

In Figures 5.6 and 5.7 we show the posterior distributions from the MCMC analysis for the PL and $MGE+PL$ models respectively. In both models the best fitting inclination is the lowest possible value allowed by the MGE deprojection; in this case 78.83 degrees, which is very close to the real value (80). In both models the best fitting anisotropy is negative, around $\beta_z = -0.25$, which makes sense given that the galaxy is a fast rotator; the real value is however smaller in absolute value: $\beta_z = -0.06$. This could be caused by the fact that the stars of the fast-rotating disk component are also brighter. In the PL model the density profile normalization ρ_0 and the slope γ are degenerate, as would be expected (higher normalization and lower slope can result in the same total mass). In the $MGE+PL$ model there is a weaker degeneracy between the power-law parameters, but also between them and the stellar mass-to-light ratio $(M/L)_\star$, as all of them contribute to the total mass.

5.1.5   Results for the whole sample

So far we looked at a single galaxy model, but now we would like to see how well the JAM models fare in our whole sample. In Figure 5.8 we compare the total mass-to-light ratio calculated from JAM $((M/L)_{\mathrm{JAM}})$ with the real one $((M/L)_{\mathrm{real}})$, both computed within the effective radius R_{e}. $(M/L)_{\mathrm{JAM}}$ is the model mass divided by the deprojected MGE luminosity (Eq. 5.3 without multiplying by $(M/L)_\star$), both within R_{e}. The grey dashed line is given by $(M/L)_{\mathrm{JAM}}=(M/L)_{\mathrm{real}}$. The recovery of the mass-to-light ratio is generally accurate. The PL values (red dots) tend to slightly underestimate the real M/L. This is probably caused by the problem of fitting the kinematics in the central region, where the density profile is flat. The $MGE+PL$ values (green dots) are instead very accurate.

In Figure 5.9 we compare the best-fitting anisotropy β_z with the corresponding real val-
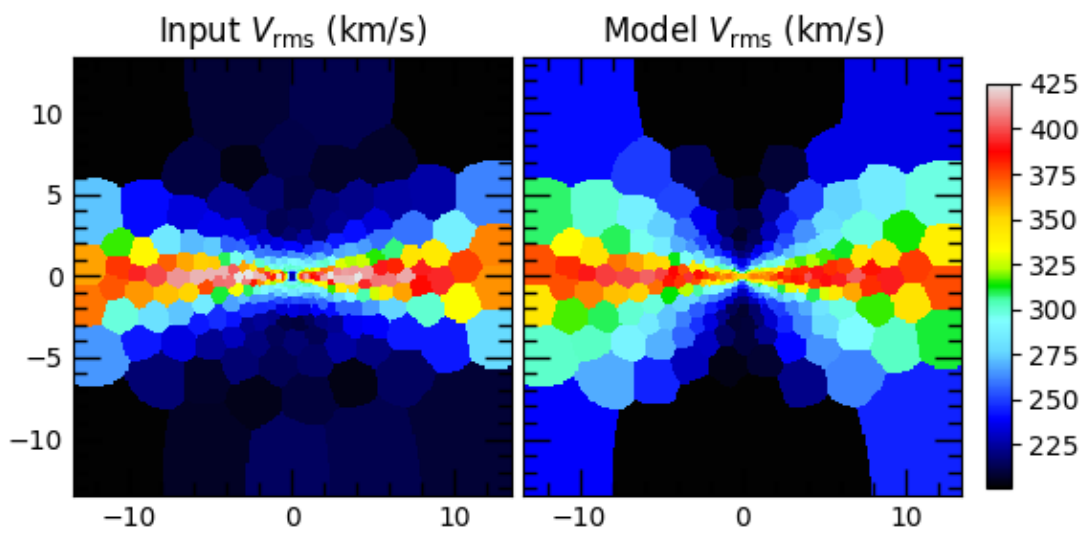
Figure 5.2: V_{rms} map of galaxy 0227 *NoAGN* compared with its best-fitting *PL* JAM model.
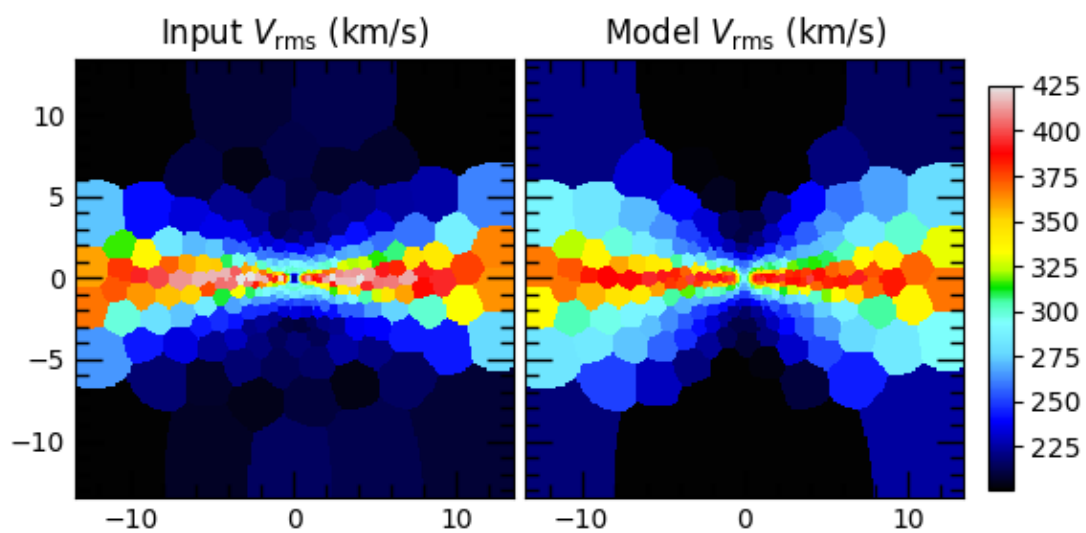
Figure 5.3: $V_{\rm rms}$ map of galaxy 0227 *NoAGN* compared with its best-fitting *MGE+PL* JAM model.
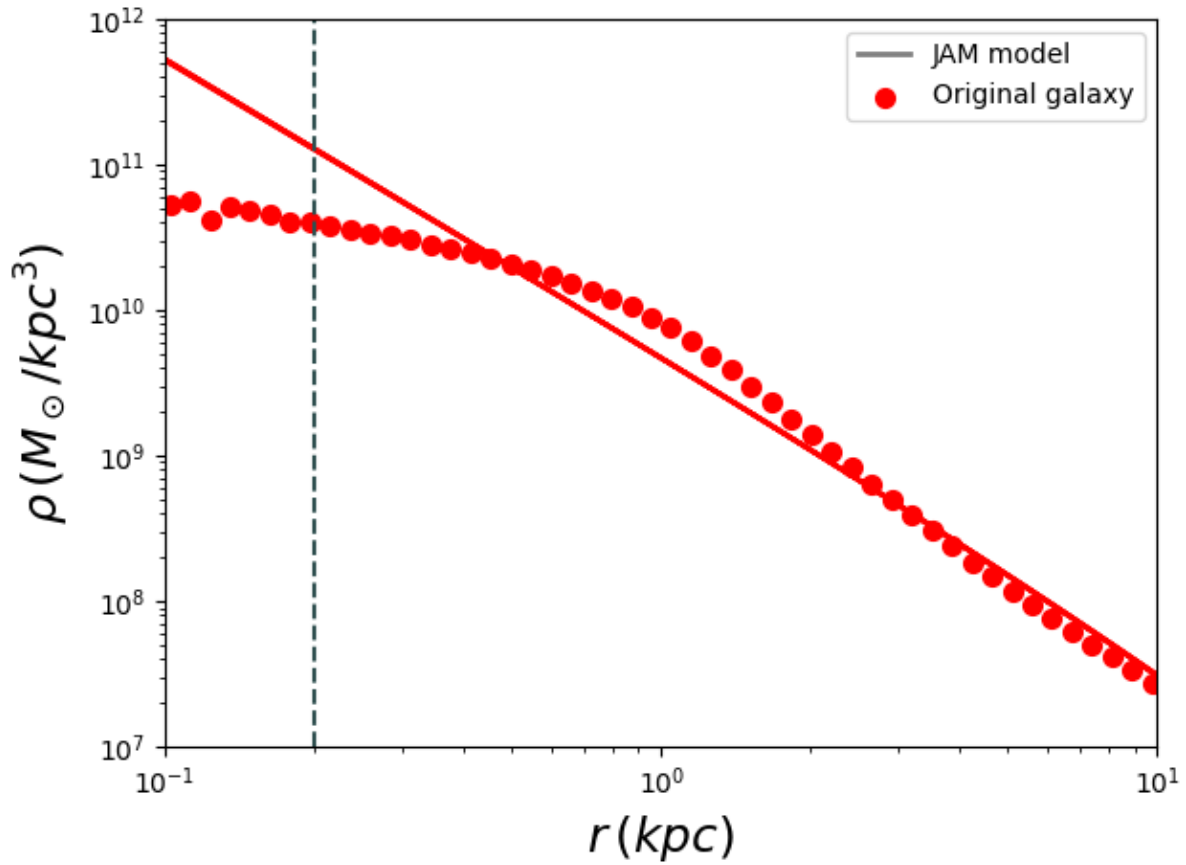
Figure 5.4: Comparison of the total density profile of galaxy 0227 *NoAGN* (red dots) with the reconstructed *PL* profile from dynamical modelling (red line). The profile slope is skewed to shallower values because of the central core.
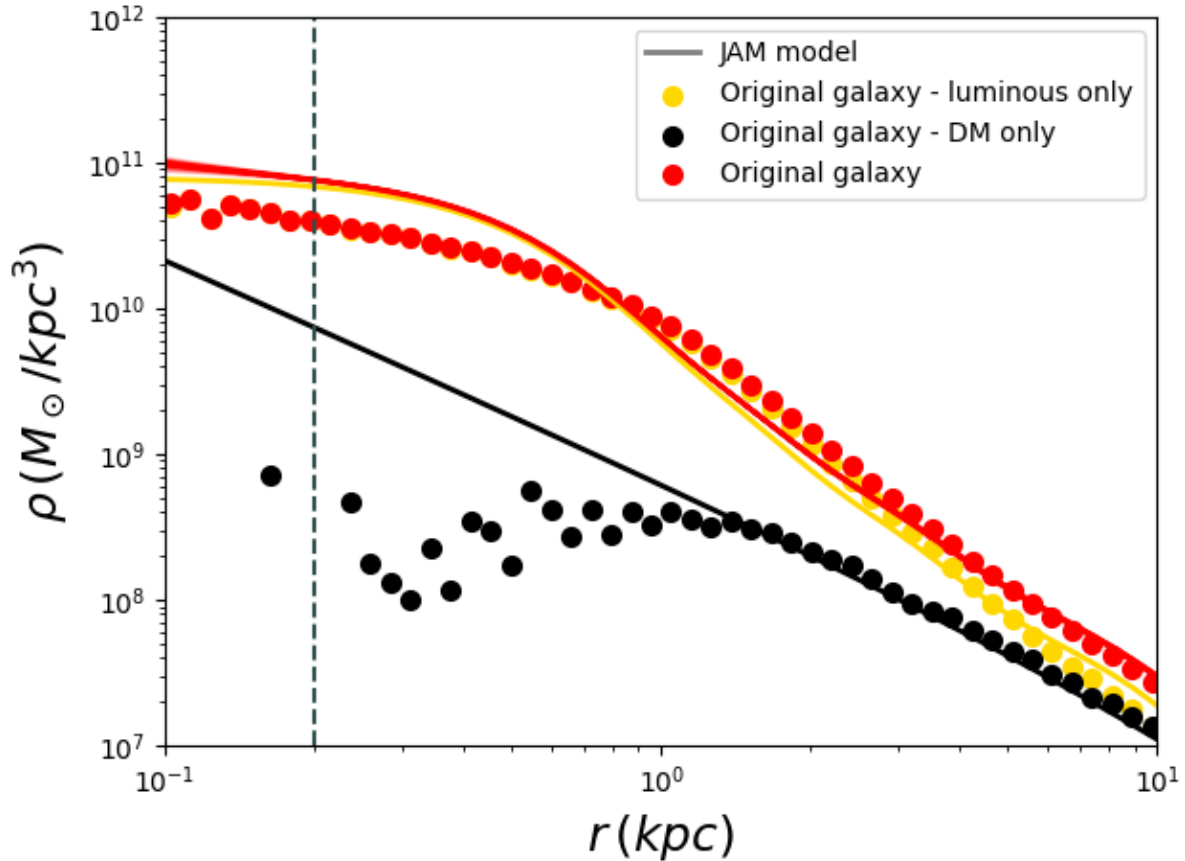
Figure 5.5: Comparison of the total density profile of galaxy 0227 *NoAGN* (red dots) with the reconstructed *MGE+PL* profile from dynamical modelling (red line). We also distinguish the stellar and dark matter components of the galaxy (yellow and black dots) and show the MGE and PL components of the model separately (yellow and black lines). The MGE component fails to represent accurately the luminous mass in the center because of the varying stellar M/L, which our model assumes to be constant. The PL component manages to recover the dark matter density profile correctly.
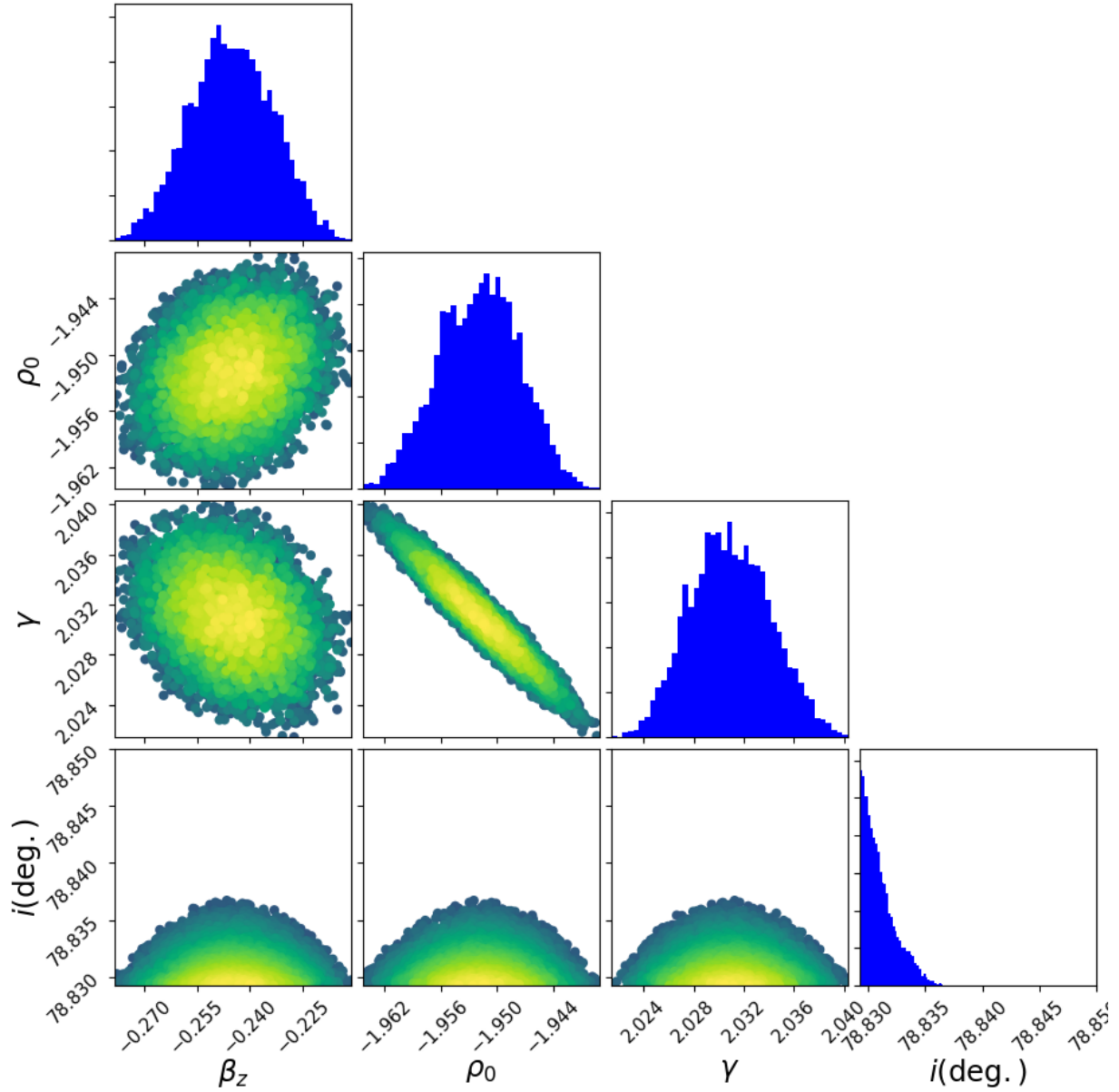
Figure 5.6: Posterior distribution of the MCMC run for the *PL* model of galaxy 0227 *NoAGN*. The parameters are the anisotropy β_z, density profile normalization ρ_0 and slope γ and inclination i. The distribution is color-coded by likelihood, so that the brighter points represent parameter sets that better fit the input V_{rms}. There is degeneracy between the two parameters of the mass model, ρ_0 and γ .
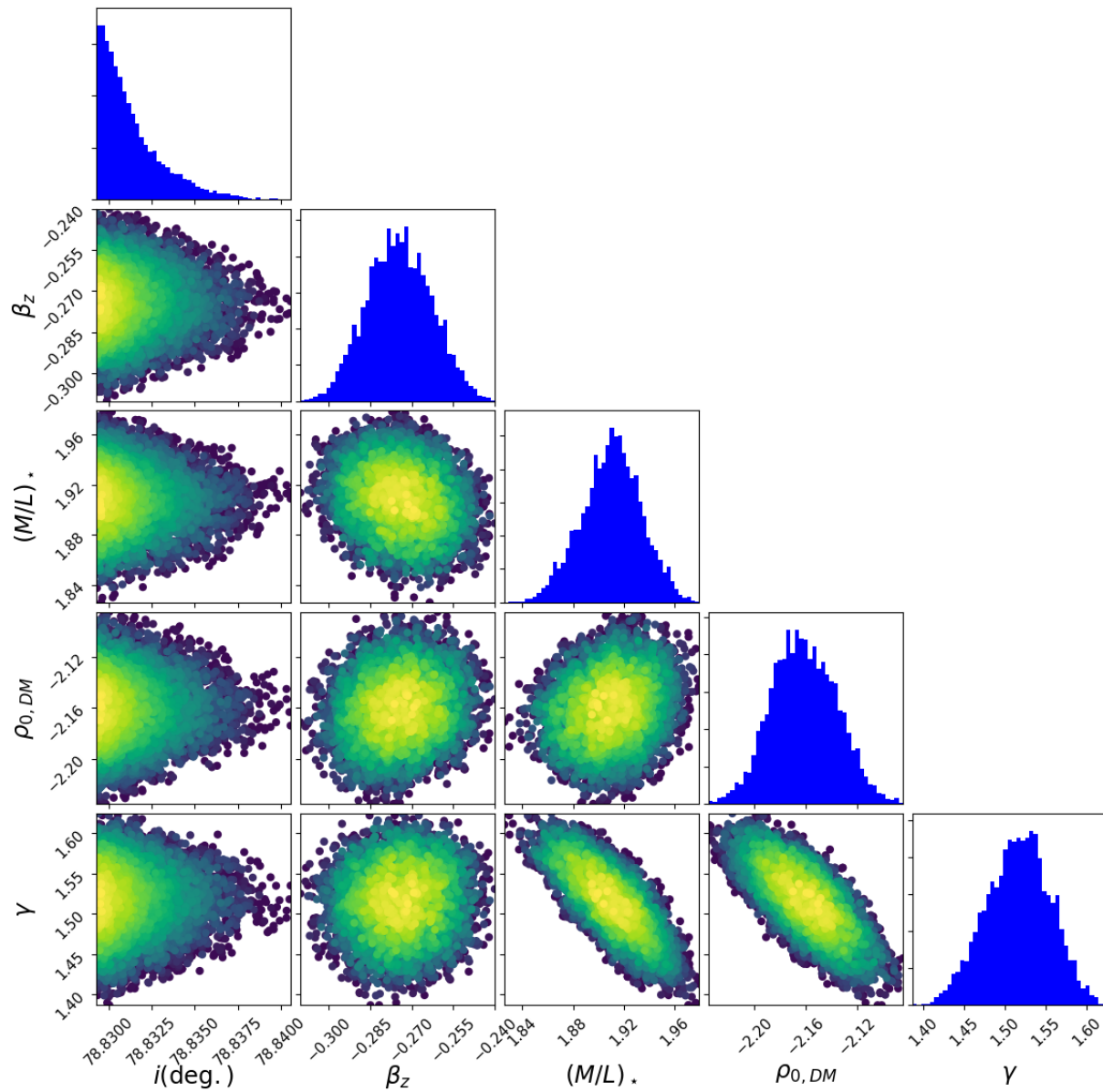
Figure 5.7: Posterior distribution of the MCMC run for the *PL* model of galaxy 0227 *NoAGN*. The parameters are inclination i, anisotropy β_z, stellar $(M/L)_\star$, density profile normalization ρ_0 and slope γ_{DM}. They distribution is color-coded by likelihood, so that the brighter points represent parameter sets that better fit the input V_{rms}. There is a weak degeneracy between the three parameters of the mass model, $(M/L)_\star$, ρ_0 and γ_{DM}.

ues. The real values were computed by calculating the velocity dispersions in cylindrical coordinates within the radial range of the kinematics ($4\,R_{\mathrm{e}}$). In this case the correlation between JAM values and real values is very weak, for both the *PL* and *MGE+PL* models. This generally tells us that a simple axisymmetric Jeans model with constant anisotropy is not adequate for representing the kinematics of our simulated galaxies, even though the density profile estimations work well enough. Observed fast-rotators are espected to not have cored density profiles and to have a more homogeneous structure, making the values recovered from them more accurate.

Figure 5.10 shows the recovered galaxy inclination from the JAM models as a function of the galaxy ellipticity, calculated as a weighted average of the flattenings of the MGE Gaussians. The grey dashed line shows the real value of the inclination (80 degrees). We find that for most of our galaxies the best fitting inclination is edge-on (90 degrees). Only for galaxies with larger ellipticity than $\sim 0.3 - 0.4$ the recovery is more accurate. The *MGE+PL* values are slightly more likely to be accurate.

Finally, in Figure 5.11 we show the dark matter fractions within sphere of radius R_{e} as a function of stellar mass of the galaxy. The blue circles represent the values computed directly from the simulations, while the green circles represent the values computed from JAM (*MGE+PL*) modelling. We also show the values corresponding to the galaxies from the ATLAS^{3D} sample (Cappellari et al., 2013a; Cappellari et al., 2013b). For our JAM values, we used the real stellar mass within R_{e} to compute the dark matter fraction, as if the exact stellar mass-to-light ratio was known, so that all the uncertainty is given by the dynamical modelling. In other words the JAM dark matter fractions presented here are given by $f_{DM}^{JAM} = (M_{tot}^{JAM} - M_{\star}^{real})/M_{tot}^{JAM}$. The dark matter fractions of our galaxies within the effective radius vary from 5% to 30%. Our JAM estimates cover more or less the same range, and no systematic bias seems to be present. In a few cases the dark matter fraction is severely underestimated; e.g. 0616 *NoAGN* has f_{DM} =10%, but the JAM estimate is 1%. The measured dark matter fractions of ATLAS^{3D} galaxies range from 0% to 35%, which is similar to our sample of simulations, despite them having generally lower mass. Using gravitational lensing, Barnabè et al. (2011) found dark matter fractions around 60% in more massive systems. Other simulations also disagree. The Magneticum simulations found similar values to ours (Remus et al., 2017), but in the Illustris TNG simulation dark matter fractions of 50% or more are common for galaxies in our mass range (Lovell et al., 2018). Part of these differences could be attributed to different definitions of the effective radius, inside which the dark matter fraction is measured (projected or three-dimensional, using stellar luminosity or stellar mass,...). They could however also be caused by the differences between the simulation codes used to run these simulations, in particular by their feedback implementations.

5.1.6   Effect of AGN feedback

So far we grouped together *AGN* and *NoAGN* simulations, but now we would like to see if one of the two groups is better represented by JAM models. Figure 5.12 shows the ratio between recovered and real total mass-to-light ratios for the *MGE+PL* model as a function
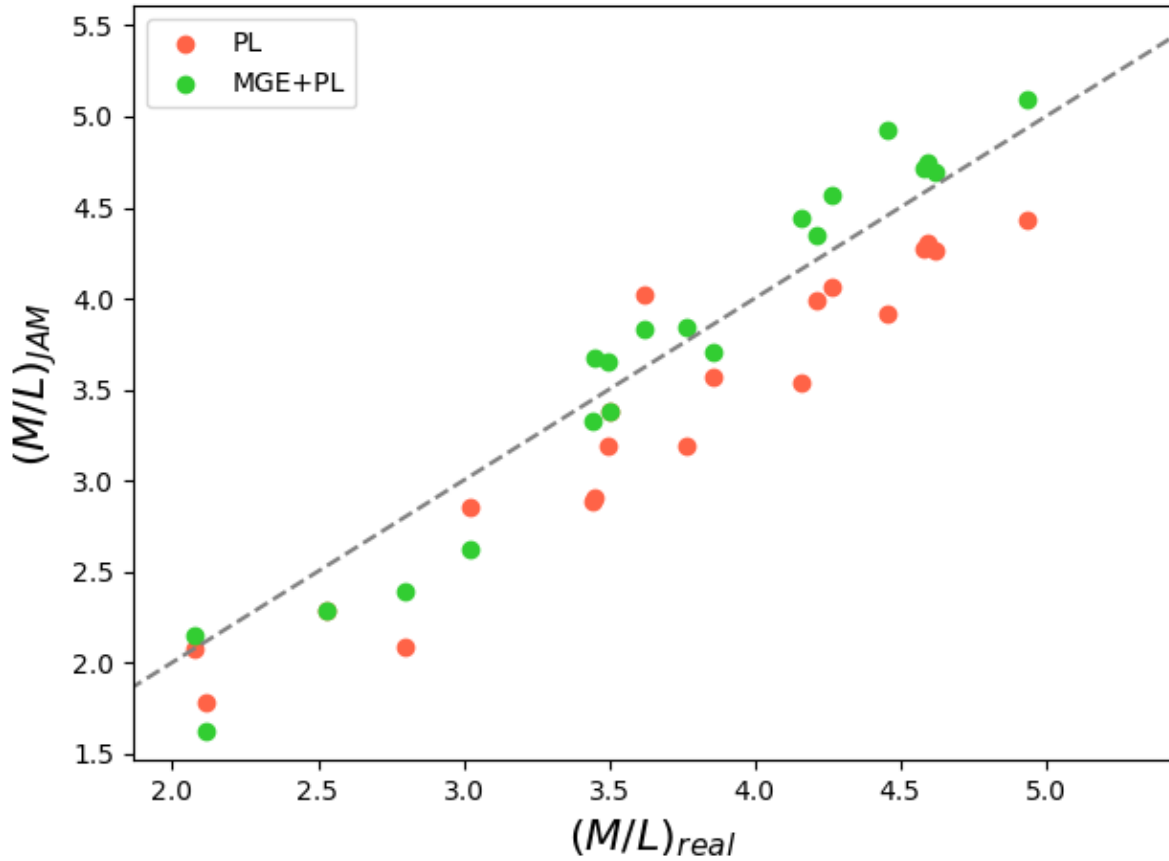
Figure 5.8: Comparison of the total M/L of our galaxy sample (both *AGN* and *NoAGN*) compared with the values derived from JAM modelling, with the *PL* model (red dots) and with the *MGE+PL* model (green dots). The grey dashed line is given by $(M/L)_{\rm JAM} = (M/L)_{\rm real}$. The recovered M/L values are generally quite accurate, especially for the *MGE+PL* model. The *PL* model tends to underestimate them.
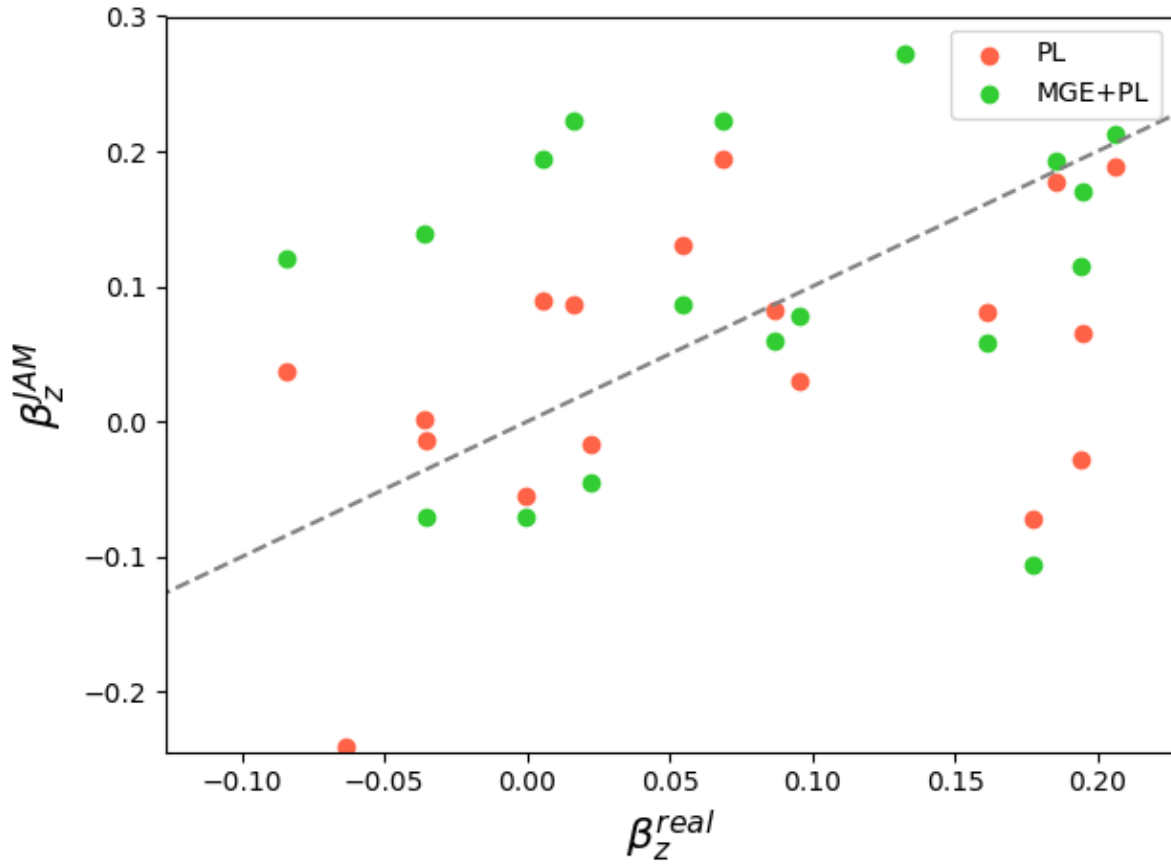
Figure 5.9: Comparison of β_z of our galaxy sample compared with the values from JAM modelling, with the *PL* model (red dots) and with the *MGE+PL* model (green dots). The grey dashed line is given by $\beta_z^{\text{JAM}} = \beta_z^{\text{real}}$. The real anisotropy values are generally not recovered correctly.
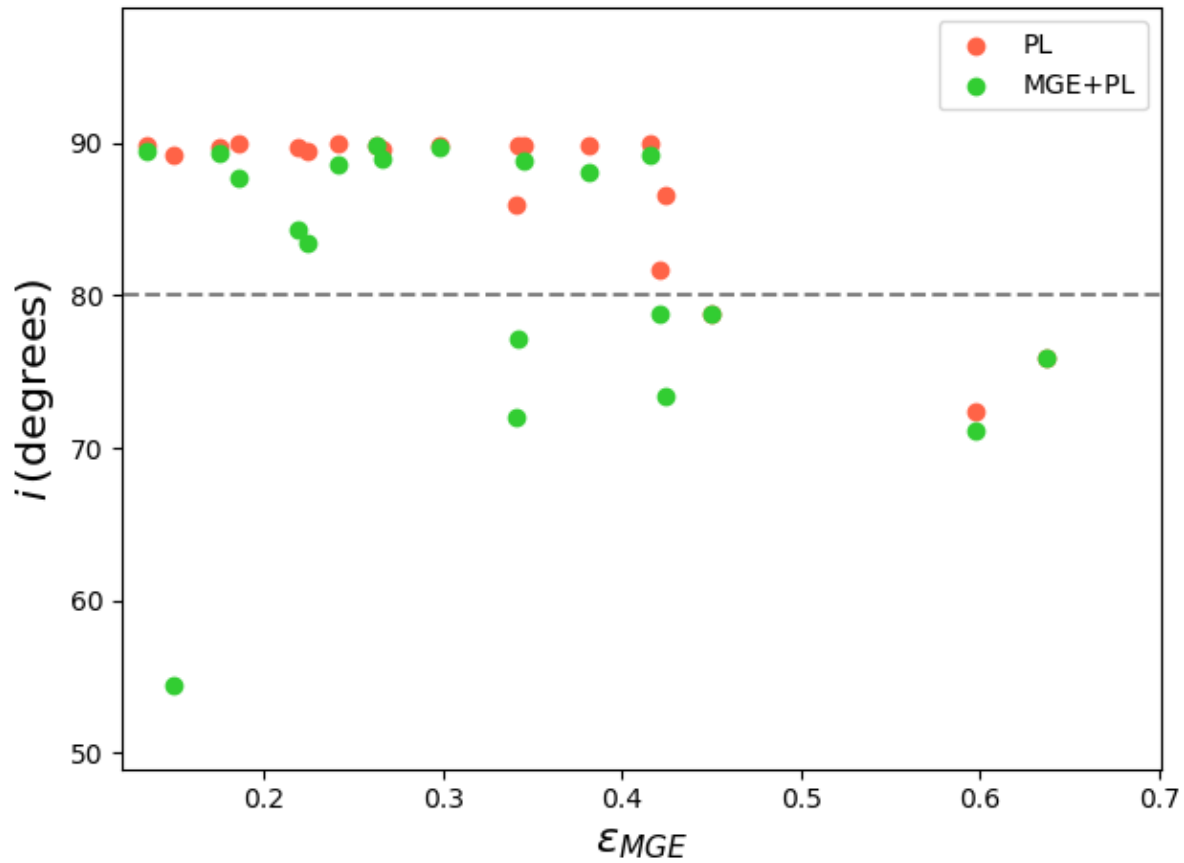
Figure 5.10: Recovered inclination from our JAM models as a function of the ellipticity recovered from MGE (ε_{MGE}). The real inclination of all our galaxies is 80 degrees (dashed grey line). In most cases the JAM models recover 90 degrees (edge-on) as inclination, especially at low ellipticity. The inclination is more accurate for $\varepsilon_{MGE} > 0.4$.
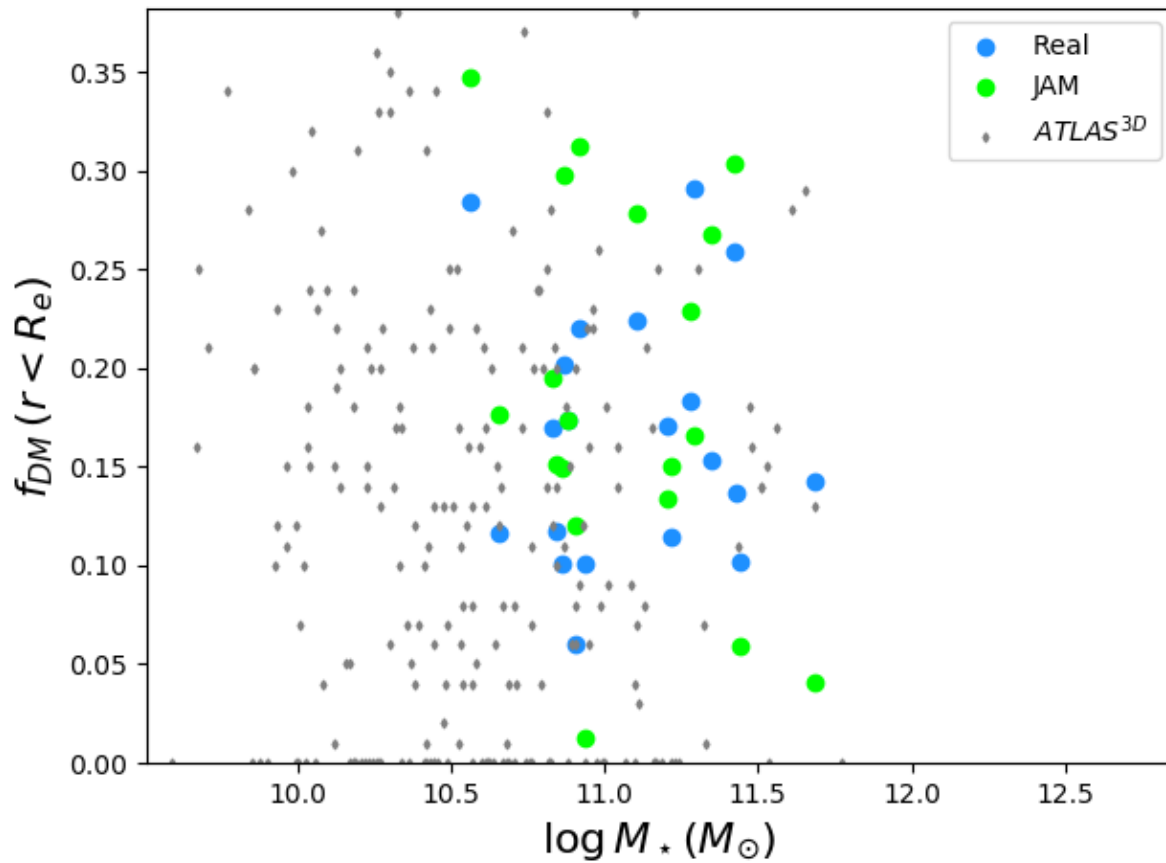
Figure 5.11: Dark matter fraction within a sphere of radius R_e as a function of stellar mass. The blue circles indicate the real values from our simulations, while the green circles the value from $MGE+PL$ JAM modelling (assuming that the correct stellar mass is known). The grey dots represent galaxies from the $ATLAS^{3D}$ sample (Cappellari et al., 2013a; Cappellari et al., 2013b).

of the angular momentum parameter λ_R. The orange markers are the values for the AGN simulations, while the blue markers represent the $NoAGN$ ones. The different marker shapes indicate different initial conditions. We find that generally the AGN simulations are easier to model. There are mainly two reasons for this. The $NoAGN$ simulations are more likely to include young in-situ-formed stars, which as previously discussed can produce variable M/L ratios (e.g. 0204 $NoAGN$ 0227 $NoAGN$). Furthermore, they can be made of many kinematic components: for instance 0175 $NoAGN$ has two rotating components with a 90 degree inclination between them, and 0616 $NoAGN$ has two counter-rotating components. The AGN counterparts have simpler kinematics. Faster-rotating galaxies generally have simpler kinematics, so one would expect the M/L recovery to be more accurate for higher λ_R values, but that is not really the case in our sample. This could simply be because of the small sample size.

In Figure 5.13 we compare the density profile slope derived from the JAM PL model with the one of the real density profile. In the latter case the slope is calculated with a linear regression within the interval $2\,\mathrm{kpc} < r < 10\,\mathrm{kpc}$. First of all looking at the distribution of the real slope γ_{real} we see that there AGN does not have a clear impact on the distribution within our sample. Large cosmological simulations found instead that galaxies simulated without AGN feedback should have steeper profiles (Remus et al., 2017; Peirani et al., 2019). Interestingly the measured slopes with the PL models are shallower for $NoAGN$ galaxies. This is however caused by the previously outlined problem of the flattened density profile in the central region. Because of this the measured γ is always lower than the real one. The reason why AGN galaxies are less affected is that they have a super-massive black hole in the center, which steepens the best-fitting slope.

In Figure 5.14 we do the same thing for the $MGE+PL$ model. Since in this case the slope is not a parameter of the model, we did a linear regression of the model density profile in the $2\,\mathrm{kpc} < r < 10\,\mathrm{kpc}$ range. In this case the profile slopes match better, but there are many outliers. Generally the AGN galaxies seem to result in better fits. One of the galaxies, 0664 AGN has a best-fitting slope of $\gamma = 3.6$ and was not included in the Figure.

5.2 Gravitational lensing

5.2.1 Lensing formalism

Gravitational lensing can be used to reconstruct a galaxy's density profile as well. Here we will briefly cover its basic equations. A more thorough presentation can be found in Chapter 1 of Schneider et al., 2006. If two galaxies are aligned on the line of sight, the image of the background galaxy (the source) gets deformed by the gravitational potential of the foreground galaxy (the lens), as predicted by general relativity (Einstein, 1916). Assuming that the lens potential is 'thin' compared to the size of the system (thin lens approximation), this deformation can be described in simple terms. The point $\vec{\theta}$ on the
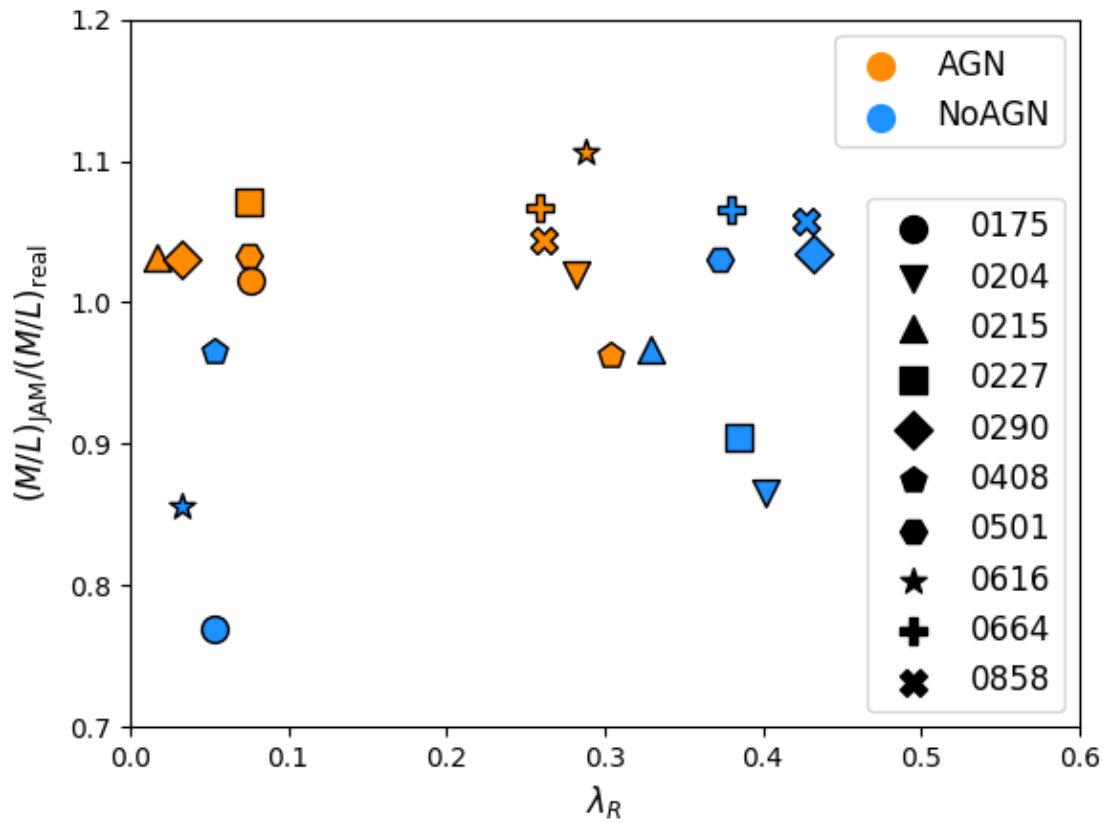
Figure 5.12: Error in the recovery of the total M/L (ratio between JAM *MGE+PL* and real values) as a function of λ_R for our sample. For most galaxies the recovery is accurate, but in some M/L is underestimated. These tend to belong to the *NoAGN* sample. There is no clear trend with λ_R.
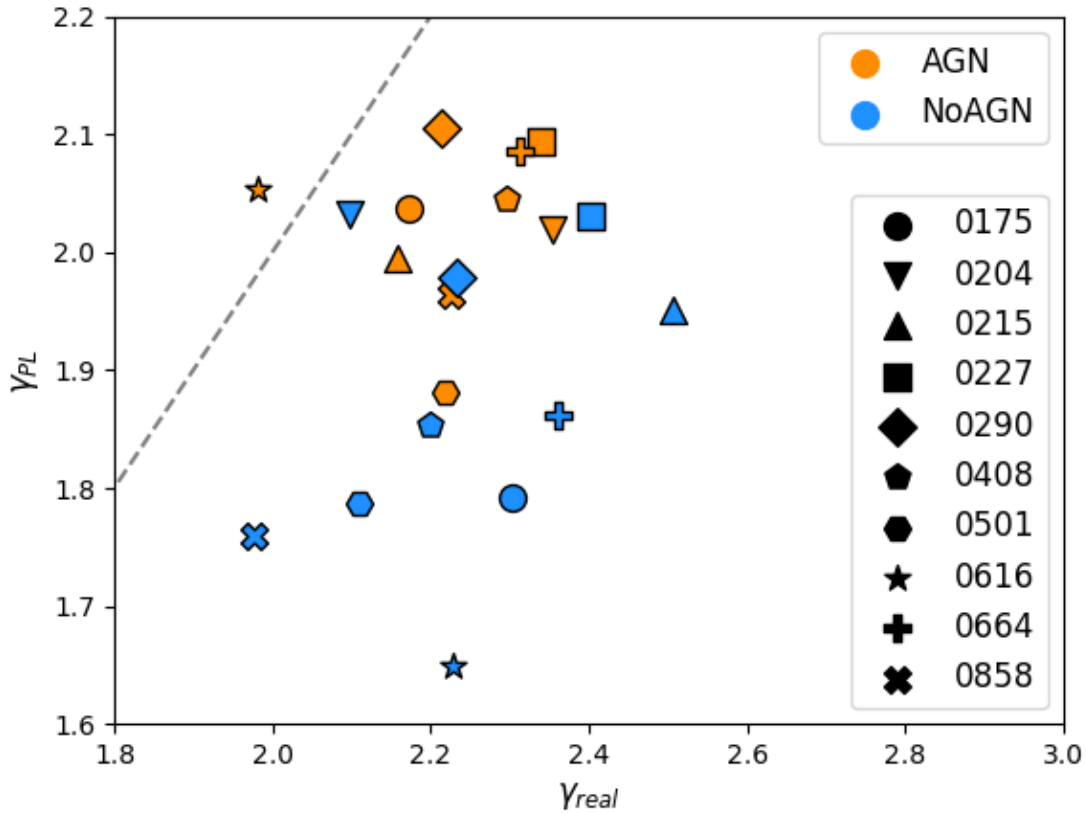
Figure 5.13: Density profile slope derived from *PL* JAM modelling of our whole sample as a function of the best linear fit of the real density profile. The grey dashed line is given by $\gamma_{\mathrm{PL}} = \gamma_{\mathrm{real}}$. Galaxies without AGN feedback tend to have shallower measured density profiles, but this is likely caused by the flat cores in the density profile (see Figure 5.4). The real density slopes cover more or less the same distribution: we see no effect of AGN feedback.
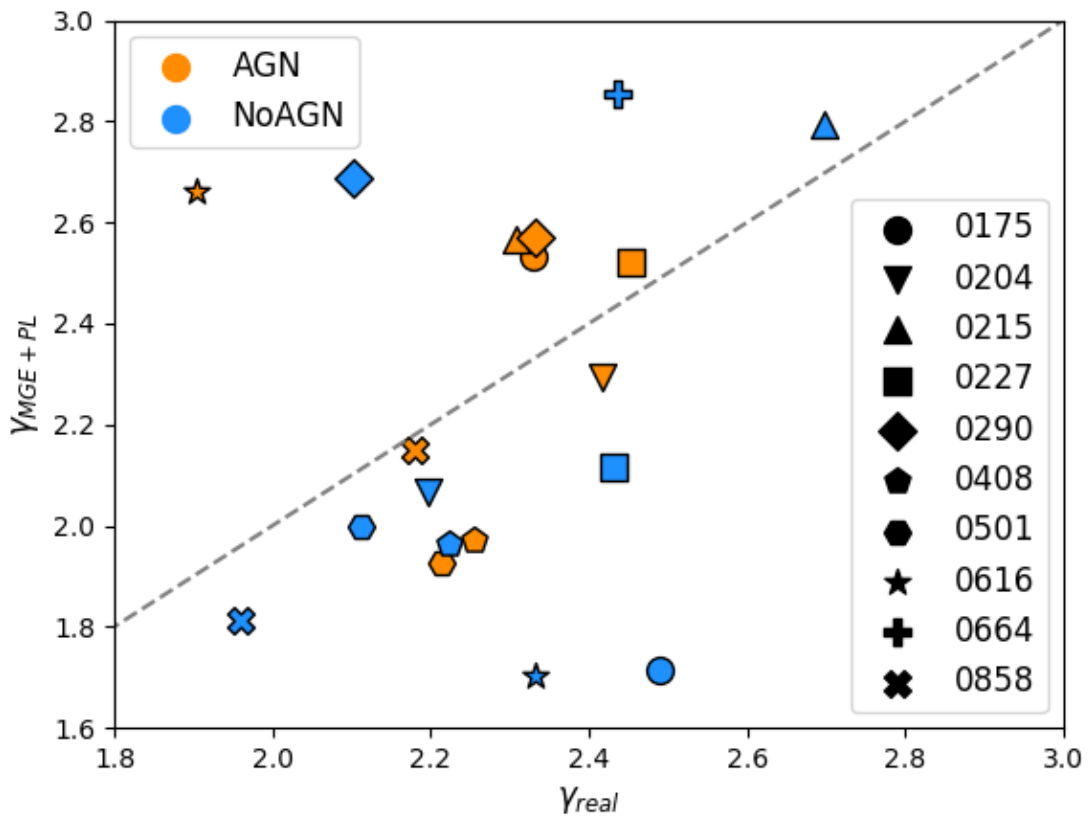
Figure 5.14: Density profile slope derived from *MGE+PL* JAM modelling of our whole sample as a function of the best linear fit of the real density profile. The grey dashed line is given by $\gamma_{\mathrm{MGE+PL}} = \gamma_{\mathrm{real}}$.

source plane gets deflected by $\vec{\alpha}$ on the lens plane according to:

$$\vec{\alpha}(\vec{\theta}) = \frac{1}{\pi} \int d^2\theta' \kappa(\vec{\theta'}) \frac{\vec{\theta} - \vec{\theta'}}{|\vec{\theta} - \vec{\theta'}|^2} , \tag{5.10}$$

where κ is the convergence, an adimensional measure of the projected surface mass density distribution of the lens. If Σ is the surface mass density, κ is defined as:

$$\kappa(\vec{\theta}) = \frac{\Sigma(D_L \vec{\theta})}{\Sigma_{cr}} , \tag{5.11}$$

where Σ_{cr} is the critical surface density:

$$\Sigma_{cr} = \frac{c^2}{4\pi G} \frac{D_S}{D_{LS} D_L} , \tag{5.12}$$

and D_L, D_S and D_{LS} are respectively the angular diameter distances from viewer to lens, from viewer to source and from lens to source. If we rescale the Newtonian potential and project it along the line of sight we get the lensing potential:

$$\Psi = \frac{D_{LS} D_L}{D_S} \frac{2}{c^2} \int \Phi(D_L \vec{\theta}, z) dz \tag{5.13}$$

The deflection angle α and convergence κ are then connected to the lensing potential by:

$$\vec{\alpha}(\vec{\theta}) = \vec{\nabla}\Psi(\vec{\theta}) \tag{5.14}$$

$$\kappa(\vec{\theta}) = \frac{1}{2}\nabla^2\Psi(\vec{\theta}) . \tag{5.15}$$

The full transformation from coordinates in the source plane $\vec{\theta}$ to the coordinates in the lens plane $\vec{\beta} = \vec{\theta} - \alpha(\vec{\theta})$ is then given by the lensing Jacobian:

$$A_{ij} = \frac{\partial\beta_i}{\partial\theta_j} = \delta_{ij} - \frac{\partial\alpha_i}{\partial\theta_j} = \delta_{ij} - \frac{\partial^2\Psi}{\partial\theta_i\theta_j} \tag{5.16}$$

which can be written in matrix form as:

$$A = (1 - \kappa) \begin{pmatrix} 1 & 0 \\ 0 & 1 \end{pmatrix} + \gamma \begin{pmatrix} cos2\phi & \sin 2\phi \\ \sin 2\phi & -\cos 2\phi \end{pmatrix} , \tag{5.17}$$

where ϕ is the angle between α and the x axis and γ is known as the shear. Equation 5.17 then tells us that an image on the source plane gets transformed in two ways: it gets amplified by the κ term and its shape gets distorted by the γ term.

In the special case where the lens potential is that of a point mass, the solution is simple. In an image lies at $\vec{\theta_S}$ in the source plane, in the lens plane it will lie in:

$$\vec{\theta} = \vec{\theta_S} + \frac{D_{LS}}{D_S}\alpha(\vec{\theta}) = \vec{\theta_S} + \frac{\theta^2_{einst}}{|\theta|} , \tag{5.18}$$

where θ_{einst} is the Einstein radius:

$$\theta_{einst} = \sqrt{\frac{4\,G\,M}{c^2}\frac{D_{LS}}{D_L\,D_S}}\,. \tag{5.19}$$

If the observer, lens and source are aligned, then the source image will form a ring around the lens of angular diameter $2\,\theta_{einst}$, known as Einstein ring. In spatial units, the Einstein radius at the lens is $R_{\mathrm{einst}} = D_L\,\theta_{einst}$. This effect also happens if the source is close to radially symmetric, and is observed in real galaxies.

5.2.2 Constructing mock lensing images

In order to construct mock lensing images we employed a multiple-lens-plane ray-tracing code (Jain et al., 2000; Hilbert et al., 2009). This code has been used for simulating weak lensing effects in cosmological simulations, to compare with observations (Hilbert et al., 2009; Hilbert et al., 2012). In our case we use it to simulate strong lensing effects caused by the potential of one of our galaxy. We construct the lens system in the following way: the lens is positioned at $z = 0.2$ and oriented randomly. We used the corresponding snapshot of our simulation at that redshift (therefore its mass is different from the one of the JAM comparisons, for which we used $z = 0$ snapshots). The galaxy is cut at the virial radius, so there are no additional halos near the line-of-sight and the thin lens approximation is correct. As a source image we used a scaled-down picture of a nearby spiral galaxy (M51, Fig. 5.15). The source is positioned at $z = 0.7$. The lens and source are slightly misaligned, so that the lensed image is not a perfect Einstein ring. The potential used by the ray tracing code is a smoothed version of the particle potential of the simulated galaxy, smoothed according to a Gaussian with sigma equal to the softening length (0.2 kpc). The rays are 'shot' from the source, their trajectory gets deformed by the potential of the lens, and they reach the observer at different angles, producing a deformed image of the source. This image is then convoluted with a point spread function (PSF) and random noise is added to it, to make it look more like a real observed lensed galaxy. Figure 5.16 shows a summary of our sample of lensed galaxies. The source image is always the same, and so are the lens-source and observer-lens distances; only the lens potential changes. Since source, lens and observer are almost aligned the lensed images have a ring-like shape, and the size of the ring is the Einstein radius. Larger images mean that the lens mass is larger.

5.2.3 Reconstructing the lensed source image

Once the mock observational lensed image is constructed, we apply the code by Vegetti and Koopmans (2009) to reconstruct the source image and in the process obtain the mass of the lens galaxy. This code has been employed in many lensing papers, e.g. for detecting dark matter substructures (Vegetti et al., 2012; Vegetti et al., 2014). It uses adaptive grids to transform the image on the lens plane to the corresponding reconstructed image on the source plane for a given model potential. The lensing potential is modelled as an elliptical
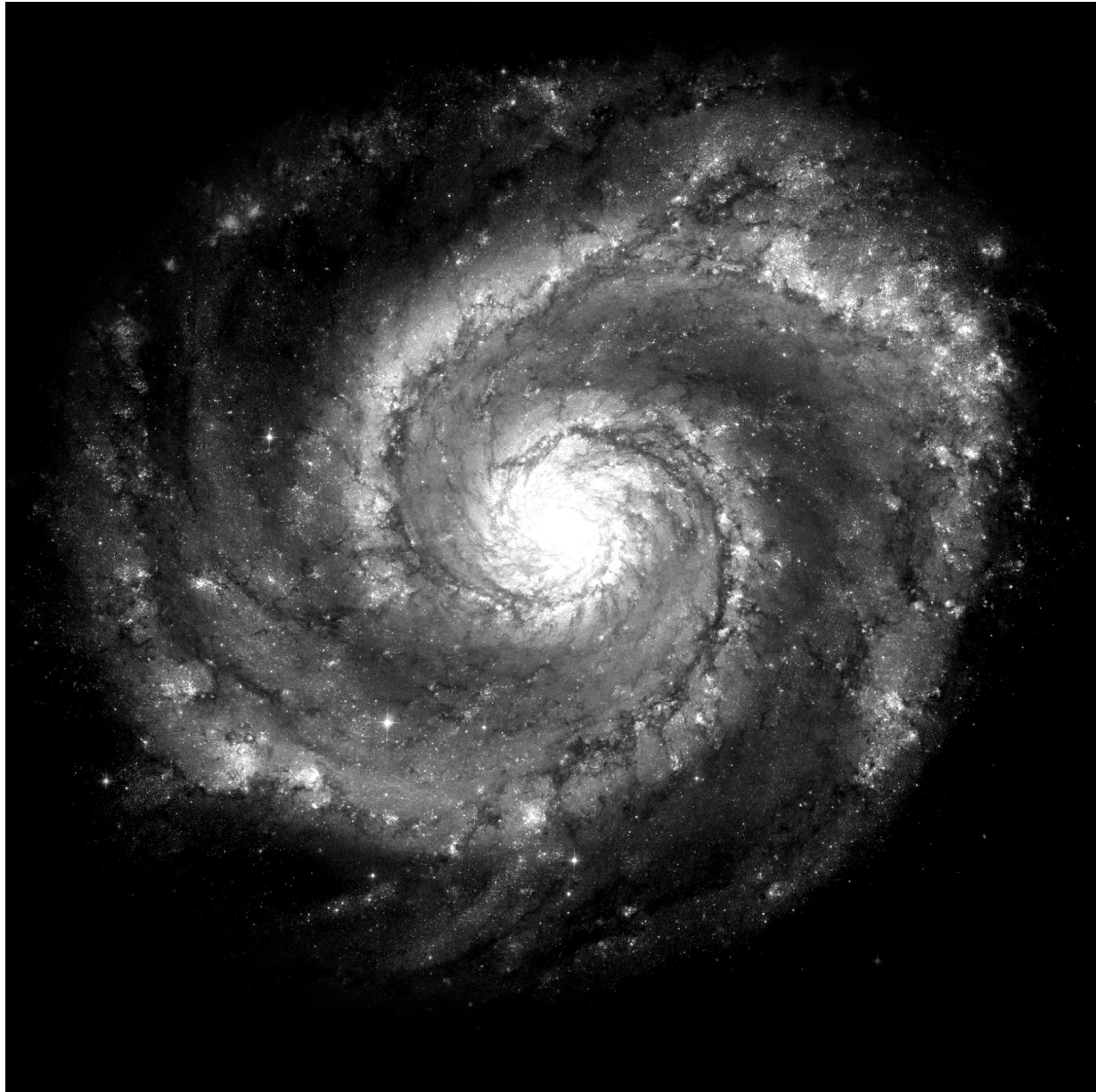
Figure 5.15: The picture used as source galaxy in our analysis. The picture was taken by the Hubble Space Telescope and depicts M51, the Whirlpool Galaxy (without its companion galaxy).
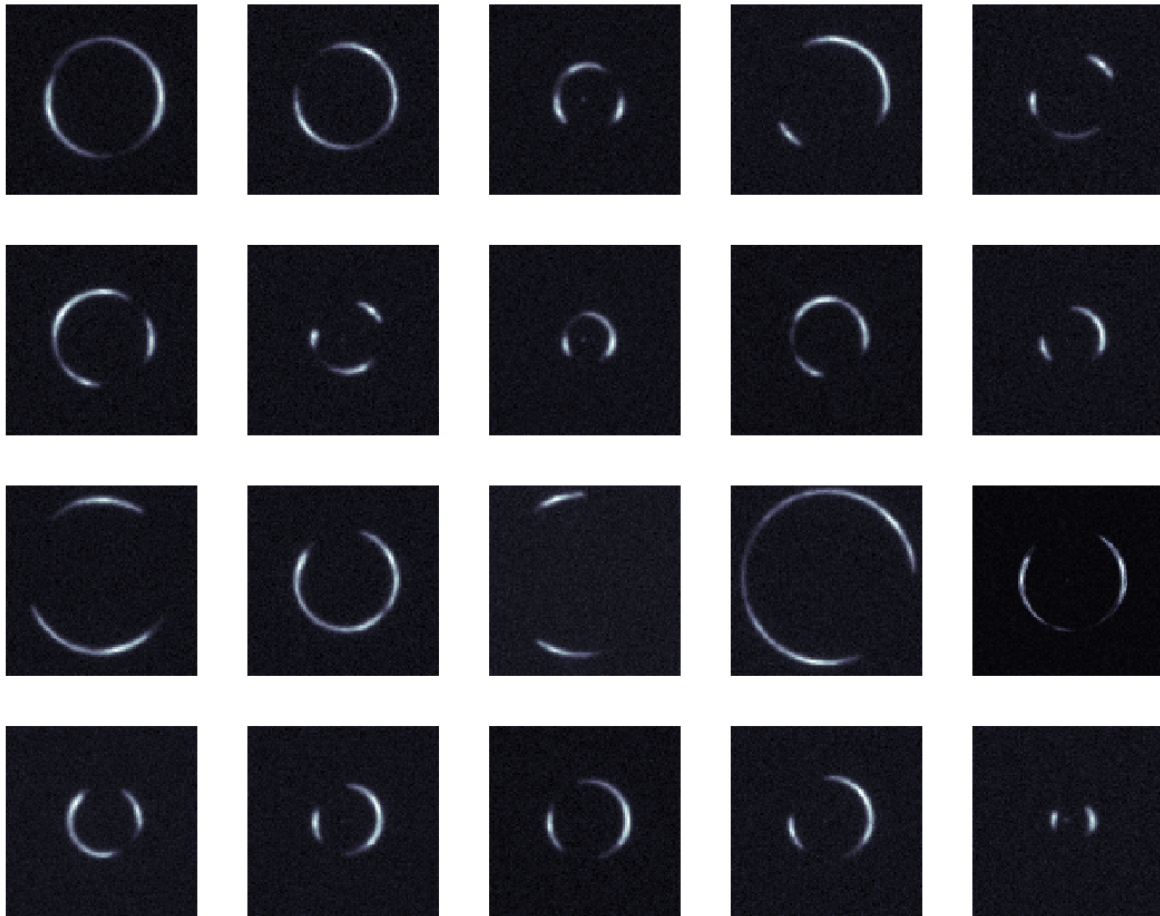
Figure 5.16: Our sample of simulated lenses. Each image is constructed using one of our zoom simulations as lens, and Fig. 5.15 as source, and then adding noise to mock observational figures.

power-law, with free normalization κ_0, slope γ, axial ratio q and orientation with respect to the x axis. The x and y positions of the center of the potential in the plane of the sky (x_0, y_0) are also free parameters. If for simplicity we assume that the major axis is aligned with the x axis, the lens convergence is:

$$\kappa(x,y) = \kappa_0 \, \frac{2 - \gamma/2}{2} q^{\gamma - 3/2} \, \left(q^2 \, (x - x_0)^2 + (y - y_0)^2\right)^{-\frac{\gamma - 1}{2}} \, . \tag{5.20}$$

γ is the equivalent three-dimensional density profile slope. The parameter actually used in the code is the projected slope, $\gamma - 1/2$. The normalisation of the power-law κ_0 is related to the Einstein radius by (Vegetti et al., 2014):

$$\theta_{Einst} = \left(\frac{2 - \gamma/2}{3 - \gamma} \, \kappa_0 \, q^{\frac{\gamma - 2}{2}}\right)^{\frac{1}{\gamma - 1}} \, . \tag{5.21}$$

The code can also model the shear exerted by an external potential.

The complication of the reconstruction process is that the original source image is unknown, adding in principle a number of degrees of freedom equal to the number of pixels of the image. This is treated by applying a regularization to shape of the source, specifically to the surface brightness gradient. The code then optimizes the parameters of the lens potential and of the source regularization iteratively with a Bayesian approach, taking into account the noise and PSF, until the best-fitting set of parameters is found. The number of free parameters makes the modelling quite complicated, and at the time of writing this the results are still work in progress.

Figure 5.17 shows an example of the source reconstruction process using high resolution data (400 pixels per side, very little noise) from galaxy 0290 *NoAGN*. The first panel from the left shows the mock lensed image, the second panel shows the best fitting model, the third panel the residuals, and the fourth panel the reconstructed source (zoomed in). The model fits the data well. The residuals are larger in the region where the lensed source image lies, but they have a random pattern. They could be caused by details of the source image that the model does not capture. The reconstructed source looks realistic, and the spiral arms of the original image (Fig. 5.15) are clearly visible.

5.2.4   Density profile comparison

For our lensing analysis we used input images with a lower resolution, 100x100, closer to what has been done observationally with the SLACS survey (Bolton et al., 2006). In Figure 5.18 we compare the recovered surface density profile from lensing with the real profile of one of our galaxies (0290 *NoAGN* at $z = 0.2$). The real density profile is represented by the black dots, while the lensing estimate (a simple power-law) is shown as a green line. The real density profile is flattened in the central region due to softening (grey dashed line). Beyond 1 kpc it is close to isothermal ($\Sigma \propto R^{-1}$). The lensing estimate matches quite well the real profile, but it deviates in the central and outer regions. The slope of the reconstructed density profile matches the real slope at the Einstein radius R_{einst} where there is data available, but beyond 10kpc the density profile gets slightly steeper.
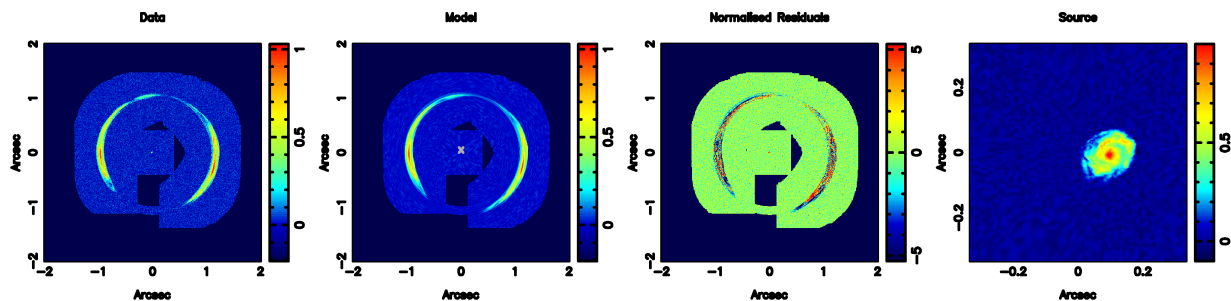
Figure 5.17: From left to right: input lensed image, model lensed image, residuals, reconstructed source. In this case the reconstruction was done with higher resolution than what is used elsewhere in this Chapter (400x400 instead of 100x100). The reconstructed source has visible spiral arms.
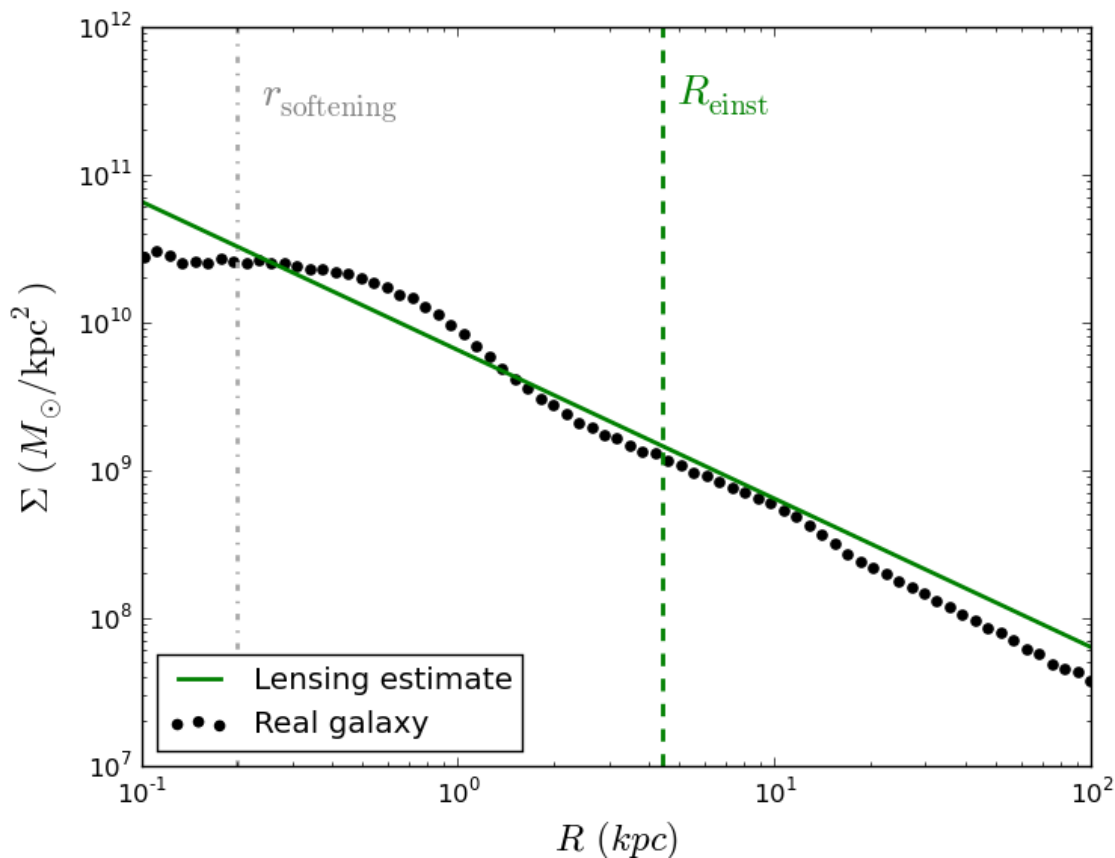
Figure 5.18: Comparison between the density profile recovered from gravitational lensing and the real one, for a simulated galaxy (0290 *NoAGN*). The grey dashed line shows the softening length, while the green dashed one shows the Einstein radius. The density profile slope at the Einstein radius is correctly recovered.
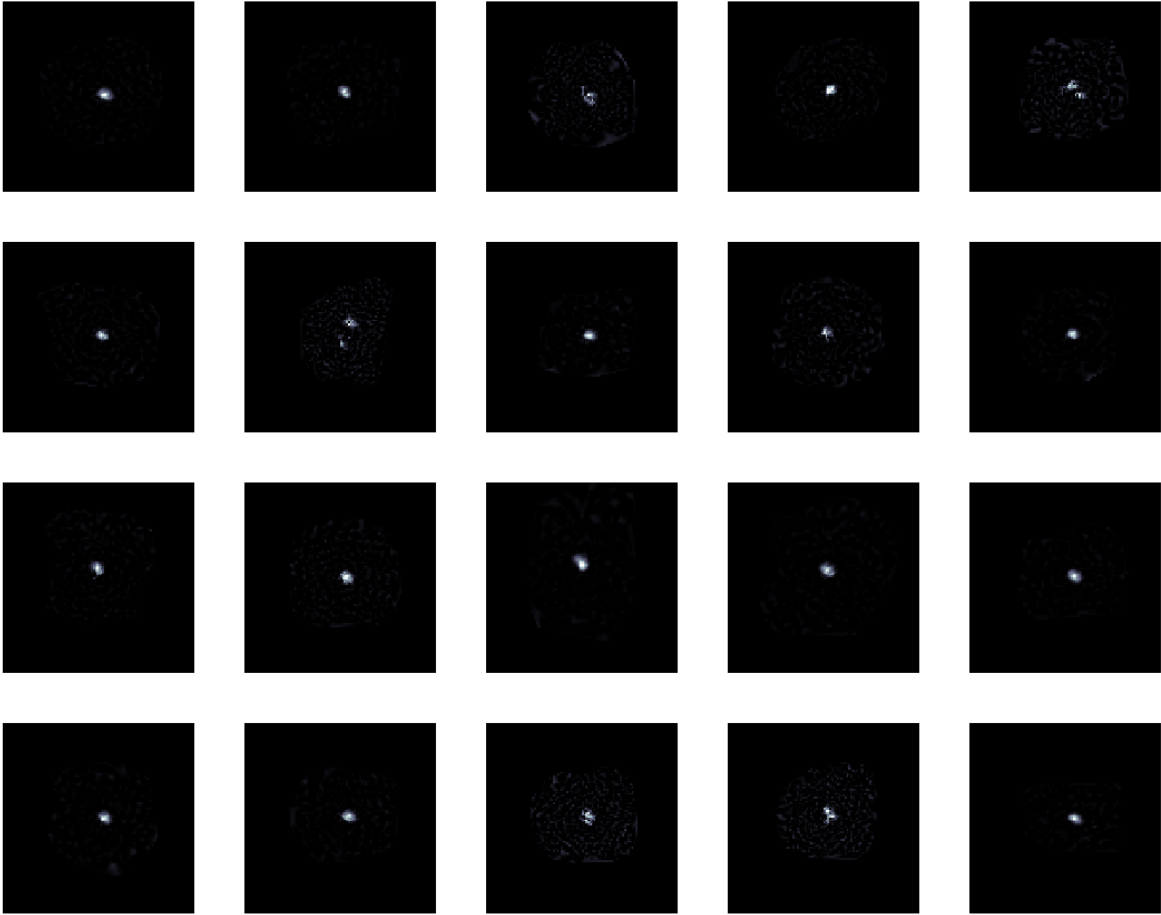
Figure 5.19: All the reconstructed source images for our sample. At this resolution we cannot see anything more than a blob.

5.2.5 Global comparison

In Figure 5.19 we show the reconstructed source images for all our galaxies, using 100x100 pixel input images. At this resolution the internal structure of the source galaxy cannot be resolved (unlike in Figure 5.17). With a few exceptions most reconstructions are correct. We compare how well the lens galaxy is modelled in Figure 5.20. It shows the total mass within the Einstein radius recovered from lensing as a function of the real value. For most galaxies the recovery is extremely accurate, even when the source reconstruction is not correct. There are two outliers, 0215 *NoAGN* and 0227 *NoAGN*, where the lensing value overestimates the real one ($3.77 \cdot 10^{11} \, M_{\odot}$ instead of $3.61 \cdot 10^{11} \, M_{\odot}$ and $4.22 \cdot 10^{11} \, M_{\odot}$ instead of $4.07 \cdot 10^{11} \, M_{\odot}$ respectively). Both of these galaxies have relatively high ellipticity and are seen almost edge-on, so it could be that the code struggled to find their correct flattening. More accurate modelling would probably solve this issue.
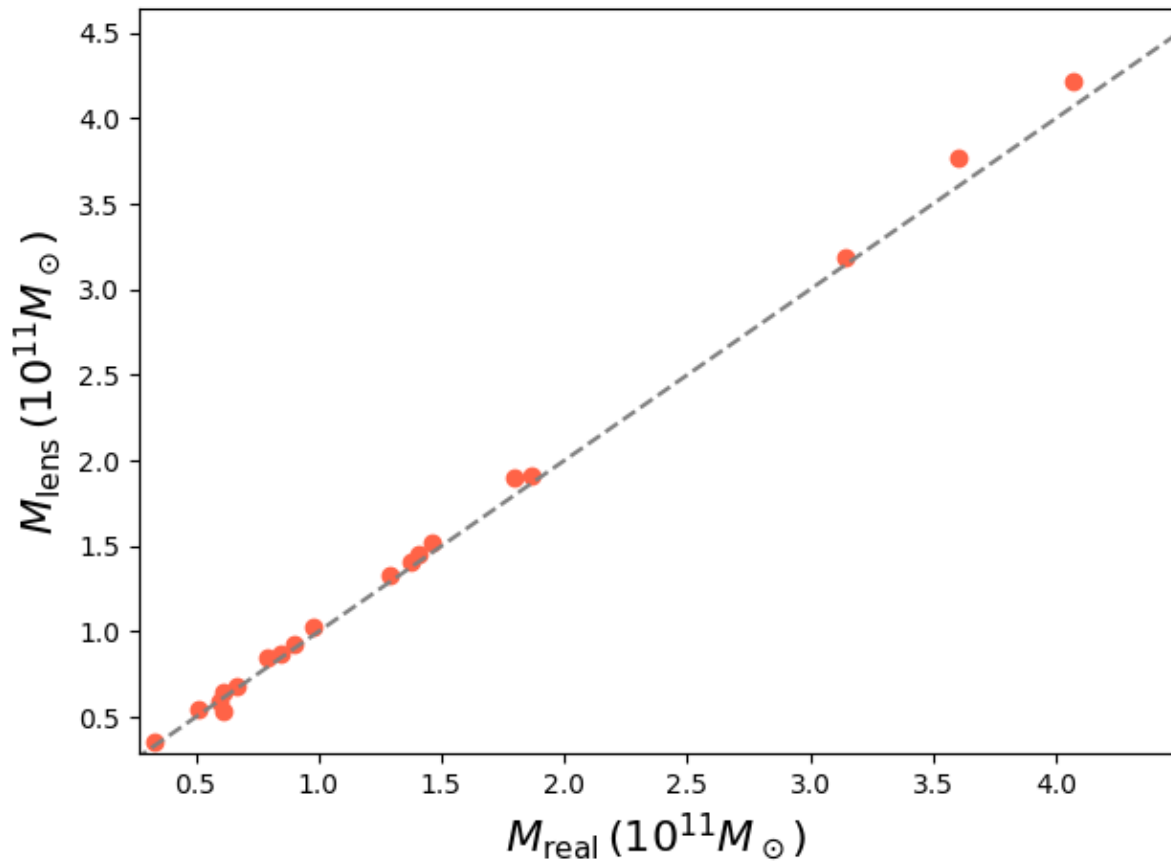
Figure 5.20: Comparison between the mass within R_{einst} recovered from gravitational lensing and the corresponding real value for the whole sample. The dashed grey line indicates $M_{lens} = M_{real}$. In most cases the estimate is very accurate.

5.3   Summary

In this Chapter we applied Jeans dynamical modelling and gravitational lensing to mock data from our cosmological simulations, trying to recover their mass and density profile. With the important caveat that our simulations might not be completely realistic, especially in the center, we found that:

- Jeans modelling can recover the M/L ratio of our simulated galaxies to good accuracy. Generally the *MGE+PL* model is slightly more accurate than the *PL* model in this. The accuracy in M/L recovery does not seem to depend strongly on other galactic properties (e.g., λ_R).

- In many of our galaxies the density profiles are correctly recovered in their entirety. In some cases the *MGE+PL* model even allows to measure the dark matter density profile correctly. This is however not always the case; in some of our galaxies varying stellar M/L ratios create degeneracies with the power-law component of the model.

- The anisotropy β_z recovered from Jeans modelling is generally inaccurate within our simulation sample, even when the density profile is correctly recovered and the model V_{rms} matches the observed one.

- The dark matter fractions of our galaxies range from 5 % to 30%. This is similar to the fractions measured in the ATLAS^{3D} survey and the ones from the Magneticum simulations (Remus et al., 2017), but much lower than what is found in Illustris TNG (Lovell et al., 2018).

- We succesfully constructed a pipeline for creating mock strong lensing images using our simulated galaxies as lenses, and then reconstructing the source images to recover the lens mass model. While the results are preliminary, we find that the accuracy of this mass estimation is very high, apart from a few cases where our automated pipeline failed. The density profile slope at the Einstein radius is also recovered to reasonable accuracy.

- We do not observe a strong impact of AGN feedback on the density profile slopes; a larger sample of simulated galaxies would be necessary to observe this effect.

Chapter 6

The dynamical impact of SMBHs on the orbital structure of merger remnants

In Chapter 4 we looked at how the energy feedback of accreting supermassive black holes can affect galaxies and particularly their stellar kinematics. SMBHs can however impact the structure and kinematics of galaxies even without feedback. During major mergers the central supermassive black holes of the two galaxies slowly spiral in towards the center of the merger remnant due to dynamical friction (Chandrasekhar, 1943), the gravitational drag caused by the surrounding stars and dark matter. In this process the stellar cusps that surround the SMBHs get destroyed due to violent relaxation. Even after the merger, the black hole binary in the center continues to kick out stars that orbit too close to it, a process known as 'scouring' (Hills and Fullerton, 1980). This effect removes stars from the inner parts of the galaxy, leaving a cored (flattened) density profile, which is indeed observed in many massive ellipticals (e.g. Thomas et al., 2016, Dullo et al., 2017). This is important, as otherwise there is no straight-forward way to 'dig' a flat core in an elliptical galaxy. Minor mergers do not affect the central regions of the main galaxy (Naab et al., 2009; Hilz et al., 2013; Frigo and Balcells, 2017), and gas infall would create a new stellar cusp (if there was no AGN feedback preventing it). Furthermore, this helps explain the many observed scaling relations between SMBH mass and other galaxy properties, as more massive black holes have a larger influence radius.

An interesting side effect of scouring by black holes is that if preferentially affects stars on radial orbits, as these stars pass closer to the black hole binary. This makes the orbit distribution in the inner region of the galaxy tangentially biased. The cored density profile and the tangential anisotropy have been observed together in massive elliptical galaxies (Thomas et al., 2016), further confirming this picture. Recently, simulations with accurate black hole dynamics showed that supermassive black holes can indeed produce both the core and the tangential bias (Rantala et al., 2018a). They also showed that the second effect does not happen if the black holes are merged as soon as they form a binary, confirming that it is caused by scouring.

In this Chapter I look more in detail at the orbital structure of merger remnants scoured by supermassive black holes. I do this by performing a full orbital analysis on a set of isolated, idealized simulations (presented in Chapter 3.3) of galaxy mergers with different black hole masses and different merger mass ratios. The orbital properties will also be compared to projected 2D kinematics and tridimensional shape, to understand what drives the trends in frequency of different orbit families, and whether there are observable features.

6.1   Properties of the simulated merger remnants

In this project we analyze a series of isolated simulations of galaxy mergers with supermassive black holes. These simulations have been described and studied in two published works, Rantala et al., 2018a and Rantala et al., 2018b. They were run with GADGET3 with the KETJU extension, which I described in Chapter 3.1.5. Using this extension is key, as it allows to accurately model at the same time the dynamics of the black holes and of the whole galaxy. In our simulations we used 11 different initial galaxy models different stellar and black hole masses; their properties are listed in Table 3.1.

6.1.1   Density profiles

The impact of the black holes on the density profiles and anisotropy of our simulations is described in detail in Rantala et al., 2018a, to which I contributed. The black holes create a flat core in the central part of the galaxy, the size of which is proportional to the black hole mass (see left panel of Figure 6.3). This mostly happens during the merger itself. Figures 6.1 and 6.2 show how the merger of the stellar cusps of the two progenitors takes place. The panels show the time evolution of stellar surface mass density maps of the M1-nobh (above) and M1-bh6 (below) simulations. The black holes rapidly fall to the center of the galaxy because of dynamical friction, making the merger of the stellar cusps happen earlier. While in the simulation without black holes the two cusps form a larger cusp, in the simulation with black holes the stars that surround them get ejected due to the interactions with the black holes. The black holes then form a binary, and continue to affect the surrounding stellar distribution. Stellar particles that wander too close to the black holes can exchange angular momentum with the binary and get kicked from the central part of the galaxy. This slowly decreases the central density further, but also affects the orbital structure of the core, as radial orbits are more likely to get close to the binary. This causes pushes the stellar anisotropy to negative values (right panel of Figure 6.3). These effects are more evident with larger black hole masses, as they correspond to larger influence radii.
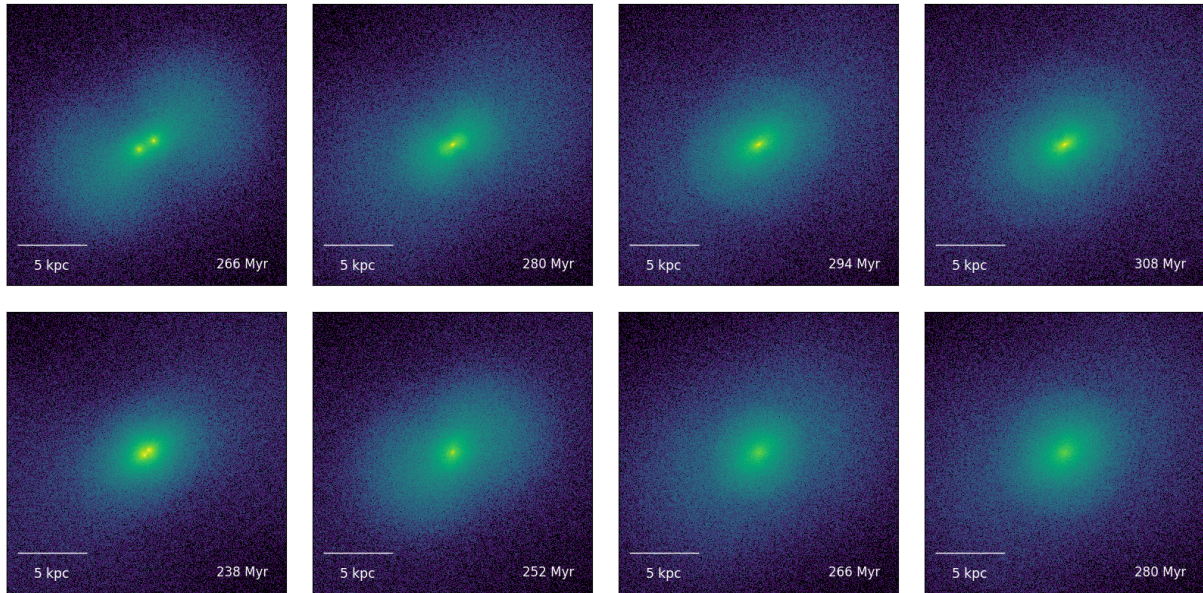
Figure 6.1: Surface mass density of stars in the M1-nobh (above) and M1-bh6 (below) simulations. The four panels from left to right indicate different snapshots in the simulation that show the effect of the merger. The spatial extent of each panel is 20kpc.
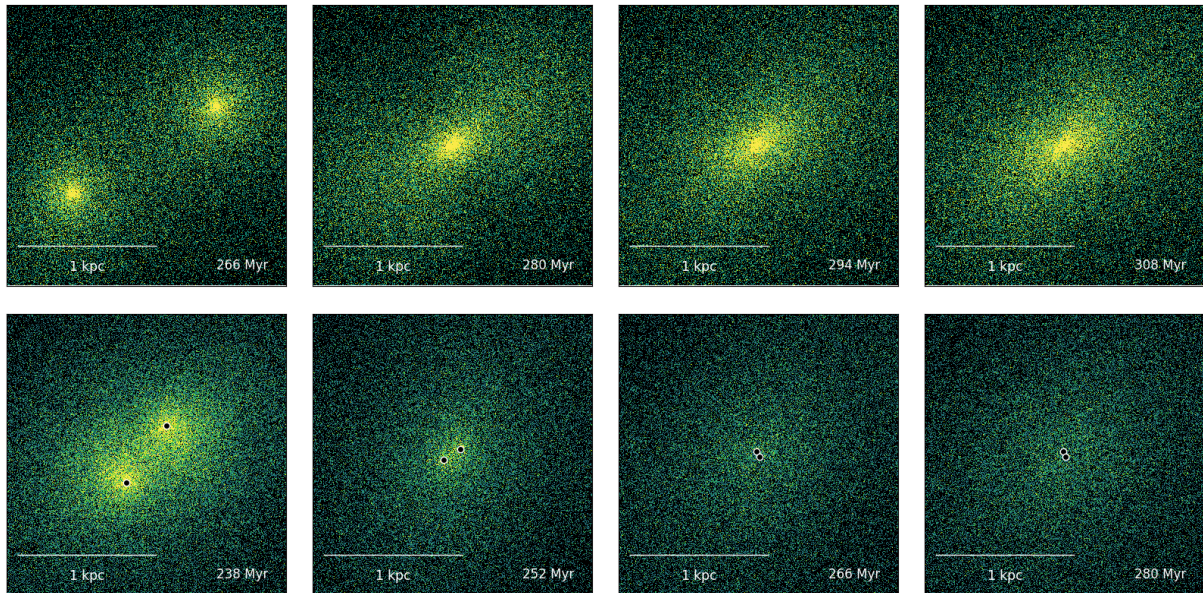
Figure 6.2: Same as Figure 6.1, but with a 2kpc extent. The black circles indicate the position of the two black holes.
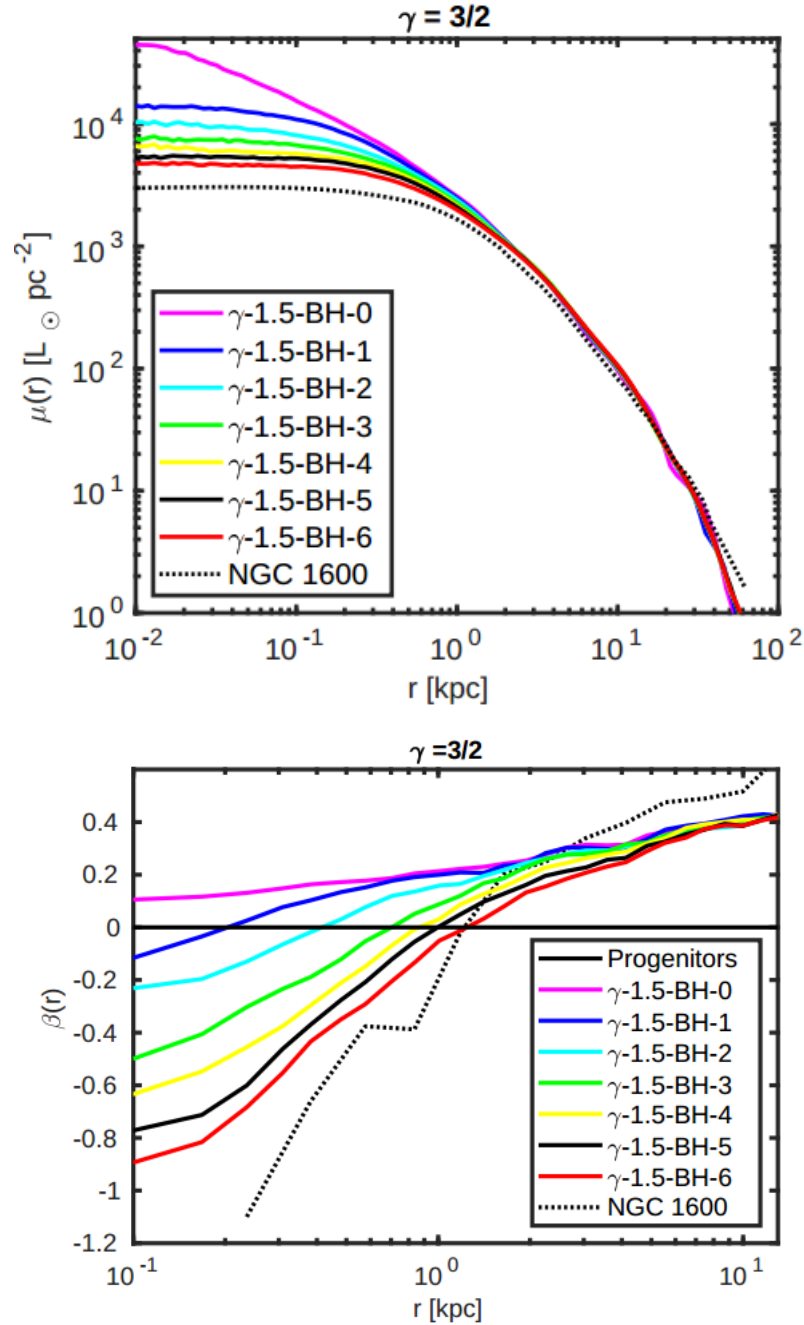
Figure 6.3: Density (top panel) and anisotropy (bottom panel) profiles of the equal-mass merger simulations, taken from Rantala et al., 2018a. The $\gamma - 1.5 - bh - N$ labels correspond to our M1-bh$N$ series. With increasing black hole mass the density profile develops a core in the center, and the anisotropy tends more towards a tangential bias. In both figures the simulations are also compared with observed massive elliptical galaxy NGC1600, which hosts a very massive black hole.

6.2 Kinematic maps

In order to understand how our galaxy sample would look like if we were to observe it realistically, we produced mock-IFU kinematic maps similar to the ones from previous chapters. The detail on the construction of these maps can be found in Chapter 2.1.4, with the only difference being that we skipped the pseudo-particle expansion, as the KETJU implementation alleviates significantly the problems introduced by having a softening length, and the spatial resolution of the simulations is anyway higher than the pixel resolution of the map. In all the maps the line-of-sight is the intermediate axis of the galaxy (as determined through the reduced inertia tensor), the x-axis is the major axis and the y-axis is the minor axis.

6.2.1 Equal-mass mergers

Figure 6.4 shows kinematic maps (V_{avg}, σ, h_3, h_4) for the equal-mass merger simulations, with increasing black hole mass going from top to bottom. In general all these maps are typical of slow-rotators, with low average velocity (< 20km/s) and very high velocity dispersion values ($300-370$km/s in the center, increasing with increasing black hole mass). The simulation without black holes shows some rotation only in the outer parts of the galaxy, with positively-correlated h_3, which hints at the galaxy having a prolate shape (we will cover the shape of these systems in Chapter 6.3). In the presence of black holes the orbital structure of the system is affected, and the larger the black hole mass, the stronger the effect. Starting from M1-bh3 rotation patterns emerge in the center in a progressively larger area. These patterns have corresponding anti-correlated patterns in the h_3 map. The h_4 map also gets progressively more negative in the central region, hinting at a more tangentially-biased orbital structure. This is in agreement with the change in anisotropy (right panel of Figure 6.3).

6.2.2 The black hole orbit reversal effect

Figure 6.4 hints at another interesting phenomenon. The simulations with the highest black hole masses show counter-rotating patterns in their V_{avg} maps. These are indeed caused by the black holes, but their explanation is not straightforward. During the merger, the black holes flip their orbital angular momentum several times, due to the gravitational influence of the stars that get ejected from the core of the two galaxies. These stars form tidal features that attract the black holes until they flip angular momentum. As these flips happen at different radii, they leave an imprint in the kinematics of the stars that interact with them, in the form of these counter-rotating features. This is remarkable, as it shows that counter-rotating cores, which are often observed in massive early-type galaxies, can form even without dissipation due to gas dynamics, but simply through collisionless dynamics of black holes and stars. This effect can happen also without black holes as long as the merger remnant is prolate and thee merging galaxies have stellar cusps (Tsatsi et al., 2015; Barnes, 2016), but black holes make the effect stronger and more long-lasting. A
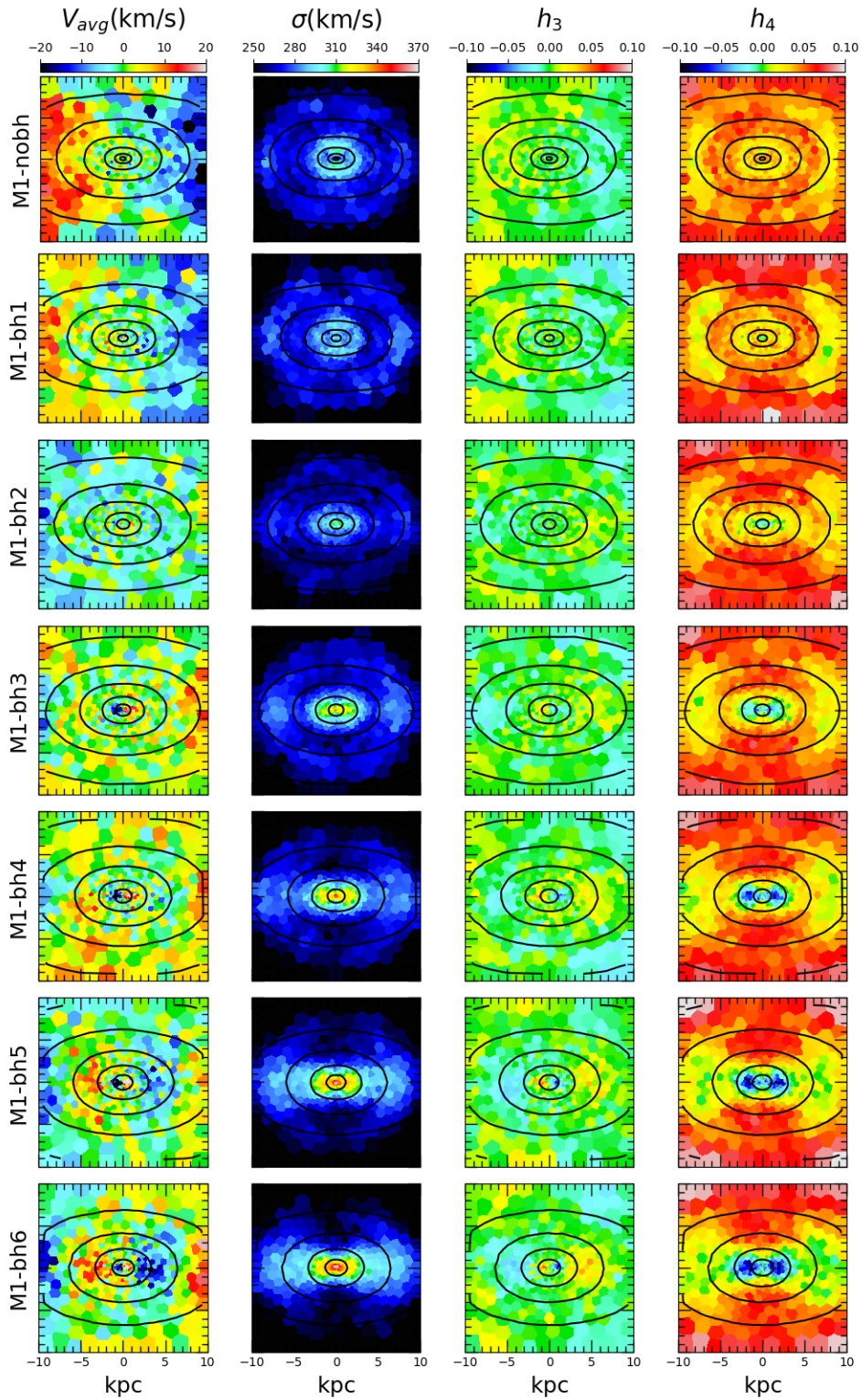
Figure 6.4: Kinematic maps for the equal mass merger remnants with increasing black hole mass. The black hole scouring effect allows for visible rotation in the inner parts, proportionally to black hole mass. This is seen both in the velocity and h_3 maps, which are anticorrelated, and in the h_4 map, which is negative in the center, indicating tangential anisotropy.

more thorough explanation of this effect is presented in Rantala et al. (2018b), but later in this Chapter we will analyze in detail how the orbital structure of the system is impacted by it.

6.2.3   Mergers with different mass ratios

Figure 6.5 shows kinematic maps for the set of remnants from minor merger simulations, from the one with the smallest merger ratio (5:1, top panel) to the equal-mass merger (bottom panel). The 5:1, 4:1 and 3:1 merger remnants (M5, M4, M3) look very similar. In all cases the velocity map has only very weak features, as is the case for the h_3 map. The dispersion is centrally peaked and very large compared to the average velocity (up to 370 km/s). The h_4 map is mainly positive, with a central $h_4 < 0$ region. All of these remnants are completely pressure-supported, and differ little from the main progenitor galaxy. The (projected) shape of the galaxy gets progressively more flattened. In the 2:1 merger remnant (M2), rotational patterns start appearing: coherent rotation in the V_{avg} map, anti-correlation with the h_3 map in the central two-three kpc and a larger area of the map with negative h_4. The velocity map shows counter-rotating region originating from black hole orbit reversals. In the 1:1 merger remnant (M1-bh6), as already described in Chapter 6.2.1, all of these features become stronger: the (counter-)rotation is very clear, the velocity dispersion increases significantly, h_3 is anti-correlated with V_{avg} in the whole extent of the map, and more spaxels have negative h_4. The final row of Figure 6.5 shows the kinematics of M5x5, the merger remnant of five minor mergers in succession, with the same total stellar mass as the M1 series and the same total black hole mass as M1-bh6. Its velocity map is completely featureless, and its velocity dispersion is very high, also in the outskirts. This suggests that it is kinematically very complex, as one would expect from the remnant of multiple mergers. In the next Chapters we will better understand why.

6.2.4   Global trends in the kinematics

So far we compared our simulations to each other qualitatively using their kinematic maps, but we would like to compare them quantitatively. To do so we employ the global parameters λ_R (projected angular momentum) and ξ_3 (relation between V_{avg}/σ and h_3), introduced in Chapter 2.1.3. Figure 6.6 shows ξ_3 as a function of λ_R for our sample, both calculated within the effective radius R_e. The coloured markers represent the equal-mass merger series, while the grey-scale markers represent the minor merger series. Compared to the equivalent figures in Chapter 4, the range of the two axes has been restricted to $0 < \lambda_R < 0.1$ and $-2 < \xi_3 < 0$, as in this case our whole sample is made of slow-rotators. All our galaxies have in fact $\lambda_R < 0.03$, owing to their very high velocity dispersion. Even when there is net rotation present (e.g., M1-bh6), the average velocity only reaches to $\sim 20\mathrm{km/s}$, with dispersion values above 300km/s. There is however a trend with black hole mass and merger configuration. The slowest-rotating galaxy is M1-nobh, with $\lambda_R \sim 0.01$, and it shows no clear trend between h_3 and velocity ($\xi_3 \sim 0$). The rotation that appears in the outer parts of the kinematic maps of this galaxy, with positively correlated h_3, is
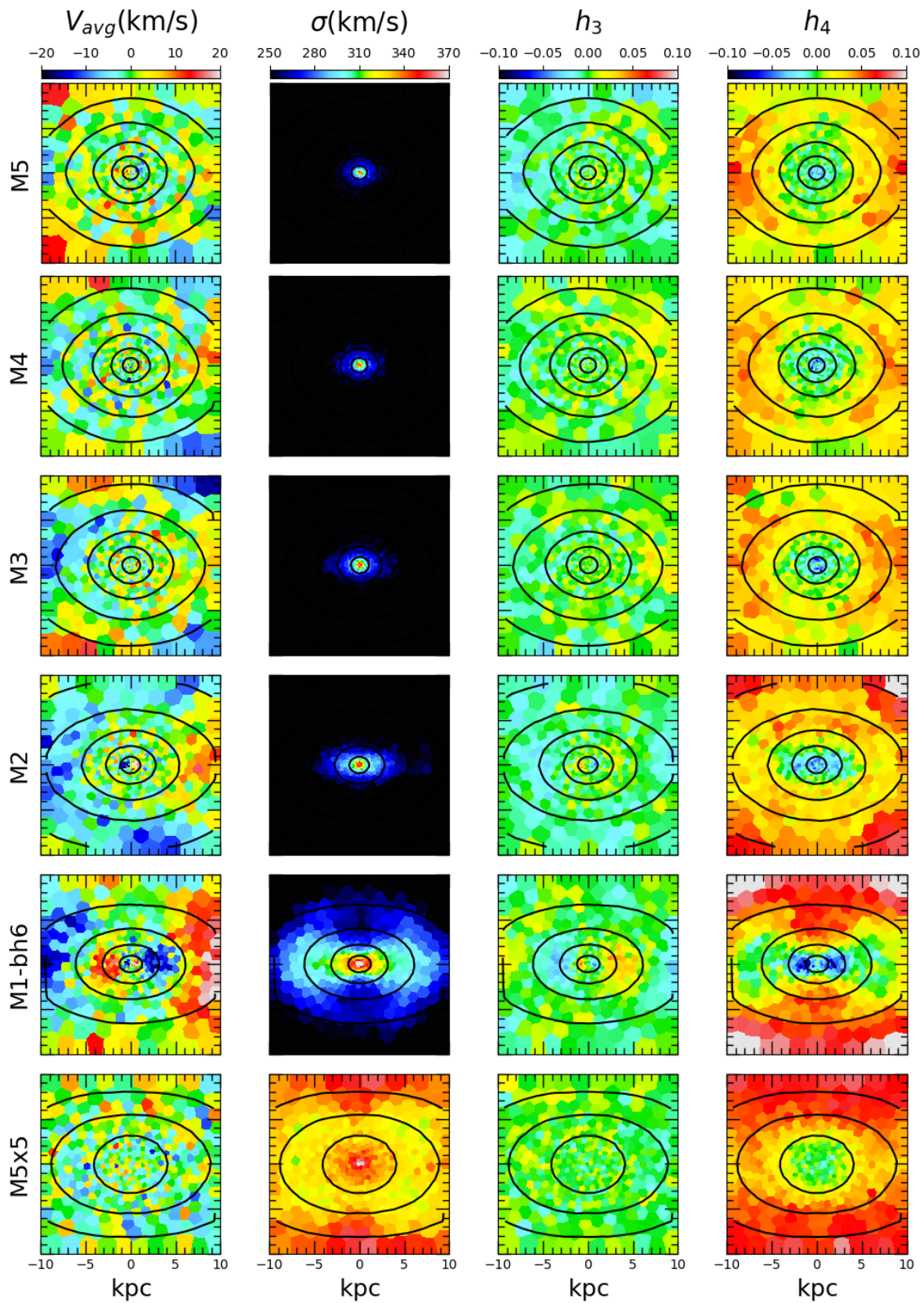
Figure 6.5: Kinematic maps of minor merger remnants, with increasing mass of the satellite, from 5:1 (top) to 1:1 (bottom). The last row shows the M5x5 simulation, which is a remnant of five minor mergers in succession.
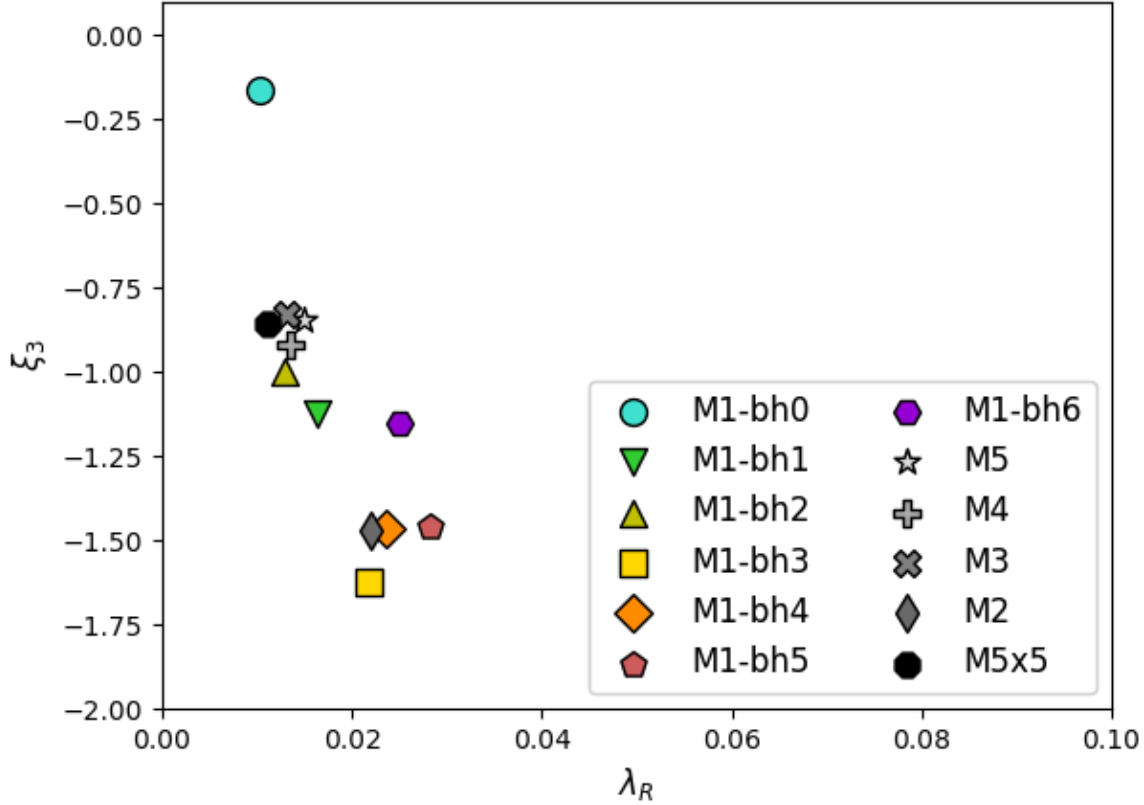
Figure 6.6: ξ_3 as a function of λ_R for our simulation sample. All galaxies are clear slow-rotators, and the ones that have non-zero ξ_3 have values around -1 / -2 (steep h_3- V_{avg}/σ anti-correlation).

not counted in the computation of λ_R and ξ_3, as it mainly lies beyond R_e. The galaxies with small black hole masses (M1-bh1, M1-bh2) and the remnants of minor mergers also have $\lambda_R \sim 0.01$, but they show some anti-correlation between h_3 and V_{avg}/σ , resulting in a slightly negative ξ_3 (~ -1). M2 (2:1 merger mass ratio remnant) is an exception among the minor mergers, in that it shows a larger λ_R (~ 0.02) and lower ξ_3 (~ -1.5). In this case, the difference in mass between the black holes of the two progenitors is small enough to form visible rotating features in the center of the kinematic maps. M1-bh3, M1-bh4 and M1-bh5 have similar values of λ_R and ξ_3 also because of the effect of their black hole binaries. Compared to M2, they have a clearer anti-correlation pattern between h_3 and V_{avg}/σ (larger $abs(\xi_3)$), but also a steeper trend (smaller $abs(\xi_3)$). M1-bh6 has similar λ_R, but its ξ_3 value is slightly smaller in absolute value (~ -1.2) because its h_3-V_{avg}/σ trend is even steeper.

6.3   Orbit analysis

To understand more in detail the orbital structure of the galaxy we ran our orbit classification pipeline (see Chapter 2.2.3 for a description) on this simulation sample. In the case of these simulations we centered the galaxies' position and velocity on the center of mass of their black hole binary, and orient the galaxy according to the reduced inertia tensor of the stars, so that the long axis is the x axis, the short axis is the z axis and the intermediate axis is aligned with the line-of-sight.

6.3.1   Equal-mass mergers

Figure 6.7 shows the frequency of different orbit types as a function of radius, for six of the equal-mass merger simulations: M1-nobh (top left), M1-bh1 (top right), M1-bh2 (center left), M1-bh4 (center right), M1-bh5 (bottom left), M1-bh6 (bottom right). Orbits are classified as box, z-tube, x-tube, irregular, and 'not classified'. The latter means that the orbit classification scheme failed to classify this particle because of inconsistent orbit types throughout the 50 periods that get computed. Additionally, z-tubes are also separated in prograde (dashed line) and retrograde (dotted line). In all our simulations from this sample the 'not classified' fraction is very high, particularly towards the center of the galaxy. This issue does not seem to depend on black hole mass, and could possibly stem from the analytic potential fit not being accurate enough, or from our assumption that the potential is static being incorrect (figure rotation). As we will show later however, this problem does not seem to happen preferentially in a particular orbit type, so it should not skew the relative frequencies of the other orbit types by a large amount. In all cases x-tubes dominate in the outer parts and box orbits become more prevalent in the inner parts. Interestingly, the frequency of box orbits is roughly the same in all simulations, contradicting our expectation that black hole scouring would lower it. If the analysis is correct, this means that black hole scouring, in the way we understand it, is negligible, or that we do not fully understand it. With increasing black hole mass the trend we see is that x-tube orbits become less prevalent in the center, while z-tube orbits become more common. In the M1-nobh simulation the center is completely devoid of z-tubes, while in M1-bh6 they are $\sim 15\%$ of all orbits. If we look at prograde and retrograde z-tubes separately, they mostly balance each other at every radius, but the regions where one has an excess over the others are consistent with the counter-rotating features seen in the kinematic maps. Irregular orbits are relatively rare, especially in the central region. The reason why x-tube orbits become more rare with increasing black hole mass lies in the three-dimensional shape of the system. Prolate and triaxial potentials allow for x-tube orbits, but the black holes make the potential more spherical or oblate within their sphere of influence, forcing particles on different kinds of orbits. Figure 6.8 compares the three-dimensional shape of the four galaxies we considered. The left panel shows the ratios c/a and b/a between the axes a, b and c of the system ($a > b > c$), calculated through the reduced inertia tensor (see Appendix 4.2). The binning was done using the binding energy rather than the radius, as otherwise the measured shape would be biased towards spherical.
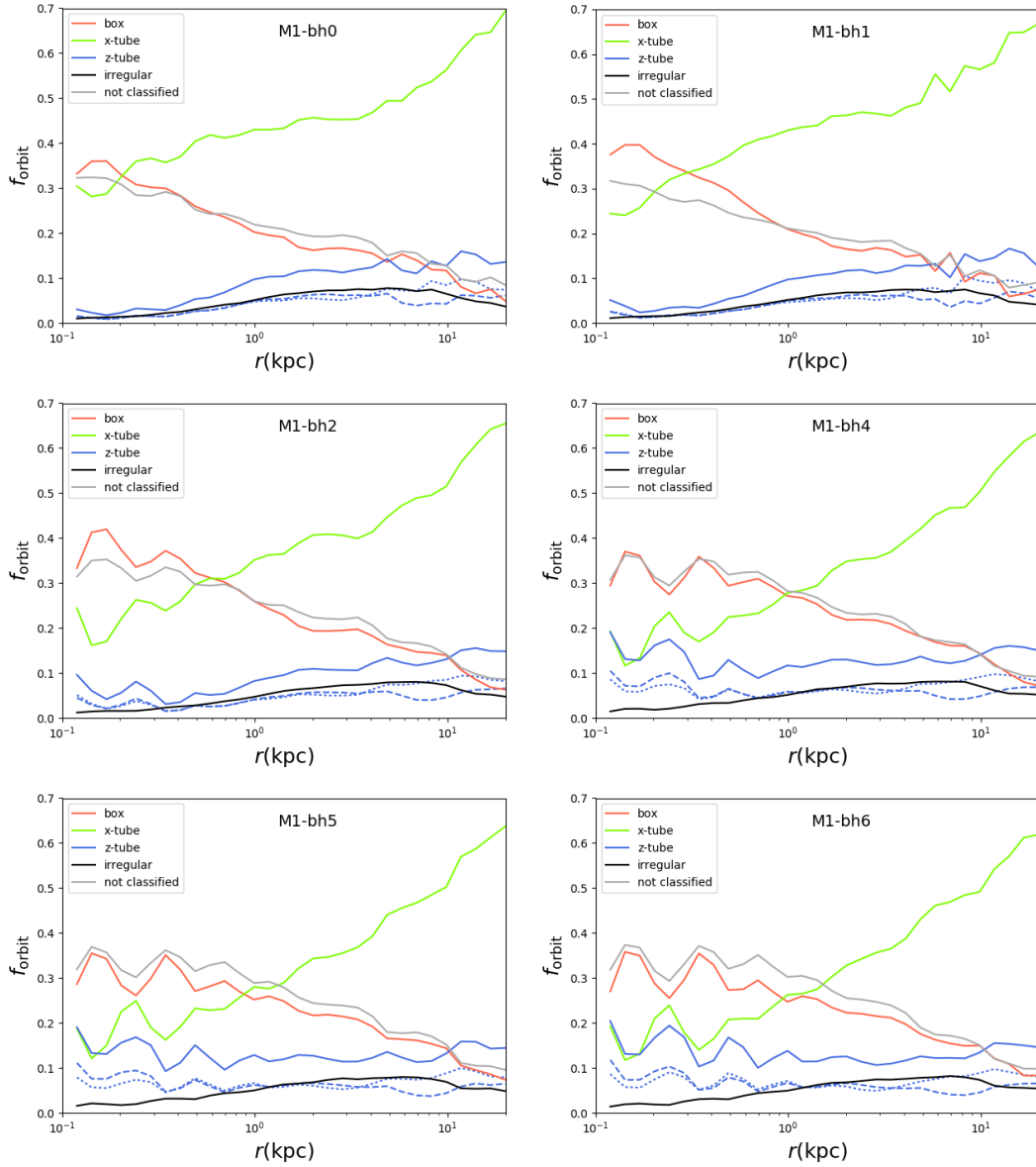
Figure 6.7: Frequency of the different orbit types as a function of radius, for four of our equal-mass merger simulations: M1-nobh (top left), M1-bh1 (top right), M1-bh2 (center left), M1-bh4 (center right), M1-bh5 (bottom left), M1-bh6 (bottom right). Increasing black hole mass makes x-tubes less common and z-tubes more common. Contrary to expectations, the fraction of box orbits is very similar in all our remnants.

The circular marker represents the value in the center of the galaxy (at $0.1\,\mathrm{kpc}$), and the line shows the values at different radii all the way to 10kpc. The value at the effective radius is marked by a square. In the M1-nobh simulation both axis ratios are around 0.7 in the whole radial extent; this means the galaxy is prolate. All the other simulations have similar values at large radii, but in the center they all become spherical ($c/a \sim b/a \sim 1$). This is caused by the black holes dominating the potential in the central regions. To better understand at which radius the shape switches from prolate to spherical we plotted the triaxiality parameter T as a function of radius for the same four simulations (right panel of Figure 6.8). While the M1-nobh simulation always has $T \sim 0.9$ (prolate), the other simulations have smaller values of T (oblate/spherical) with increasing black hole mass. The dip in T also reaches larger radii: $\sim 0.5\,\mathrm{kpc}$ for M1-bh1, $\sim 1\,\mathrm{kpc}$ for M1-bh2 and $\sim 10\,\mathrm{kpc}$ for M1-bh6. This is consistent with the decrease of x-tubes and increase of z-tubes in the central regions with increasing black hole mass.

6.3.2   Kinematic maps of selected orbit types for M1-bh6

In order to test the correct functioning of our orbit analysis pipeline, and to better understand the kinematic structure of M1-bh6, we plotted kinematic maps in which we only used particles from each orbit family. This kind of separation can be done also for real galaxies using Schwarzschild modelling (van den Bosch et al., 2008). In the case of our simulated galaxy M1-bh6, the result is in Figure 6.9. From top to bottom, it shows the kinematic maps for box orbits, x-tube orbits, all z-tube orbits, prograde z-tube orbits, retrograde z-tube orbits, and orbits which the pipeline failed to classify. Stars on box orbits have very high velocity dispersion in the central region (up to $500\,\mathrm{km/s}$) and low average velocity ($< 50\,\mathrm{km/s}$). This is expected, as these stars have very radial orbits which move fast near the center of the potential. There is some net rotation ($\sim 10\,\mathrm{km/s}$), following the same pattern as the overall galaxy. This could be a symptom of some issue in the orbit classification, such as the potential of the black holes not being correctly represented or figure rotation. h_3 is featureless in the central region and anti-correlated in the outer parts. h_4 is generally positive, because the LOS velocity distribution is dominated by a peak at $V \sim 0$ of orbits at their apocenter with extended high-velocity tails. It is instead negative in the center, where the LOS velocity distribution is relatively flat because of the different orientations of radial orbits at their pericenter. The x-tube orbits are preferentially distributed along the short axis of the galaxy, and don't show net rotation. The velocity dispersion is however very high above and below the midplane, and very low along it. h_4 is also very highly negative (-0.5) where the dispersion is high. This tells us that there is a double peaked LOS velocity distribution, with x-tubes rotating in both directions around the long axis of the galaxy and balancing each other out. The same is true for the z-tube orbits after switching long and short axes. The z-tubes however do show net rotation (up to $\sim 70\,\mathrm{km/s}$) with clearly anti-correlated h_3 values. This rotation changes sign in the same pattern as the full kinematic map of the galaxy: once at 0.2 kpc, once at 1 kpc, once at 3.5 kpc. The entity of these patterns gets however lowered by the presence of other orbit types. If we look at the prograde and retrograde z-tube orbits separately we see that
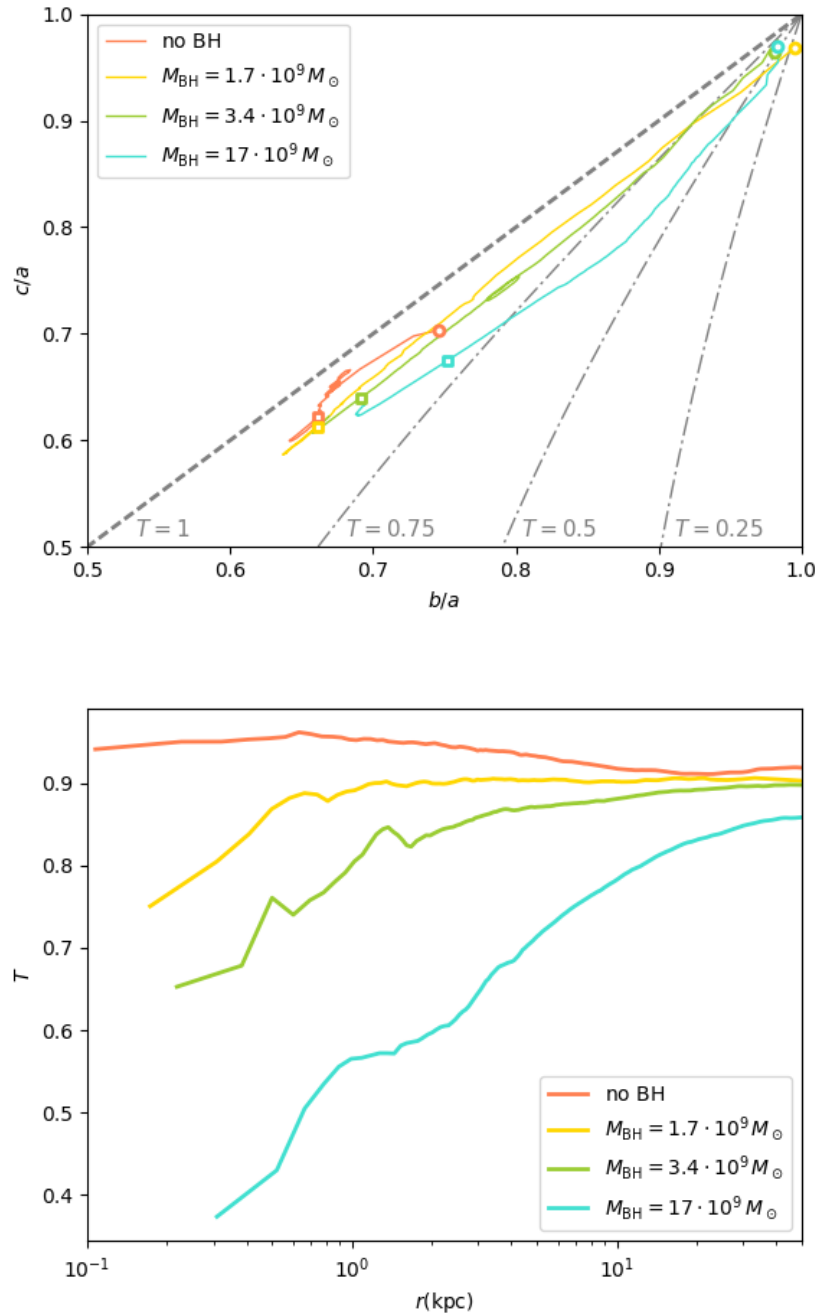
Figure 6.8: Top panel: axis ratios c/a and b/a (with a being the major axis) of four merger simulations with increasing black hole mass, at different radii. The circular marker indicates the value at the center of the galaxy, while the square marker indicates the value at the effective radius. The dashed line indicates $b = c$ ($T = 1$), while the dot-dashed lines correspond to other constant values of the triaxiality parameter ($T = 0.75, 0.5, 0.25$). Bottom panel: Radial profile of T of the same galaxies.

they both rotate very fast (up to $\sim 300\,\mathrm{km/s}$) and more or less balance each other, but the excess of one over the other at different radii causes the counter-rotating features seen in the general kinematic map. This kind of superposition resulting in counter-rotating features has also been seen in observed galaxies (Figure 13 of van den Bosch et al. 2008). The irregular orbits are very few, so we do not show the corresponding kinematic map. Finally, the orbits that our analysis tools failed to classify seem to follow the same pattern as the overall galaxy, meaning that this does not introduce big biases in our radial frequency comparison. The failure in classifying them is probably once again caused by the fit of the gravitational potential not being adequately accurate in the central region.

6.3.3   Mergers with different mass ratios

In the series of simulations with different merger mass ratios we find a different orbital structure. From the perspective of the larger galaxy, a merger affect its orbital structure mainly in two ways: the infalling satellite's black hole affecting its stars and the satellite's stars being added to it. While in a major merger these happen together, in a minor merger most of the satellite's stars do not reach the inner parts of the main galaxy. Figures 6.10 show the fraction of different orbit families at different radii, for each of the minor merger simulations: M5 (top left), M4 (top right), M3 (bottom left), M2 (bottom right). In all the remnants, the fraction of orbits which were failed to be classified is around 30% in the center of the galaxy and drops to less than 10% in the outer parts, similarly to the equal-mass mergers. This is once again likely an effect of our static analytical potential not being an accurate representation of the real one. The orbit structure of M5, M4 and M3 is very similar. They are dominated by x-tube orbits in the outer parts ($\sim 60\%$), while the inner parts are more isotropic. Z-tubes are the second most common orbit type, accounting for 15% of all orbits in the outskirts but rising to $\sim 30\%$ in the center. Box orbits are roughly constant at about 10%. The central region with more z-tubes and less x-tubes is likely produced by the black holes. In fact in M2 we see similar trends, but the central region is larger (1 kpc). There is also more matter coming from the satellites in the central region, slightly increasing the fraction of box orbits. All the remnants have a negligible amount of orbits classified as irregular.

The differences in orbit fractions can also be understood by looking at the shape of these galaxies. Figures 6.11 show the axial ratios and triaxiality parameter as a function of radius for these galaxies. All of them are spherical in the center ($b/a \sim c/a \sim 1$) and prolate in the outskirts. For M5, M4 and M3 this transition starts happening at 0.5 kpc (as seen in the triaxiality plot). Considering that in the M1-nobh simulation the whole galaxy is prolate, this spherical shape in the center is caused by the gravitational impact of the black hole. This is likely connected with the increased number of x-tube orbits in the outer parts of M5, M4 and M3, which happens at the same radius. In the case of M2, the black hole's influence radius gets much larger, making the merger remnant spherical up to a larger radius (~ 2 kpc). This is also reflected in the diminished role of x-tubes. The additional stellar matter coming from the satellite does not seem to affect significantly the shape of the remnant.
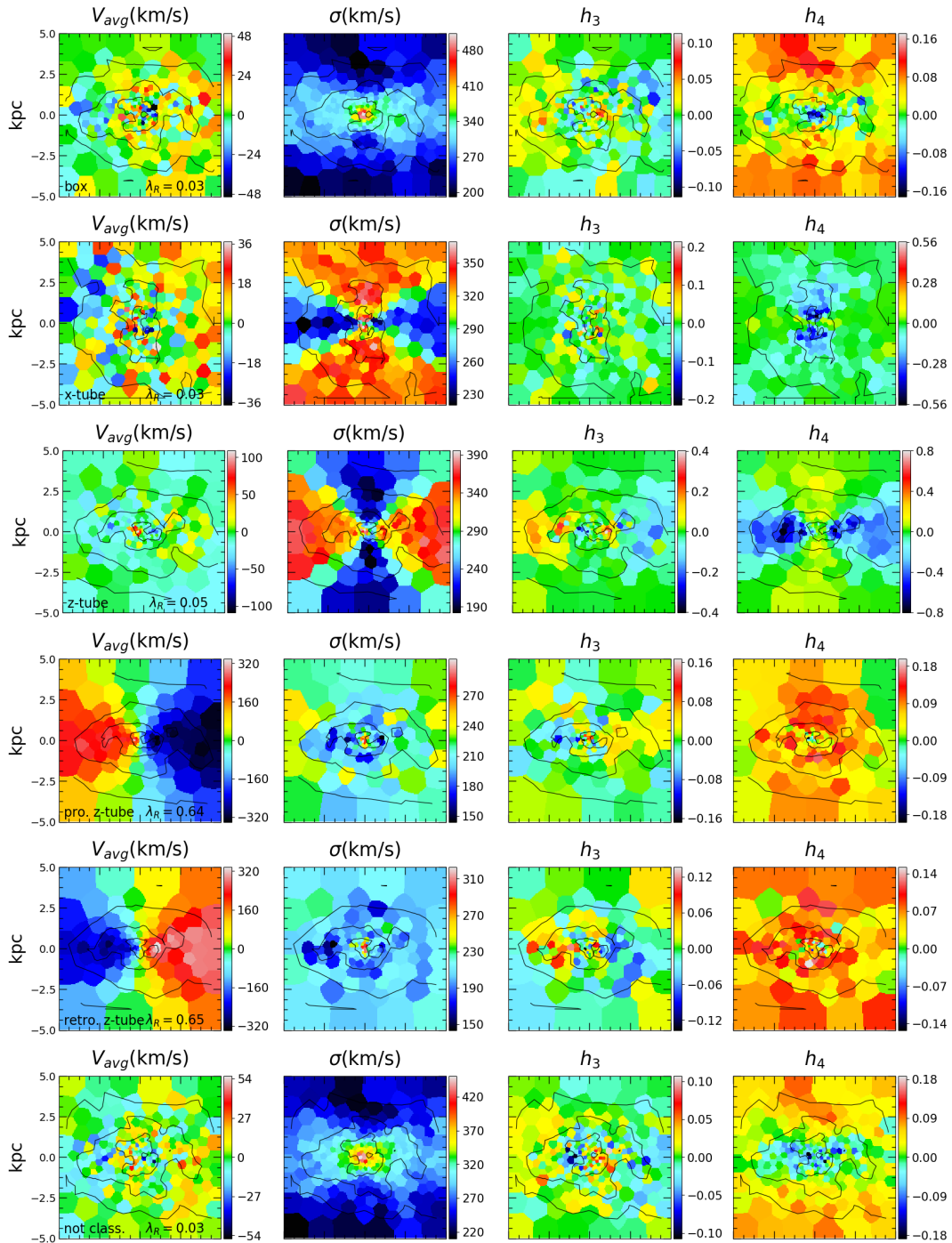
Figure 6.9: Kinematic maps of major merger remnant M1-bh6 selecting only particles of a specific orbit type. From top to bottom: box, x-tube, z-tube (total), z-tube (prograde), z-tube (retrograde), not classified.
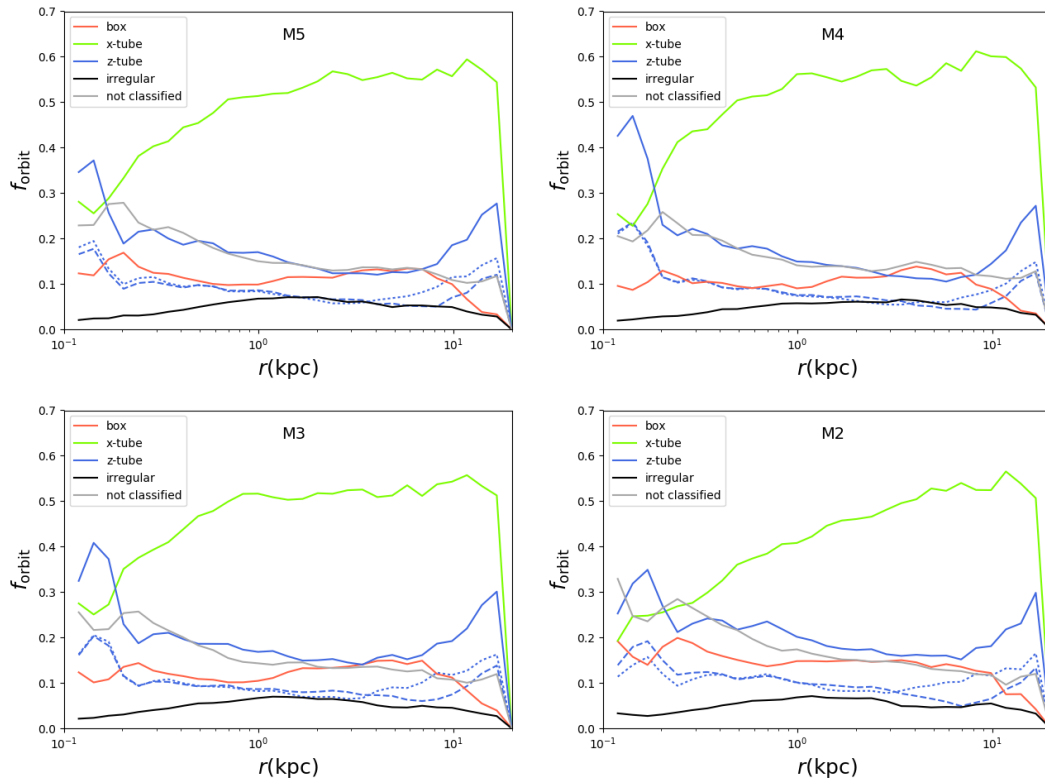
Figure 6.10: Frequency of the different orbit types as a function of radius, for our four unequal-mass merger simulations: M5 (top left), M4 (top right), M3 (bottom left), M2 (bottom right).

6.3.4 Multiple minor mergers

M5x5, the simulation with multiple minor mergers, has different properties from all the others. Figure 6.12 shows its orbital fractions, and Figures 6.11 show its axial ratios and triaxiality profiles together with the already discussed single minor merger remnants. The shape is spherical in the center and triaxial ($T \sim 0.5$, $c/a \sim 0.5$, $b/a \sim 0.75$) in the outer parts. The triaxiality jump in the at around 1kpc actually happens because of a small change in the axial ratios when they are close to spherical, as can be seen in the left panel. The less prolate and more oblate shape compared to our other remnants is consistent with M5x5 being the remnant with the most z-tubes in our sample (20%). It has very few x-tubes and is dominated on the whole radial range by box orbits (40%). This is consistent with its origin from mergers with much smaller galaxies (5:1 to 9:1 mass ratios), which deposited their mass in the outskirts producing a lot of box orbits. We can better understand the large number of z-tubes looking at the kinematic maps for only particles on prograde and retrograde z-tube orbits, which we show in Figure 6.13 (top and bottom panel respectively). In both prograde and retrograde z-tubes the rotation speed does not depend on the azimuthal angle the way a regular rotator would ($\propto \cos\theta$). This suggests that many of these stars came from the satellites, and their orbits are tied to the satellite's original orbital planes, which were different from each other. This explains why even when selecting only prograde (or retrograde) z-tubes the dispersion map has such high values (up to 320 km/s) apart from a small region in the midplane. This also explains the unusually high values of velocity dispersion which we saw in the full kinematic map of M5x5 (bottom panels of Figure 6.5).

6.3.5 Global trends with triaxiality

We saw how the shape of the galactic potential can determine which kinds of stellar orbits are more frequent in the galaxy. Here we would like to compare the orbit fractions and shapes of our simulations directly using the triaxiality parameter T. In the top panel of Figure 6.14 we show the fraction of x-tube orbits within the effective radius R_e as a function of T (also computed within R_e) for our simulations. There is a positive correlation between the two parameters for the major mergers (M1-bh(n)) and M5x5. We expect this correlation, because the more a galaxy is prolate, the more it can support x-tube orbits, as we also saw in Chapter 4. The major merger simulation without black holes (M1-bh0) is the most prolate of the sample ($T > 0.9$) and has one of the highest fractions of x-tubes at about a third of all orbits. The minor merger simulations, especially the ones with smaller satellites, are outliers, likely because they are close to spherical within their effective radius, making the triaxiality parameter inadequate. The bottom panel of Figure 6.14 shows the fraction of z-tube orbits as a function of triaxiality. Once again the minor mergers are outliers, but for the other remnants there is an anti-correlation: the closer a galaxy is to prolate, the less z-tube orbits it contains. M5x5 has the highest fraction of z-tubes at about a fifth, and also the lowest T parameter (~ 0.1).
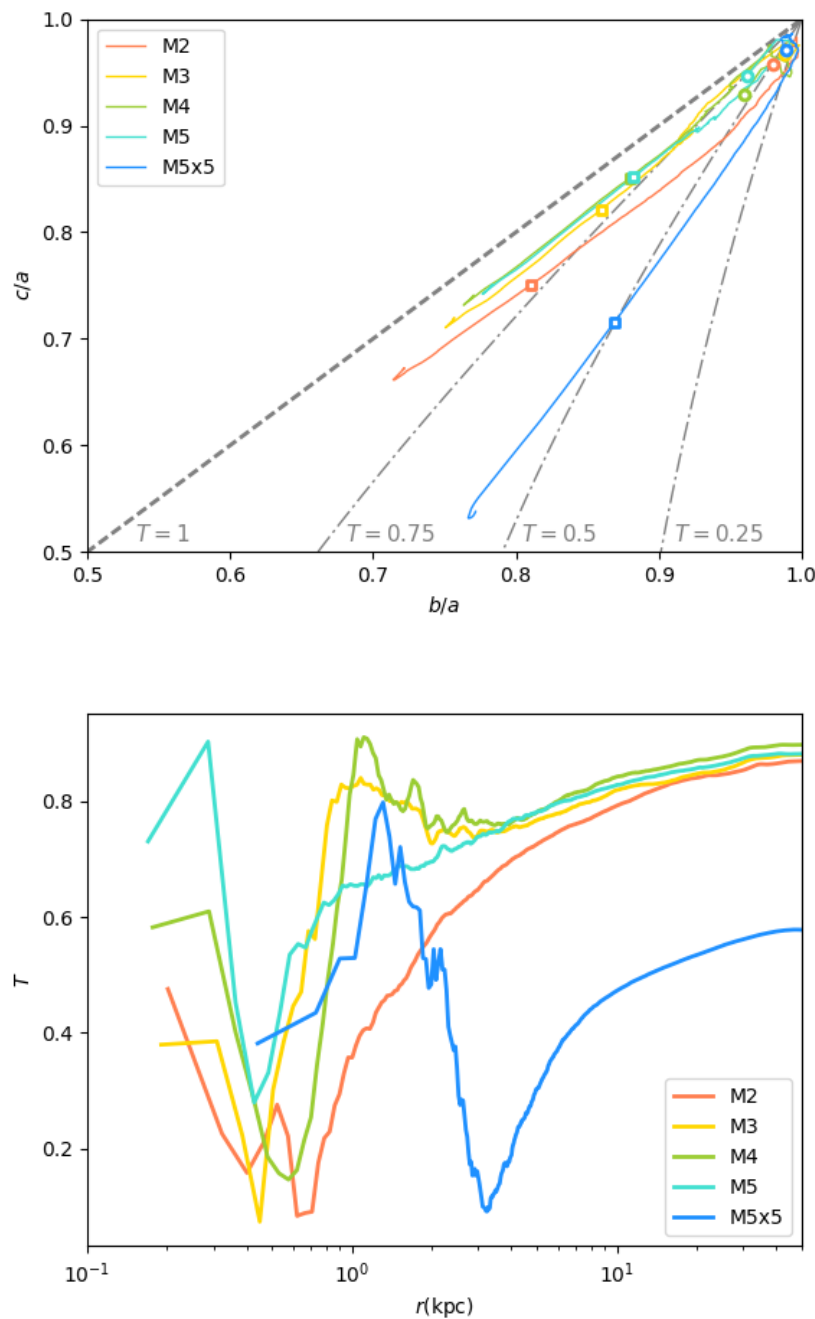
Figure 6.11: Top panel: axis ratios c/a and b/a (with a being the major axis) of four minor merger remnants (M2, M3, M4, M5, M5x5), at different radii. The circular marker indicates the value at the center of the galaxy, while the square marker indicates the value at the effective radius. The dashed line indicates $b = c$ ($T = 1$), while the dot-dashed lines correspond to other constant values of the triaxiality parameter ($T = 0.75, 0.5, 0.25$). Bottom panel: Radial profile of T of the same galaxies.
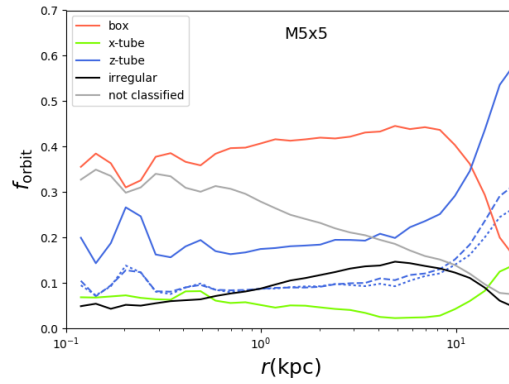
Figure 6.12: Frequency of the different orbit types as a function of radius, for the M5x5 simulation (multiple minor mergers, same mass as the M1 series). X-tube orbits are very rare.
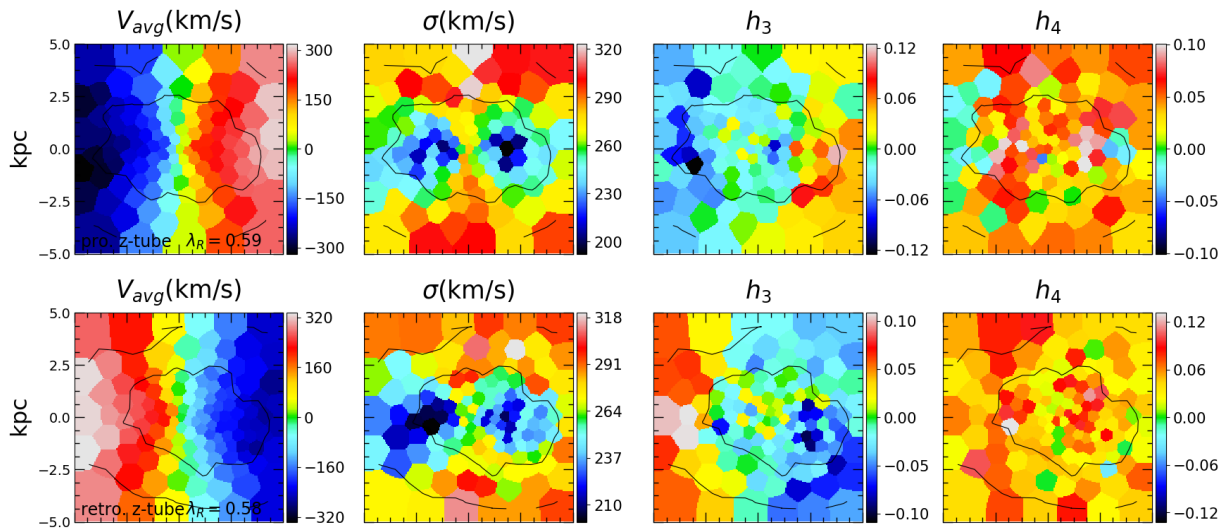
Figure 6.13: Kinematic maps of the galaxy remnant M5x5 selecting only particles on prograde (top panel) and retrograde (bottom panel) z-tube orbits.
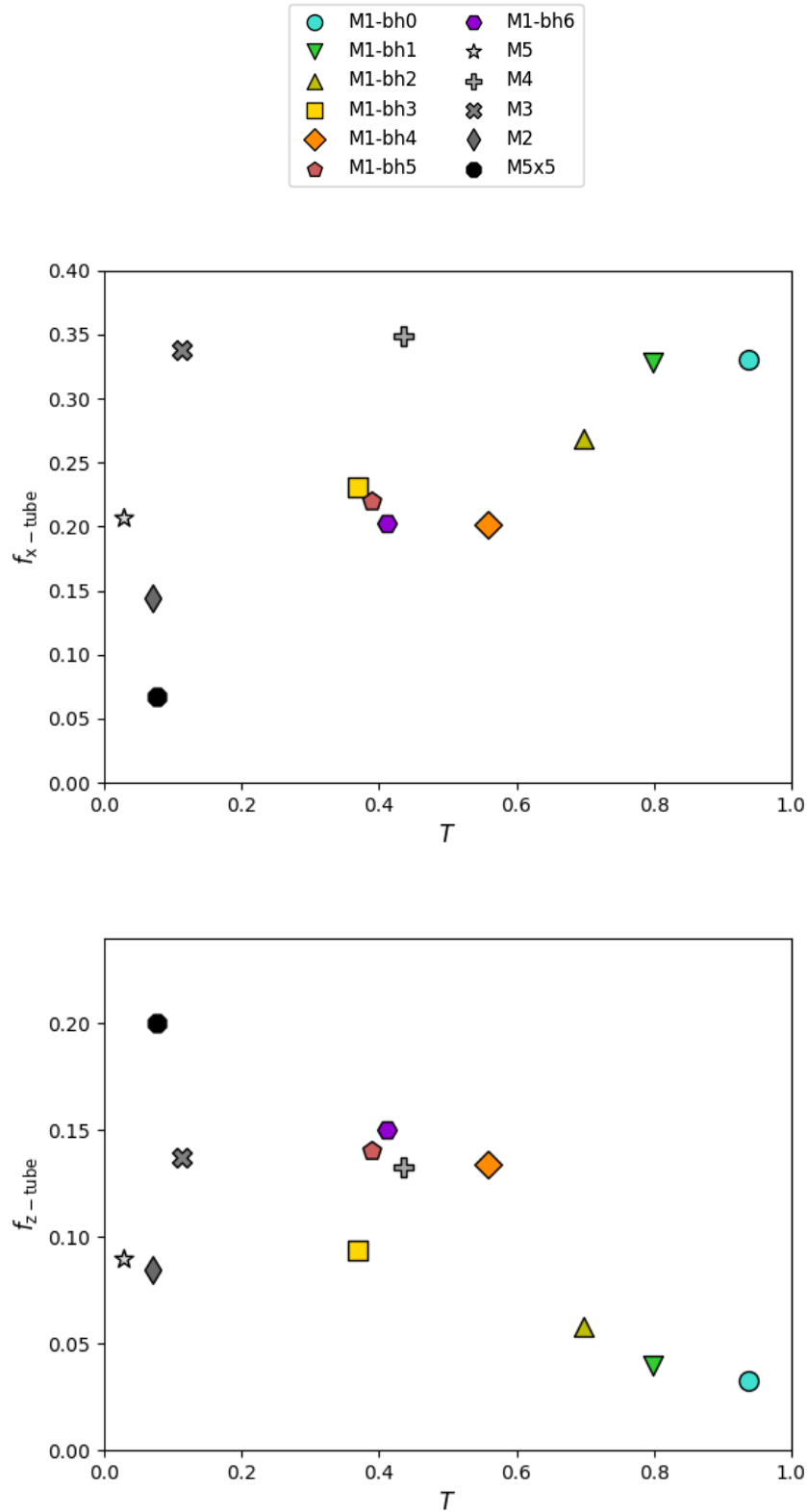
Figure 6.14: Fraction of x-tube orbits (top panel) and z-tube orbits (bottom panel) within R_e as a function of triaxiality for our simulation sample.

6.4   Summary

In this Chapter we analyzed the dynamical effect of supermassive black holes during galaxy mergers. As already pointed out in (Rantala et al., 2018a; Rantala et al., 2018b), the gravitational impact of the black holes results in cored density profiles with more tangentially-biased orbits. This happens in two phases: first, during the merger itself the central stellar cusp gets destroyed because of violent relaxation, due to the quickly varying potential of the spiralling-in black holes. Then once the black holes formed a binary in the center of the remnant, stars on radial orbits are more likely to pass closer to the binary and get kicked out, further decreasing the central density and favouring tangential orbits. Furthermore, the two black holes can flip their orbital angular momentum during the merger, leaving an imprint in the kinematic maps of the remnant. In this Chapter we added to these results with a more in-depth look at the orbital structure and three-dimensional shape of the remnant. We found that:

- All our merger remnants (except M5x5) are dominated by x-tube orbits. This is reflected in them having a prolate shape, and likely the result of forming through gas-less mergers with small impact parameters. We however never see any net prolate rotation; these x-tubes are always equally likely to have a positive or negative x component of the angular momentum.

- The fraction of x-tubes decreases gradually with increasing black hole mass, especially in the core of the galaxy. At the same time the fraction of z-tubes increases.

- All our galaxies have a spherical shape near the center, because of the gravitational potential of the black holes, and a prolate shape in the outskirts. The size of the spherical region increases with black hole mass, and coincides with the radial range where x-tube orbits are suppressed.

- Unlike the x-tubes, we find z-tube orbits to show net rotation, and with high black hole masses even counter-rotating features. While both prograde and retrograde z-tubes are present at all radii, the slight dominance of one over the other creates the counter-rotating pattern.

- In the equal-mass mergers, box orbits are surprisingly unaffected by the black holes, and always dominate the very core of the remnants. Only in the simulations with the most massive black holes the fraction of box orbits slightly lowers. If the analysis is correct, this suggests that the orbit scouring effect - in the way we understand it - is only relevant for very massive black holes, and most of the dynamical impact of black holes happens during the initial phase of the merger.

- In the minor merger remnants the fraction of box orbits is low throughout the galaxy, probably because few of the stars of the satellite reach the central region. The outer parts are dominated by x-tubes, but in the inner regions they drop and z-tubes are more common. The size of this inner region increases with black hole mass.

- The simulation in which five minor mergers took place one after the other (M5x5) shows unique properties within our sample. The galaxy has a triaxial shape and is dominated by box orbits throughout its radial range. It also has high z-tube fractions, despite the absence of net rotation. X-tubes are very rare. The z-tube orientations are likely connected to the different orbital planes of the satellite galaxies, and their superposition causes very high velocity dispersion values.

- In all the equal mass merger galaxies there is a correlation between the fraction of x-tubes and z-tubes and triaxiality parameter T. The correlation is positive for x-tubes and negative for z-tubes. The minor merger simulations are outliers, possibly due to their close-to-spherical shape.

These results come with various caveats, even within the assumptions inherent to these idealized isolated simulations. In all of our galaxies a big fraction of orbits are 'not classified', meaning that our classification scheme failed. While the kinematic maps show that these orbits roughly follow the same trend as the overall distribution, it is not unlikely that they skew the results. We also assume the potential to be static, which is not necessarily the case; in particular, it could slowly rotate. This would also result in the misclassification of some of the orbits.

Chapter 7

Conclusions

In this thesis project we investigated several ways in which the dynamical properties of galaxies are impacted by their central supermassive black holes. While the general effect on galaxies' rotational support (Lagos et al., 2018), density profiles (Remus et al., 2017) and major merger remnants (Rantala et al., 2018a) was already known, we investigated all of these topics more in detail and found further insights. A detailed summary of our results can be found in Chapters 4.3, 5.3 and 6.4. Here we will collect the main conclusions.

7.1 SMBHs and 2D stellar kinematics

Our zoom simulations showed that AGN feedback contributes to all the typical properties of quiescent galaxies (slow rotation, old stellar age, low metallicity, boxy isophotes,...). Without AGN our galaxies would have very unrealistic properties for their mass, such as massive star-forming disks and very high metallicities. In our sample the impact of AGN becomes important only after $z = 1$, and it is especially strong during wet major merger events, where the remnant is completely different with or without AGN feedback. This is because of the intrinsically different kinematic and stellar-population properties of stars that formed in-situ and stars that were accreted from other galaxies. By severly limiting in-situ formation, AGN feedback affects all of these properties. It also affects the three-dimensional shape of galaxies, making them more likely to be triaxial rather than oblate. This is reflected in a different distribution of orbit families, with x-tube orbits becoming much more common with AGN feedback. Overall we found a strong decrease in the angular momentum λ_R when AGN feedback is present, with many more galaxies becoming slow-rotators, which is what we expect for this mass range. There can however be exceptions where AGN feedback effectively makes the galaxy rotate *faster*, because without it counter-rotating features would have formed. We introduced a parameter, ξ_3, which characterizes the trend of third moment of the LOS velocity distribution h_3. h_3 is typically anti-correlated to V_{avg}/σ in fast-rotators, but in galaxies with complex structures the slope of the trend can be different, or then can be no trend. We found that when the relation is tight, ξ_3 captures the slope of the trend, while when h_3 and V_{avg} are not correlated it goes to zero. We then

found that ξ_3 correlates with the shape of the system (as characterized by the triaxiality parameter T) and with the fractions of x-tubes (anticorrelation) and prograde z-tubes (positive correlation). This makes the parameter quite useful, given that triaxiality and orbit fractions are not directly observable. We compared the ξ_3 values of our simulations with the ones computed for the ATLAS^{3D} observations, finding that they cover the same distribution. However the ATLAS galaxies tend to have smaller ξ_3 than the simulations at a given λ_R value. We attribute this difference to either the observed galaxies being more likely to have bar features or to observational noise making the $h_3 - V_{\mathrm{avg}}/\sigma$ trend less tight.

7.2   SMBHs and mass estimations

We applied observational methods for estimating the mass and density profile of galaxies to mock data from our zoom simulations, to test how well they work. Jeans dynamical modelling is effective in retrieving the density profile of galaxies. We tested the JAM code (Cappellari, 2008) with two different families of mass models: a simple power-law for the total mass distribution and the sum of the light distribution multiplied by a free constant plus a power-law for representing the dark matter profile. The second model was generally more accurate, although it also uses five parameters instead of four. Total mass-to-light ratios were correctly recovered, with the power-law model slightly underestimating them. The anisotropy values from JAM modelling were instead not very accurate. We compared the dark matter fractions of our sample with the observations of the ATLAS^{3D} survey, finding that they cover the same range. An important caveat of these results is that our simulations are not always realistic. In all of them the density profile is cored in the center due to the gravitational softening, and this skews many of the JAM modelling predictions; for instance measured density profile slopes tend to be shallower. The limited particle resolution probably also complicates the modelling. Real galaxies, especially fast-rotators, are expected to be better represented by Jeans models. These tests are however still interesting, as they help us understand in which situations Jeans models can fail. We tested strong gravitational lensing as a mass estimator for the lens galaxy. The mass within the Einstein radius was almost always recovered to high accuracy, and the slope of the density profile at R_{einst} is also often accurate. We tested whether the density profile slopes of our galaxies depend on AGN feedback, something expected from other studies (Remus et al., 2017). We found that there is no clear difference for our galaxies, and a larger sample would be necessary to detect a trend.

7.3   SMBHs and orbit scouring in mergers

We analyzed a set of isolated merger simulations (Rantala et al., 2018a) to evaluate the dynamical impact of supermassive black holes on collisionless systems. The code used for these simulations includes a special integrator, KETJU (Rantala et al., 2017), which calculates the black hole dynamics and their interactions with stars and other black holes

very accurately and without softening. Rantala et al. (2018a) previously analyzed these simulations and found that SMBHs 'dig' a core in the density profile proportional to their mass, leaving a more tangentially biased orbit distribution. Here we looked more in detail at the orbit structure of the merger remnants, using 2D kinematic maps, analyzing their three-dimensional shape, and running a full orbit analysis. The orbital structure of our merger remnants is almost always dominated by x-tube orbits. This is reflected in them having a prolate shape, and probably caused to the small impact parameter of the merger. The fraction of x-tubes decreases in the central regions in the presence of black holes, which change the shape of the galaxy from prolate to spherical. Correspondingly, z-tubes become more common with larger black hole mases. Box orbits are more common in the central regions, and contrary to our expectations, their fraction shows almost no dependence on black hole mass. If our analysis is correct (see Chapter 6.4 for a list of the caveats), this would mean that our understanding of how the black hole binary impacts the surrounding galaxy is incomplete. Further analysis on these simulations will help understand the full picture. In the minor merger simulations we do not see major differences in the orbital structure of the remnants, which are all dominated by x-tubes and have low box fractions. Only in the 2:1 merger we see an increase in box orbits, due to more particle from the satellite reaching the inner regions. When there are multiple minor mergers in succession we find a remnant dominated by radial orbits even at large radii, with complex shape and kinematics. We also investigated the counter-rotating features that appear in the simulations with the largest black hole masses, already discussed in Rantala et al., 2018b. These features originate from the orbital angular momentum reversals of the black holes during the merger. Distinguishing prograde and retrograde z-tube orbits in our orbit analysis we see that both components are always present and rotating at the same net velocity, but the excess of one over the other at different radii produces the observed counter-rotation.

7.4 Future prospects

The main limiting factor in this thesis projects was given by the simulations' accuracy and sample size. Regarding the accuracy, the resolution of cosmological simulations is increasing significantly. We now have zoom simulations where the mass of stellar particles is in the range of tens of solar masses, even though just for dwarf galaxies (Wheeler et al., 2018). Once this will be possible for larger galaxies, we will be able to study more realistic stellar systems and and have better comparisons with observations, especially regarding the stellar kinematics. If we limit the simulations to high redshifts we can already reach these resolutions for larger systems. This can prove particularly useful, as observations of high-redshift galaxies are reaching higher and higher levels of detail. Recent observations were able to study the gas-dynamical properties of $z \sim 2$, finding that they possess massive turbulent gaseous disks and have almost no dark matter (Genzel et al., 2017). This gives important constraints to simulations and galaxy formation models, which would be perfectly suited for zoom simulations.

Our project was also limited by the small sample size, which did not allow to make meaningful statistical predictions. This would help constraining the many parameters that go into the subgrid models of simulation codes. While there are already many large scale simulations where statistical arguments can be made (e.g. Schaye et al., 2015, Vogelsberger et al., 2014a), these have much lower resolution ($\sim 700pc$), which makes many of their kinematic properties less accurate, especially near the center of galaxies. As we saw in Chapter 5, this is particularly true for testing density profile reconstructions. An important step was done recently in the Illustris TNG set of simulations. One of them, TNG50, will have spatial resolution (softening length) 300pc, almost as good as the zoom simulations we analyzed, but simulating a full cosmological box of size 50 Mpc. This will allow to better understand how stellar and total density profiles vary depending on other galactic properties and how well they can be evaluated by dynamical modelling and/or lensing. Another useful application would be analyzing the higher-order kinematics of galaxies in a statistical framework, using for instance the ξ_3 parameter we introduced, or additional parameters for representing the behaviour of h_4 maps. Higher-order kinematics have the potential to make us peek into the orbital distribution of galaxies in a simple way, and doing it on the scale of a cosmological box would allow us to make concrete predictions for their distribution and use them to test our models of galaxy formation.

Bibliography

(1) Agertz, O. et al. *MNRAS* **2007**, *380*, 963–978.

(2) Alatalo, K. et al. *ApJ* **2011**, *735* 88, 88.

(3) Auger et al. *ApJ* **2010**, *724*, 511–525.

(4) Aumer, M.; White, S. D. M.; Naab, T. *MNRAS* **2014**, *441*, 3679–3695.

(5) Aumer, M.; White, S. D. M.; Naab, T.; Scannapieco, C. *MNRAS* **2013**, *434*, 3142–3164.

(6) Bacon, R.; Accardo, M.; Adjali, L.; Anwand, H.; Bauer, S.; Biswas, I.; Blaizot, J.; Boudon, D.; Brau-Nogue, S.; Brinchmann, J.; Caillier, P.; Capoani, L.; Carollo, C. M.; Contini, T.; Couderc, P. In *Ground-based and Airborne Instrumentation for Astronomy III*, 2010; Vol. 7735, p 773508.

(7) Bailin, J.; Steinmetz, M. *ApJ* **2005**, *627*, 647–665.

(8) Barnabè, M.; Czoske, O.; Koopmans, L. V. E.; Treu, T.; Bolton, A. S. *MNRAS* **2011**, *415*, 2215–2232.

(9) Barnes, J.; Hut, P. *Nature* **1986**, *324*, 446–449.

(10) Barnes, J. E. *MNRAS* **2016**, *455*, 1957–1980.

(11) Barnes, J. E.; Hernquist, L. *ApJ* **1996**, *471*, 115.

(12) Behroozi, P.; Wechsler, R.; Hearin, A.; Conroy, C. *arXiv e-prints* **2018**.

(13) Bender, R. *A&A* **1988**, *193*, L7–L10.

(14) Bender, R.; Moellenhoff, C. *A&A* **1987**, *177*, 71–83.

(15) Bender, R.; Saglia, R. P.; Gerhard, O. E. *MNRAS* **1994**, *269*, 785.

(16) Bertschinger, E. *ApJS* **2001**, *137*, 1–20.

(17) Binney, J.; Tremaine, S., *Galactic Dynamics: Second Edition*; Princeton University Press: 2008.

(18) Birnboim, Y.; Dekel, A. *MNRAS* **2003**, *345*, 349–364.

(19) Bois, M. et al. *MNRAS* **2010**, *406*, 2405–2420.

(20) Bolton, A. S.; Burles, S.; Koopmans, L. V. E.; Treu, T.; Moustakas, L. A. *ApJ* **2006**, *638*, 703–724.

(21)   Bondi, H. *MNRAS* **1952**, *112*, 195.

(22)   Bondi, H.; Hoyle, F. *MNRAS* **1944**, *104*, 273.

(23)   Brennan, R.; Choi, E.; Somerville, R. S.; Hirschmann, M.; Naab, T.; Ostriker, J. P. *ApJ* **2018**, *860* 14, 14.

(24)   Bruzual, G.; Charlot, S. *MNRAS* **2003**, *344*, 1000–1028.

(25)   Bundy, K.; Bershady, M. A.; Law, D. R.; Yan, R.; Drory, N.; MacDonald, N.; Wake, D. A.; Cherinka, B.; Sánchez-Gallego, J. R.; Weijmans, A.-M.; Thomas, D. *ApJ* **2015**, *798* 7, 7.

(26)   Cappellari, M. *MNRAS* **2002**, *333*, 400–410.

(27)   Cappellari, M. *MNRAS* **2008**, *390*, 71–86.

(28)   Cappellari, M. *ARA&A* **2016**, *54*, 597–665.

(29)   Cappellari, M.; Copin, Y. *MNRAS* **2003**, *342*, 345–354.

(30)   Cappellari, M.; Emsellem, E. *PASP* **2004**, *116*, 138–147.

(31)   Cappellari, M.; Romanowsky, A. J.; Brodie, J. P.; Forbes, D. A.; Strader, J.; Foster, C.; Kartha, S. S.; Pastorello, N.; Pota, V.; Spitler, L. R.; Usher, C.; Arnold, J. A. *ApJ* **2015**, *804* L21, L21.

(32)   Cappellari, M.; Emsellem, E.; Krajnović, D.; McDermid, R. M.; Scott, N.; Verdoes Kleijn, G. A.; Young, L. M.; Alatalo, K.; Bacon, R.; Blitz, L.; Bois, M.; Bournaud, F.; Bureau, M.; Davies, R. L. *MNRAS* **2011**, *413*, 813–836.

(33)   Cappellari, M. et al. *MNRAS* **2013**, *432*, 1709–1741.

(34)   Cappellari, M. et al. *MNRAS* **2013**, *432*, 1862–1893.

(35)   Carpintero, D. D.; Aguilar, L. A. *MNRAS* **1998**, *298*, 1–21.

(36)   Chandrasekhar, S. *ApJ* **1943**, *97*, 255.

(37)   Cheung, E. et al. *Nature* **2016**, *533*, 504–508.

(38)   Choi, E.; Naab, T.; Ostriker, J. P.; Johansson, P. H.; Moster, B. P. *MNRAS* **2014**, *442*, 440–453.

(39)   Choi, E.; Ostriker, J. P.; Naab, T.; Somerville, R. S.; Hirschmann, M.; Núñez, A.; Hu, C.-Y.; Oser, L. *ApJ* **2017**, *844* 31, 31.

(40)   Choi, E.; Ostriker, J. P.; Naab, T.; Johansson, P. H. *ApJ* **2012**, *754* 125, 125.

(41)   Choi, E.; Ostriker, J. P.; Naab, T.; Oser, L.; Moster, B. P. *MNRAS* **2015**, *449*, 4105–4116.

(42)   Choi, E.; Somerville, R. S.; Ostriker, J. P.; Naab, T.; Hirschmann, M. *ArXiv e-prints* **2018**.

(43)   Chung, A.; Bureau, M. *AJ* **2004**, *127*, 3192–3212.

(44) Churazov, E.; Sazonov, S.; Sunyaev, R.; Forman, W.; Jones, C.; Böhringer, H. *MNRAS* **2005**, *363*, L91–L95.

(45) Crain, R. A.; Schaye, J.; Bower, R. G.; Furlong, M.; Schaller, M.; Theuns, T.; Dalla Vecchia, C.; Frenk, C. S.; McCarthy, I. G.; Helly, J. C.; Jenkins, A.; Rosas-Guevara, Y. M.; White, S. D. M.; Trayford, J. W. *MNRAS* **2015**, *450*, 1937–1961.

(46) Croom, S. M.; Lawrence, J. S.; Bland-Hawthorn, J.; Bryant, J. J.; Fogarty, L.; Richards, S.; Goodwin, M.; Farrell, T.; Miziarski, S.; Heald, R.; Jones, D. H. *MNRAS* **2012**, *421*, 872–893.

(47) Croton, D. J.; Springel, V.; White, S. D. M.; De Lucia, G.; Frenk, C. S.; Gao, L.; Jenkins, A.; Kauffmann, G.; Navarro, J. F.; Yoshida, N. *MNRAS* **2006**, *365*, 11–28.

(48) Davé, R.; Thompson, R.; Hopkins, P. F. *MNRAS* **2016**, *462*, 3265–3284.

(49) de Kool, M.; Arav, N.; Becker, R. H.; Gregg, M. D.; White, R. L.; Laurent-Muehleisen, S. A.; Price, T.; Korista, K. T. *ApJ* **2001**, *548*, 609–623.

(50) de Vaucouleurs, G. *Annales d'Astrophysique* **1948**, *11*, 247.

(51) Dehnen, W. *MNRAS* **1993**, *265*, 250.

(52) Dehnen, W.; Aly, H. *MNRAS* **2012**, *425*, 1068–1082.

(53) Dekel, A.; Birnboim, Y. *MNRAS* **2006**, *368*, 2–20.

(54) Di Matteo, P.; Pipino, A.; Lehnert, M. D.; Combes, F.; Semelin, B. *A&A* **2009**, *499*, 427–437.

(55) Dressler, A. In *Active Galactic Nuclei*, ed. by Osterbrock, D. E.; Miller, J. S., 1989; Vol. 134, p 217.

(56) Dubois, Y.; Gavazzi, R.; Peirani, S.; Silk, J. *MNRAS* **2013**, *433*, 3297–3313.

(57) Dubois, Y.; Peirani, S.; Pichon, C.; Devriendt, J.; Gavazzi, R.; Welker, C.; Volonteri, M. *MNRAS* **2016**, *463*, 3948–3964.

(58) Dullo, B. T.; Graham, A. W.; Knapen, J. H. *MNRAS* **2017**, *471*, 2321–2333.

(59) Eddington, A. S. *MNRAS* **1916**, *77*, 16–35.

(60) Einstein, A. *Annalen der Physik* **1916**, *354*, 769–822.

(61) Eisenreich, M.; Naab, T.; Choi, E.; Ostriker, J. P.; Emsellem, E. *MNRAS* **2017**, *468*, 751–768.

(62) Emsellem, E.; Krajnović, D.; Sarzi, M. *MNRAS* **2014**, *445*, L79–L83.

(63) Emsellem, E.; Cappellari, M.; Krajnović, D.; Alatalo, K.; Blitz, L.; Bois, M.; Bournaud, F.; Bureau, M.; Davies, R. L.; Davis, T. A.; de Zeeuw, P. T. *MNRAS* **2011**, *414*, 888–912.

(64) Emsellem, E.; Monnet, G.; Bacon, R. *A&A* **1994**, *285*, 723–738.

(65)   Emsellem, E.; Cappellari, M.; Peletier, R. F.; McDermid, R. M.; Bacon, R.; Bureau, M.; Copin, Y.; Davies, R. L.; Krajnović, D.; Kuntschner, H.; Miller, B. W.; de Zeeuw, P. T. *MNRAS* **2004**, *352*, 721–743.

(66)   Emsellem et al. *MNRAS* **2007**, *379*, 401–417.

(67)   Fabian, A. C. *ARA&A* **2012**, *50*, 455–489.

(68)   Foreman-Mackey, D.; Hogg, D. W.; Lang, D.; Goodman, J. *Publications of the Astronomical Society of the Pacific* **2013**, *125*, 306.

(69)   Freedman, D.; Diaconis, P. *Zeitschrift für Wahrscheinlichkeitstheorie und Verwandte Gebiete* **1981**, *57*, 453–476.

(70)   Frigo, M.; Balcells, M. *MNRAS* **2017**, *469*, 2184–2201.

(71)   Frigo, M.; Johnson, S. G. *Proceedings of the IEEE* **2005**, *93*, 216–231.

(72)   Frigo, M.; Naab, T.; Hirschmann, M.; Choi, E.; Somerville, R.; Krajnovic, D.; Davé, R.; Cappellari, M. *arXiv e-prints* **2018**.

(73)   Gebhardt, K.; Bender, R.; Bower, G.; Dressler, A.; Faber, S. M.; Filippenko, A. V.; Green, R.; Grillmair, C.; Ho, L. C.; Kormendy, J.; Lauer, T. R.; Magorrian, J.; Pinkney, J.; Richstone, D.; Tremaine, S. *ApJ* **2000**, *539*, L13–L16.

(74)   Genzel, R.; Eckart, A.; Ott, T.; Eisenhauer, F. *MNRAS* **1997**, *291*, 219–234.

(75)   Genzel, R. et al. *Nature* **2017**, *543*, 397–401.

(76)   Gerhard, O. E. *MNRAS* **1993**, *265*, 213.

(77)   Graham, M. T. et al. *MNRAS* **2018**, *477*, 4711–4737.

(78)   Guérou, A.; Emsellem, E.; Krajnović, D.; McDermid, R. M.; Contini, T.; Weilbacher, P. M. *A&A* **2016**, *591* A143, A143.

(79)   Hernquist, L. *ApJ* **1990**, *356*, 359–364.

(80)   Hernquist, L.; Ostriker, J. P. *ApJ* **1992**, *386*, 375–397.

(81)   Hilbert, S.; Marian, L.; Smith, R. E.; Desjacques, V. *MNRAS* **2012**, *426*, 2870–2888.

(82)   Hilbert, S.; Hartlap, J.; White, S. D. M.; Schneider, P. *A&A* **2009**, *499*, 31–43.

(83)   Hills, J. G.; Fullerton, L. W. *AJ* **1980**, *85*, 1281–1291.

(84)   Hilz, M.; Naab, T.; Ostriker, J. P. *MNRAS* **2013**, *429*, 2924–2933.

(85)   Hilz, M.; Naab, T.; Ostriker, J. P.; Thomas, J.; Burkert, A.; Jesseit, R. *MNRAS* **2012**, *425*, 3119–3136.

(86)   Hirschmann, M.; Naab, T.; Somerville, R. S.; Burkert, A.; Oser, L. *MNRAS* **2012**, *419*, 3200–3222.

(87)   Hirschmann, M.; Charlot, S.; Feltre, A.; Naab, T.; Choi, E.; Ostriker, J. P.; Somerville, R. S. *ArXiv e-prints* **2017**.

(88) Hirschmann, M.; Naab, T.; Davé, R.; Oppenheimer, B. D.; Ostriker, J. P.; Somerville, R. S.; Oser, L.; Genzel, R.; Tacconi, L. J.; Förster-Schreiber, N. M.; Burkert, A.; Genel, S. *MNRAS* **2013**, *436*, 2929–2949.

(89) Hirschmann, M.; Naab, T.; Ostriker, J. P.; Forbes, D. A.; Duc, P.-A.; Davé, R.; Oser, L.; Karabal, E. *MNRAS* **2015**, *449*, 528–550.

(90) Hoffman, L.; Cox, T. J.; Dutta, S.; Hernquist, L. *ApJ* **2009**, *705*, 920–925.

(91) Hopkins, P. F. *MNRAS* **2013**, *428*, 2840–2856.

(92) Hoyle, F.; Lyttleton, R. A. *Proceedings of the Cambridge Philosophical Society* **1939**, *35*, 405.

(93) Hu, C.-Y.; Naab, T.; Walch, S.; Moster, B. P.; Oser, L. *MNRAS* **2014**, *443*, 1173–1191.

(94) Hubble, E. P. *ApJ* **1926**, *64*, DOI: 10.1086/143018.

(95) Iwamoto, K.; Brachwitz, F.; Nomoto, K.; Kishimoto, N.; Umeda, H.; Hix, W. R.; Thielemann, F.-K. *ApJS* **1999**, *125*, 439–462.

(96) Jaffe, W. *MNRAS* **1983**, *202*, 995–999.

(97) Jain, B.; Seljak, U.; White, S. *ApJ* **2000**, *530*, 547–577.

(98) Jeans, J. H. *MNRAS* **1922**, *82*, 132.

(99) Jeans, J. H. *Philosophical Transactions of the Royal Society of London Series A* **1902**, *199*, 1–53.

(100) Jesseit, R.; Naab, T.; Peletier, R. F.; Burkert, A. *MNRAS* **2007**, *376*, 997–1020.

(101) Jesseit, R.; Naab, T.; Burkert, A. *MNRAS* **2005**, *360*, 1185–1200.

(102) Jesseit, R.; Cappellari, M.; Naab, T.; Emsellem, E.; Burkert, A. *MNRAS* **2009**, *397*, 1202–1214.

(103) Karakas, A. I. *MNRAS* **2010**, *403*, 1413–1425.

(104) Kennicutt Jr., R. C. *ApJ* **1998**, *498*, 541–552.

(105) Kormendy, J. In *The Nearest Active Galaxies*, ed. by Beckman, J.; Colina, L.; Netzer, H., 1993, pp 197–218.

(106) Kormendy, J.; Bender, R. *ApJ* **1996**, *464*, L119.

(107) Kormendy, J.; Ho, L. C. *ARA&A* **2013**, *51*, 511–653.

(108) Kormendy, J.; Fisher, D. B.; Cornell, M. E.; Bender, R. *ApJS* **2009**, *182*, 216–309.

(109) Krajnović, D. KINEMETRY: Analysis of 2D maps of kinematic moments of LOSVD., Astrophysics Source Code Library, 2014.

(110) Krajnović, D.; Emsellem, E.; den Brok, M.; Marino, R. A.; Schmidt, K. B.; Steinmetz, M.; Weilbacher, P. M. *MNRAS* **2018**, *477*, 5327–5337.

(111) Krajnović et al. *MNRAS* **2011**, *414*, 2923–2949.

(112) Kroupa, P. *MNRAS* **2001**, *322*, 231–246.

(113) Lablanche, P.-Y. et al. *MNRAS* **2012**, *424*, 1495–1521.

(114) Lagos, C. d. P.; Schaye, J.; Bahe, Y.; van de Sande, J.; Kay, S.; Barnes, D.; Davis, T.; Dalla Vecchia, C. *ArXiv e-prints* **2017**.

(115) Lagos, C. d. P.; Schaye, J.; Bahé, Y.; Van de Sande, J.; Kay, S. T.; Barnes, D.; Davis, T. A.; Dalla Vecchia, C. *MNRAS* **2018**, *476*, 4327–4345.

(116) Lauer, T. R. *MNRAS* **1985**, *216*, 429–438.

(117) Li, H.; Mao, S.; Emsellem, E.; Xu, D.; Springel, V.; Krajnović, D. *ArXiv e-prints* **2017**.

(118) Lovell, M. R.; Pillepich, A.; Genel, S.; Nelson, D.; Springel, V.; Pakmor, R.; Marinacci, F.; Weinberger, R.; Torrey, P.; Vogelsberger, M.; Alabi, A.; Hernquist, L. *MNRAS* **2018**, *481*, 1950–1975.

(119) Man, A. W. S.; Toft, S.; Zirm, A. W.; Wuyts, S.; van der Wel, A. *ApJ* **2012**, *744* 85, 85.

(120) Martizzi, D.; Jimmy; Teyssier, R.; Moore, B. *MNRAS* **2014**, *443*, 1500–1508.

(121) Mikkola, S.; Merritt, D. *AJ* **2008**, *135*, 2398–2405.

(122) Monaghan, J. J.; Lattanzio, J. C. *A&A* **1985**, *149*, 135–143.

(123) Naab, T.; Burkert, A. *ApJ* **2003**, *597*, 893–906.

(124) Naab, T.; Burkert, A. *ApJ* **2001**, *555*, L91–L94.

(125) Naab, T.; Ostriker, J. P. *ARA&A* **2017**, *55*, 59–109.

(126) Naab, T.; Johansson, P. H.; Ostriker, J. P. *ApJ* **2009**, *699*, L178–L182.

(127) Naab, T.; Burkert, A.; Hernquist, L. *ApJ* **1999**, *523*, L133–L136.

(128) Naab, T.; Oser, L.; Emsellem, E.; Cappellari, M.; Krajnović, D.; McDermid, R. M.; Alatalo, K.; Bayet, E.; Blitz, L.; Bois, M.; Bournaud, F. *MNRAS* **2014**, *444*, 3357–3387.

(129) Naab, T.; Jesseit, R.; Burkert, A. *MNRAS* **2006**, *372*, 839–852.

(130) Navarro, J. F.; Frenk, C. S.; White, S. D. M. *ApJ* **1997**, *490*, 493–508.

(131) Núñez, A.; Ostriker, J. P.; Naab, T.; Oser, L.; Hu, C.-Y.; Choi, E. *ApJ* **2017**, *836* 204, 204.

(132) Oser, L.; Naab, T.; Ostriker, J. P.; Johansson, P. H. *ApJ* **2012**, *744* 63, 63.

(133) Oser, L.; Ostriker, J. P.; Naab, T.; Johansson, P. H.; Burkert, A. *ApJ* **2010**, *725*, 2312–2323.

(134) Ostriker, J. P. *Comments on Astrophysics* **1980**, *8*, 177.

(135) Ostriker, J. P.; Choi, E.; Ciotti, L.; Novak, G. S.; Proga, D. *ApJ* **2010**, *722*, 642–652.

(136) Pearson, K. *Proceedings of the Royal Society of London Series I* **1895**, *58*, 240–242.

(137) Peirani, S.; Sonnenfeld, A.; Gavazzi, R.; Oguri, M.; Dubois, Y.; Silk, J.; Pichon, C.; Devriendt, J.; Kaviraj, S. *MNRAS* **2019**, *483*, 4615–4627.

(138) Penoyre, Z.; Moster, B. P.; Sijacki, D.; Genel, S. *MNRAS* **2017**, *468*, 3883–3906.

(139) Plummer, H. C. *MNRAS* **1911**, *71*, 460–470.

(140) Puchwein, E.; Springel, V. *MNRAS* **2013**, *428*, 2966–2979.

(141) Puchwein, E.; Sijacki, D.; Springel, V. *ApJ* **2008**, *687*, L53.

(142) Qu, Y.; Di Matteo, P.; Lehnert, M.; van Driel, W.; Jog, C. J. *A&A* **2010**, *515* A11, A11.

(143) Rantala, A.; Pihajoki, P.; Johansson, P. H.; Naab, T.; Lahén, N.; Sawala, T. *ApJ* **2017**, *840* 53, 53.

(144) Rantala, A.; Johansson, P. H.; Naab, T.; Thomas, J.; Frigo, M. *ApJ* **2018**, *864* 113, 113.

(145) Rantala, A.; Johansson, P. H.; Naab, T.; Thomas, J.; Frigo, M. *arXiv e-prints* **2018**.

(146) Remus, R.-S.; Dolag, K.; Naab, T.; Burkert, A.; Hirschmann, M.; Hoffmann, T. L.; Johansson, P. H. *MNRAS* **2017**, *464*, 3742–3756.

(147) Rodriguez-Gomez, V.; Pillepich, A.; Sales, L. V.; Genel, S.; Vogelsberger, M.; Zhu, Q.; Wellons, S.; Nelson, D.; Torrey, P.; Springel, V.; Ma, C.-P.; Hernquist, L. *MNRAS* **2016**, *458*, 2371–2390.

(148) Röttgers, B.; Naab, T.; Oser, L. *MNRAS* **2014**, *445*, 1065–1083.

(149) Salpeter, E. E. *ApJ* **1964**, *140*, 796–800.

(150) Sánchez, S. F.; Kennicutt, R. C.; Gil de Paz, A.; van de Ven, G.; Vílchez, J. M.; Wisotzki, L.; Walcher, C. J.; Mast, D.; Aguerri, J. A. L.; Albiol-Pérez, S.; Alonso-Herrero, A.; Alves, J. *A&A* **2012**, *538* A8, A8.

(151) Sazonov, S. Y.; Ostriker, J. P.; Ciotti, L.; Sunyaev, R. A. *MNRAS* **2005**, *358*, 168–180.

(152) Scannapieco, C.; Tissera, P. B.; White, S. D. M.; Springel, V. *MNRAS* **2005**, *364*, 552–564.

(153) Scannapieco, C.; Tissera, P. B.; White, S. D. M.; Springel, V. *MNRAS* **2006**, *371*, 1125–1139.

(154) Schaye, J. et al. *MNRAS* **2015**, *446*, 521–554.

(155) Schneider, P.; Kochanek, C.; Wambsganss, J., *Gravitational lensing: strong, weak and micro: Saas-Fee advanced course 33*; Springer Science & Business Media: 2006; Vol. 33.

(156) Schödel, R. et al. *Nature* **2002**, *419*, 694–696.

(157) Schulze, F.; Remus, R.-S.; Dolag, K.; Burkert, A.; Emsellem, E.; van de Ven, G. *ArXiv e-prints* **2018**.

(158) Schulze, F.; Remus, R.-S.; Dolag, K.; Burkert, A.; Emsellem, E.; van de Ven, G. *MNRAS* **2018**, *480*, 4636–4658.

(159) Somerville, R. S.; Davé, R. *ARA&A* **2015**, *53*, 51–113.

(160) Spergel, D. N.; Bean, R.; Doré, O.; Nolta, M. R.; Bennett, C. L.; Dunkley, J.; Hinshaw, G.; Jarosik, N.; Komatsu, E.; Page, L.; Peiris, H. V. *ApJS* **2007**, *170*, 377–408.

(161) Springel, V. *MNRAS* **2000**, *312*, 859–879.

(162) Springel, V. *ARA&A* **2010**, *48*, 391–430.

(163) Springel, V. *MNRAS* **2005**, *364*, 1105–1134.

(164) Springel, V.; Di Matteo, T.; Hernquist, L. *ApJ* **2005**, *620*, L79–L82.

(165) Thomas, J.; Ma, C.-P.; McConnell, N. J.; Greene, J. E.; Blakeslee, J. P.; Janish, R. *Nature* **2016**, *532*, 340–342.

(166) Thomas, J.; Jesseit, R.; Naab, T.; Saglia, R. P.; Burkert, A.; Bender, R. *MNRAS* **2007**, *381*, 1672–1696.

(167) Thomas et al. *MNRAS* **2007**, *382*, 657–684.

(168) Tsatsi, A.; Macciò, A. V.; van de Ven, G.; Moster, B. P. *ApJ* **2015**, *802* L3, L3.

(169) Tsatsi, A.; Lyubenova, M.; van de Ven, G.; Chang, J.; Aguerri, J. A. L.; Falcón-Barroso, J.; Macciò, A. V. *ArXiv e-prints* **2017**.

(170) Urry, C. M.; Padovani, P. *PASP* **1995**, *107*, 803.

(171) van de Sande, J.; Bland-Hawthorn, J.; Fogarty, L. M. R.; Cortese, L.; d'Eugenio, F.; Croom, S. M.; Scott, N.; Allen, J. T.; Brough, S.; Bryant, J. J. *ApJ* **2017**, *835* 104, 104.

(172) van den Bosch, R. C. E.; van de Ven, G.; Verolme, E. K.; Cappellari, M.; de Zeeuw, P. T. *MNRAS* **2008**, *385*, 647–666.

(173) van der Marel, R. P.; Franx, M. *ApJ* **1993**, *407*, 525–539.

(174) Veale, M.; Ma, C.-P.; Thomas, J.; Greene, J. E.; McConnell, N. J.; Walsh, J.; Ito, J.; Blakeslee, J. P.; Janish, R. *MNRAS* **2017**, *464*, 356–384.

(175) Vegetti, S.; Koopmans, L. V. E. *MNRAS* **2009**, *392*, 945–963.

(176) Vegetti, S.; Lagattuta, D. J.; McKean, J. P.; Auger, M. W.; Fassnacht, C. D.; Koopmans, L. V. E. *Nature* **2012**, *481*, 341–343.

(177) Vegetti, S.; Koopmans, L. V. E.; Auger, M. W.; Treu, T.; Bolton, A. S. *MNRAS* **2014**, *442*, 2017–2035.

(178) Vogelsberger, M.; Genel, S.; Springel, V.; Torrey, P.; Sijacki, D.; Xu, D.; Snyder, G.; Nelson, D.; Hernquist, L. *MNRAS* **2014**, *444*, 1518–1547.

(179) Vogelsberger, M.; Genel, S.; Springel, V.; Torrey, P.; Sijacki, D.; Xu, D.; Snyder, G.; Bird, S.; Nelson, D.; Hernquist, L. *Nature* **2014**, *509*, 177–182.

(180) Voronoi, G. *Journal fr die reine und angewandte Mathematik (Crelle's Journal)* **1908**, *133*, 97–102.

(181) Wendland, H. *Advances in Computational Mathematics* **1995**, *4*, 389–396.

(182) Wheeler, C.; Hopkins, P. F.; Pace, A. B.; Garrison-Kimmel, S.; Boylan-Kolchin, M.; Wetzel, A.; Bullock, J. S.; Keres, D.; Faucher-Giguere, C.-A.; Quataert, E. *arXiv e-prints* **2018**.

(183) White, S. D. M.; Rees, M. J. *MNRAS* **1978**, *183*, 341–358.

(184) Woosley, S. E.; Weaver, T. A. *ApJS* **1995**, *101*, 181.

(185) Wu, X.; Gerhard, O.; Naab, T.; Oser, L.; Martinez-Valpuesta, I.; Hilz, M.; Churazov, E.; Lyskova, N. *MNRAS* **2014**, *438*, 2701–2715.

(186) Wylezalek, D.; Zakamska, N. L. *MNRAS* **2016**, *461*, 3724–3739.

(187) Yuan, F.; Narayan, R. *ARA&A* **2014**, *52*, 529–588.

Acknowledgements

First of all, I would like to thank my PhD supervisor, Thorsten Naab, who always provided me with valuable advice and continuously supported me, sometimes when even I lost faith in myself. I consider myself extremely lucky to have him as supervisor. Similarly I would like to thank all the mentors that over the course of my life motivated me to pursue a career in Physics: Enrico Rossato, Marc Balcells, Enrico Maria Corsini. Thanks also to the thesis defense committee for being so flexible and for taking part in this important moment of my life.

Huge thanks go to all the various friends I met during these years in Munich, with whom I made unforgettable memories. Among others, in order of hair length: Ricard Ardevol, Talytha Barbosa, Linda Baronchelli, Aoife Boyle, Raffaella Capasso, Jens Stücker, Anabele Pardi, Miranda Jarvis, Malin Renneby, Timo Halbesma, Vlas Sokolov, Michael Gabler, Francesco Rizzuto, Ninoy Rahman, Andreas Schmidt, Philipp Busch, Chris Byrohl, Maximilian Eisenreich, Tim-Eric Rathjen. Thanks again to Philipp for translating the abstract into german. A special thanks to all IMPRS reps past and future; joining you was an important personal experience and a ton of fun! Thanks also to the austrian driver who saved me and by extension my thesis.

I am very grateful to my family, who encouraged me throughout the PhD and throughout my life as a whole, and were always there when I needed them. Lastly I would like to thank my girlfriend Chiara, who somehow managed to tolerate me for several years (!) and accompanied me through fun and troubled times alike.